

Probing Cellular Uptake of Nanoparticles, One at a Time



Zur Erlangung des akademischen Grades eines
DOKTORS DER NATURWISSENSCHAFTEN

(Dr. rer. nat.)

Fakultät für Chemie und Biowissenschaften

Karlsruher Institut für Technologie (KIT) – Universitätsbereich

genehmigte

DISSERTATION

presented by

Yiming Li, M.Sc. (Medical Physics)

Born in: Fujian, China

Referees: Prof. Dr. Gerd Ulrich Nienhaus

Prof. Dr. Martin Bastmeyer

Oral Examination: 20 October 2015

Declaration

“I hereby affirm that I have written this thesis independently and without use of resources other than those quoted. Cited and copied work is marked as such.”

Content

Chapter 1	1
Introduction	1
1.1 Investigation of Nanoparticle Uptake by Live Cells	1
1.2 Mechanisms of Endocytosis	1
1.2.1 Phagocytosis	3
1.2.2 Pinocytosis	3
1.3 Optical Nanoscopy	6
1.3.1 Resolution Limit	7
1.3.2 Far-field Fluorescence Nanoscopy Techniques	9
1.4 Outline of this Work	13
Chapter 2	16
Software Development of Localization Based Super Resolution Microscopy	16
2.1 Fluorescence Image Formation and Noise Models	17
2.2 General Molecule Detection Framework	22
2.3 Description of the a-livePALM Algorithm	23
2.4 Comparison of a-livePALM and DAOFIND	28
2.5 Software and Hardware Implementation	30
2.6 Image Simulation	32
2.7 Performance Assessment	33
2.7.1 Recall and Precision	33
2.7.2 Software Comparison	34
2.8 ISBI Localization Microscopy Challenge	46
Chapter 3	50
Experimental Setup for 3D Localization Microscopy	50
3.1 The TIRF Microscope	50
3.2 Experimental Setup	52
3.3 3D Super-resolution Imaging	53
3.3.1 3D Astigmatism Super-resolution Imaging	53
3.3.2 Experimental Note on Calibration Curve Generation	57
3.3.3 Dual Channel 3D Astigmatism Super-resolution Imaging	61
Chapter 4	64

Combination of Single Particle Tracking and Localization Microscopy	64
4.1 Combination of PALM and SPT.....	64
4.2 Fluorophore Selection.....	67
4.3 Single Particle Tracking and Moment Scaling Spectrum Analysis	70
Chapter 5	75
Materials and Methods.....	75
5.1 Immunostaining	75
5.2 Tagging by Fluorescent Proteins	78
5.3 Imaging Buffer.....	80
5.4 Protein labeling.....	80
5.5 Cell Culture.....	81
5.6 Inhibitor Studies	81
5.7 PS40 Nanoparticle Functionalization	82
5.7.1 Directly Coupled PS40-Transferrin NPs	82
5.7.2 Tf Modified with a PEG linker (PS40-PEG10K-Tf).....	82
5.7.3 Characterization of PS NPs	84
Chapter 6	86
Super-resolution Imaging of Microtubules and Clathrin Coated Pits	86
6.1 Super-resolution Imaging of Microtubules.....	86
6.2 Super-resolution Imaging of Clathrin Coated Pits.....	91
Chapter 7	98
Super-resolution Imaging-based Single Particle Tracking Reveals Fast Dynamics of Nanoparticle-cell Interactions	98
7.1 Interaction between PS40 NPs and CCPs.....	98
7.1.1 Accumulation of PS40 NPs on the Membrane	100
7.2 Two Types of Interaction between PS40 NPs and CCPs.....	102
7.3 Co-localization of PS NPs with CCPs.....	104
7.3.1 Role of Clathrin in the Cellular Uptake of PS NPs	104
7.3.2 Co-localization Probability.....	105
7.4 Mobility of PS NPs on the Membrane.....	110
7.4.1 MSS Analysis of the Mobility of Bare PS NPs on the Membrane.....	110
7.4.2 Microscopic Diffusion Coefficients	112
7.5 Spinning Disk Confocal Imaging	113
7.6 Size of CCPs.....	116
7.7 Summary.....	117
Chapter 8	119
Summary.....	119

Acronyms	126
References	129
Appendix	144
List of Publications	148
List of Presentations	149
Curriculum Vitae	150
Acknowledgements	151

Chapter 1

Introduction

1.1 Investigation of Nanoparticle Uptake by Live Cells

In recent years, nanoparticles (NPs) have emerged as important players in modern medicine. NPs intended for clinical use have to overcome the cell membrane barrier in order to enter their destined target cell. Mechanistic studies of cellular uptake of NPs are essential to their design for practical drug/imaging applications¹⁻⁴. The cellular uptake of NPs is affected by many parameters including physicochemical properties of NPs, intracellular concentrations, duration of contact, subcellular distributions and interactions with biological molecules¹. Still, how these particles interact with cells, in particular, how they bind to the membrane and are taken up by the cells remains unclear. It is important to point out that NPs typically use different entry routes in parallel, making it very difficult to identify a specific one. Most of the work suffers from poor NP characterization, and the use of inhibitors to block specific pathways often complicates the studies further. Inhibitors can introduce toxicity, artefacts and they need adequate controls that are often overlooked⁵.

Mapping these processes requires a technique with both high spatial and temporal resolution due to the sub-diffraction nature of the membrane morphology and the fast dynamic interactions between NPs and their membrane receptors⁶. Such early stage knowledge is prerequisite information for any further development of these nanomaterials for their desired biomedical applications. Highly sensitive fluorescence microscopy imaging techniques are currently emerging as powerful approaches for probing cellular events in real time. However, despite rapid progress in recent years, in situ visualization of the fast entry process of NPs with nanoscale resolution remains challenging. Recent advancements in super-resolution fluorescence microscopy have extended the spatial resolution down to tens of nanometers⁷. These techniques have opened a whole new world to image the structural details of biological systems⁸.

1.2 Mechanisms of Endocytosis

Endocytosis is a fundamental cellular process that is used by cells to internalize environmental materials⁹. It involves deformation of the plasma membrane and generates membrane vesicle carriers with the help of adapter proteins. The ingested vesicles are transported to endosomes, from which they can either be sent to lysosomes for digestion or be recycled to the plasma membrane. The metabolites generated in the

lysosomes can be transferred into the cytosol, where they can be used by the cell. Endocytosis regulates the interaction between the cell and its environment. Thereby, it not only controls the uptake of nutrients, but also plays a critical role in cell adhesion and migration, receptor signaling, cell polarity, *etc*¹⁰.

However, the mechanism by which the cell regulates endocytosis is still unclear. There are many difficulties for revealing the mechanisms of endocytosis: (i) a generally accepted inhibitor or marker is still needed^{5,9}, (ii) technical limitations such as imaging resolution of conventional light microscopy and cell perturbation by high resolution electron microscopy¹¹, (iii) overlap between the different pathways. Molecules can be taken up by cells through multiple pathways. Some associated proteins can also be found in different pathways.

Historically, endocytosis has been divided into two categories, depending on the cargo size: phagocytosis (also called cell eating) and pinocytosis (also known as cell drinking) as shown in **Figure 1.1**. Phagocytosis is employed by only a few types of cells (*i.e.*, dendritic cells, neutrophils, and macrophages¹²). Pinocytosis is more universal and occurs in almost every eukaryotic cell. It can be further subdivided into a number of different pathways, based on the proteins and lipids involved: clathrin-mediated endocytosis (CME), caveolae-mediated endocytosis, clathrin/caveolae-independent endocytosis, and micropinocytosis. It is believed that a deeper understanding of the mechanistic details of endocytosis will facilitate the development of NPs with precise targeting and enhanced therapeutic outcomes.

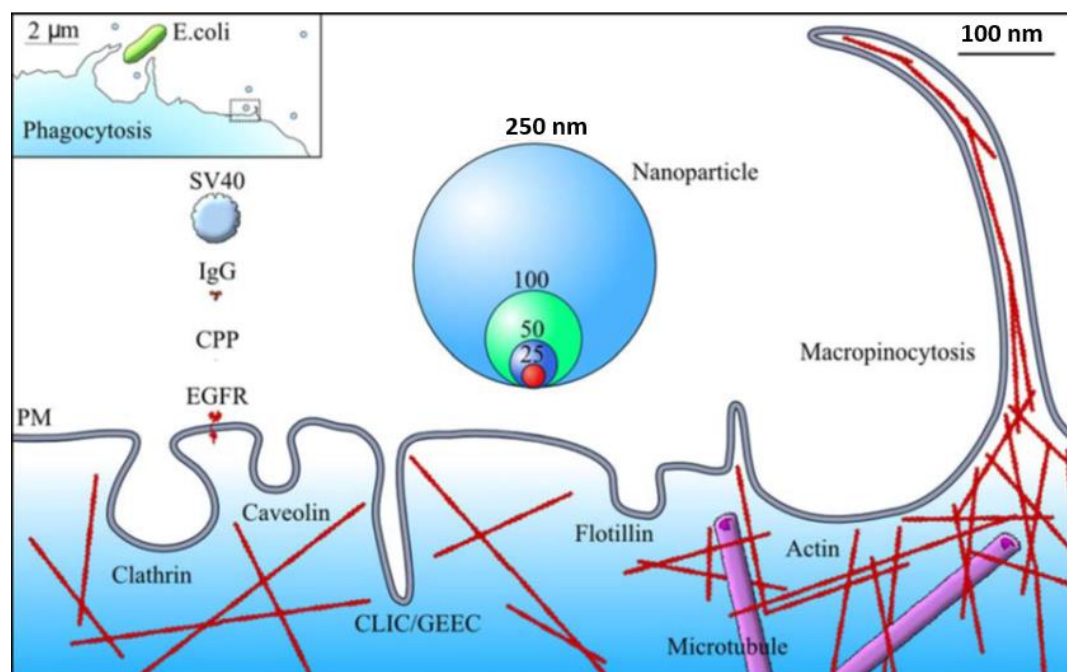


Figure 1.1 Pathways of endocytosis and its size limitations. Image adopted from Ref. [13].

1.2.1 Phagocytosis

Phagocytosis is employed by only a few specialized cells, especially immune cells such as mast cells, macrophages, monocytes and neutrophils. They are called professional phagocytic cells. Their major role is to engulf disabled particles, dead cells and infectious bacteria and viruses¹⁴. Typically, phagocytosis is triggered by the interaction of cell-surface receptors and foreign agents with particular surface ligands or by specific cell membrane recognition of the particle through the recruitment of receptors (opsonisation). Opsonisation happens in immune cells with soluble receptors such as proteins of the complement system (*i.e.*, CR3¹⁵), antibodies (*i.e.*, IgG¹⁶), acetylcholine and laminin¹⁷. Attractive forces, *e.g.*, van der Waals interactions, electrostatic interactions, hydrophobic/hydrophilic effects, between the cells and the NP surfaces are involved in the internalization of NPs via phagocytosis. In addition, phagocytosis can also be triggered by opsonins adsorbed on the particle surface which can be recognized by the receptors on the cell membrane. Phagocytosis starts with a cup-shaped membrane distortion, and then the membrane gradually surrounds the particle/pathogen with the help of actin¹⁸. The contact angle between the membrane and the particle has a significant effect on the ability of macrophages to internalize particles. Some studies have demonstrated that elongated particles with higher aspect ratios are less prone to be internalized through phagocytosis^{19,20}.

1.2.2 Pinocytosis

1.2.2.1 Clathrin-mediated Endocytosis

CME is by far the most studied endocytosis process. It was first discovered by Roth and Porter in 1964 using thin-section electron microscopy²¹. CME has been reported to be one of the most important pathways that involves intercellular signaling, membrane recycling, and uptake of nutrients²². CME starts with the participation of protein machinery to induce curvature in the membrane to form clathrin coated pits (CCPs) on the cytosolic side of the plasma membrane²³. To form the clathrin cage assembly, adaptor proteins (APs) are needed²⁴. APs coordinate formation of a putative nucleation site, where clathrin will be recruited and vesicles will bud^{25,26}. The CCPs then invaginate and pinch off from the plasma membrane by activation of the GTPase dynamin, a protein that is assembled as a ring around the neck of the invagination site²⁷. Live cell imaging studies have shown that actin is involved in the scission of the CCPs²⁸. After the CCPs have detached from the plasma membrane, the clathrin coat is disassembled by the ATPase heat shock cognate 70 (HSC70) and its cofactor, auxilin²³. The uncoated vesicles are then either recycled back to the plasma membrane or further guided to early endosomes. CME is a highly dynamic process. The lifetime of a CCP is between 20 s and 2 min⁹. CCPs can grow into clathrin coated vesicles (CCV) with a diameter as large as 200 nm²⁹.

CCPs are responsible for the uptake of many membrane receptors and their cargoes,

among which the uptake of transferrin-bound iron is one of the best understood processes in cell biology. Transferrin (Tf) is a single-chain glycoprotein which consists of *ca.* 700 amino acids with a molecular mass of *ca.* 80 kDa. The polypeptide chain folds into two lobes with homologous N-terminal and C-terminal iron-binding domains. At the neutral pH of blood, two Fe(III) ions can be bound to transferrin with a dissociation constant of 10^{-23} M. **Figure 1.2** shows a model of iron uptake through receptor-mediated endocytosis. After loading iron, the di-ferric transferrin (holo-transferrin) binds to its receptor (transferrin receptor-1, TfR1) on the cell surface. The Tf-TfR1 complex is rapidly internalized by receptor-mediated endocytosis through CCPs and routed into the endosomal compartment. At the low pH inside the endosome, the conformations of both transferrin-Fe(III) and TfR1 are changed, resulting in iron release from the protein. The free Fe(III) is reduced to Fe(II) in the endosome. Fe(II) is subsequently transported from the endosome to the cytosol by the divalent metal transporter1 (DMT1). After release of iron into the endosome, the resultant apo-Tf remains bound to TfR1 at acidic pH in the endosome and the complex is recycled through exocytic vesicles back to the cell surface. At the more neutral pH of the extracellular plasma, apo-Tf dissociates from its receptor and is released into the circulation and free to bind iron to initiate further rounds of uptake of Tf-bound iron.

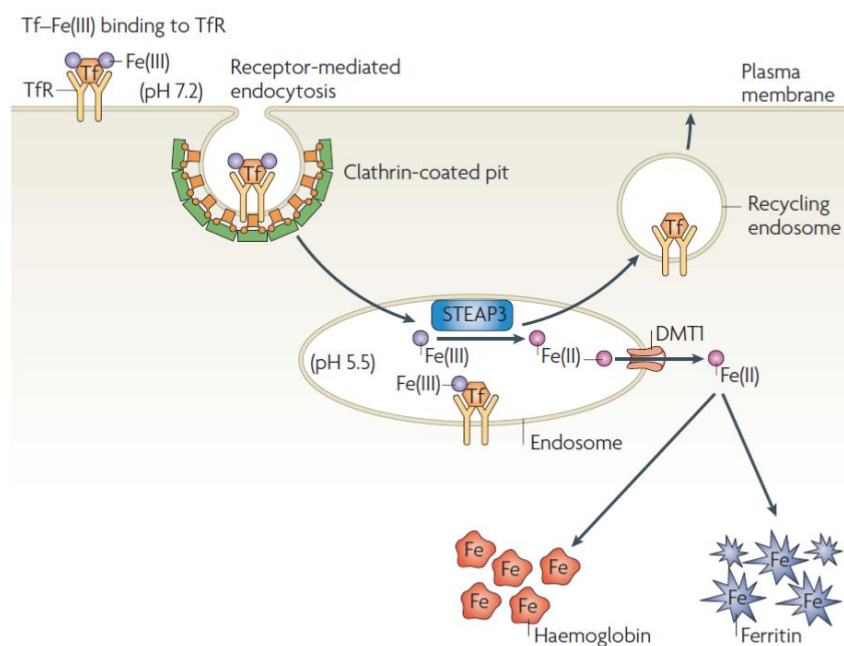


Figure 1.2 Transferrin and transferrin receptor mediated cellular uptake of iron. Fe(III) is bound to Tf with high affinity. The di-ferric Tf then binds to TfR1 and forms a Tf-TfR1 complex on the cell surface. The resulting complex is internalized by CME. At low pH in the internalized vesicle (endosome), Fe(III) is released from Tf and converted to Fe(II) by the endosomal reductase STEAP3. Fe(II) is then transported into the cytosol by DMT1. Fe(II) can be utilized as a cofactor for heme to form haemoglobin or stored in ferritin. The Tf-TfR1 complex is exocytosed back to the cell surface. Image adopted from Ref. [30].

Although CME is referred to as receptor-mediated endocytosis, the uptake of non-targeted NPs may also occur through CME. For example, cationic poly(ethylene glycol)-polylactide NPs (around 100 nm) appeared to be internalized through CME as well as micropinocytosis in HeLa cells³¹. Modified poly(lactic-co-glycolic acid) (PLGA) NPs coated by poly(L-lysine) were found to be rapidly internalized *via* CME³². Mesoporous silica-based NPs³³ and cationic chitosan NPs³⁴ were also found to be internalized through CME.

1.2.2.2 Caveolae-Mediated Endocytosis

Caveolae-mediated endocytosis is the most studied clathrin-independent carrier (CLIC) pathway. It participates in many cellular processes including signal transduction, protein uptake, and cholesterol homeostasis³⁵. Caveolae are flask-shaped invaginations of the plasma membrane with diameters of 50 – 80 nm³⁶. They are abundant in many different types of cells, such as fibroblasts, smooth muscle cells, adipocytes and endothelial cells. Cells such as neurons and leukocytes were found to lack caveolae³⁷. A caveola is coated predominately by hairpin-like caveolin (CAV1, CAV2 and CAV3)³⁸. Cavins, which also coat the caveolae, are believed to cooperate with the caveolins to regulate the formation of caveolae³⁹. Dynamin is also supposed to enable vesicle scission of caveolae⁴⁰. The mechanism of caveolae-mediated endocytosis is still subject of study because the intracellular transport of caveolae still has to be elucidated.

It has been reported that a number of non-enveloped viruses such as Simian Virus 40 enter cells through caveolae-mediated endocytosis⁴¹. Several other pathogens also exploit this pathway to avoid lysosomal degradation. Therefore, it is also believed to be beneficial for cellular delivery of proteins and DNA⁴². Nanomaterial has also been reported to enter cells *via* caveolae. Polymeric micelles with cross-linked anionic core were found to be taken up predominately through caveolae-mediated endocytosis in cancer cells⁴³. Amphiphilic polysiloxane NPs were shown to selectively target caveolae in human aortic endothelial cells⁴⁴.

1.2.2.3 Clathrin- and Caveolae-independent Endocytosis

Endocytosis can also occur independently of clathrin and caveolae. However, relatively few endogenous proteins associated with this pathway have been reported to date, and of those that have been discovered, little is known about how they regulate the mechanism of endocytosis¹⁰. Based on the effectors, this pathway is presently classified as Arf6-dependent, flotillin-dependent, Cdc42-dependent and RhoA-dependent¹⁰. This pathway was initially discovered because a number of bacterial toxins and cell surface proteins entered cells devoid of both clathrin and caveolin⁴⁵. In such cells, *ca.* 90 nm vesicles have been shown to carry cargoes including extracellular fluid, glycosylphosphatidylinositol (GPI)-linked proteins, interleukin-2, and growth hormones⁴⁶. These vesicles do not require the presence of coat proteins; however, they

appear to require specific lipid compositions and are dependent on cholesterol. After leaving the plasma membrane, the vesicles are usually delivered to early endosomes, followed by transfer to late endosomes and lysosomes. In addition, their cargo can be routed to the trans-Golgi network or recycled back to the plasma membrane⁴⁷.

There are not many reports on nanomaterials entering cells *via* different subtypes of clathrin- and caveolae-independent endocytosis. The examples include polyplexes of self-branched and trisaccharide-substituted chitosan oligomer NPs (SBTCO) for the delivery of DNA⁴⁸. SBTCO were primarily taken up by cells via clathrin independent endocytosis. Other examples are NPs and polymers modified with folate⁴⁹. However, multiple pathways were reported to be involved in the uptake of folate by cells including CME in specific cell types^{10,50}.

1.2.2.4 Macropinocytosis

Unlike the above discussed endocytosis mechanisms which are regulated by the direct action of receptor or cargo molecules, macropinocytosis is initiated by the transient activation of a tyrosine kinase receptor (such as the epidermal growth factor and the platelet-derived growth factor receptor)⁵¹. Receptor activation leads to an increase in actin polymerization and triggers formation of membrane ruffles⁵². These membrane ruffles engulf a large quantity of the surrounding fluid and nutrients, thus forming large (0.5 – 10 μm) organelles called macropinosomes. A variety of particles such as bacteria, apoptotic bodies, necrotic cells and viruses can also induce the ruffling behavior independently of the growth factors⁵¹⁻⁵³. Macropinosomes are sensitive to the cytoplasmic pH and undergo acidification and fusion events⁵⁴.

Recently, lapatinib-loaded NPs formulated with a core of albumin and lipid corona formed by egg yolk lecithin were reported to be internalized by BT-474 cells through multiple pathways including clathrin-dependent pinocytosis and micropinocytosis⁵⁵.

1.3 Optical Nanoscopy

The study of cellular processes such as endocytosis requires sensitive and non-invasive observation techniques. In 1665, Robert Hooke discovered the cell as the fundamental unit of life with the help of light microscopy, thus initiating one of the great revolutions of human science⁵⁶. Because the traditional light microscopy suffers from low contrast in biological samples, fluorescence microscopy has become the most widely used technique in cellular biology for noninvasive, time-resolved imaging with high biochemical specificity. Fluorescent probes have become available in a variety of colors that span the whole visible spectrum. Various labeling techniques, such as immune labeling and in situ hybridization, allow biomolecules of interest to be specifically labeled, even enabling simultaneous visualization of multiple targets through multicolor imaging. Furthermore, the revolutionizing development of fluorescent proteins and other genetically encoded fluorescent labels has allowed specific proteins

in living cells to be observed in real time⁵⁷.

Until recently, all live-cell analysis methods using light microscopy approaches suffered from the resolution limit set by the diffraction of light which states that two points can only be resolved if their distance is larger than $\frac{1}{2}$ the wavelength used for imaging, *i.e.*, ~ 200 nm for visible light, which is insufficient to visualize subcellular structures. As described in the famous publication of Ernst Abbe (1873)⁵⁸, this limit was regarded to be insurmountable due to the diffraction theory of light. A very similar conclusion was obtained in 1903 by Lord Rayleigh⁵⁹. In the past 20 years, so-called super-resolution fluorescence microscopy techniques have been developed that circumvent the diffraction limit and achieve resolution down to ~ 10 nm.

1.3.1 Resolution Limit

In real optical systems, the resolution that can be achieved depends on two factors: 1) the phenomenon of diffraction of light; 2) the numerical aperture of the objective in use. According to Abbe, the propagation of a ray from the object to the image involves two stages. The incident light first interacts with the specimen by diffraction and is deflected at an angle compatible with the diffraction theory. The lens will gather 0th-order and higher order of the diffracted light from each specimen point, and a diffraction pattern is formed in the back focal plane of the objective. These diffracted rays will interfere with each other, producing an image at the image plane. The closer the features of the specimen are to each other, the larger are the diffraction angles. Therefore, the ability of a lens to resolve fine details of a specimen depends on its ability to gather the higher orders of the diffracted light at the periphery of the lens. If the specimen feature are so small that even first-order diffraction are excluded from the lens, an Airy pattern in which the size is independent of the size of the feature will be formed from the 0th-order wave. Thus, any feature smaller than about half the wavelength of the light will appear larger than it actually is.

The resolution limit is usually obtained by considering two points in the object plane, and calculating the images in the imaging plane, to see whether or not the summed image still resolves the points. According to Fourier optics, the object appears as the Fourier spectrum of the sample in the back focal plane of the imaging lens and finally in the image plane, the various Fourier components passed by the lens are recombined to form a replica of the sample (**Figure 1.3**). However, the lens has only finite transverse dimensions. Only a certain portion of the diffracted components are intercepted by this finite pupil. The components not intercepted are precisely the high-frequency components of the object amplitude transmittance. In Fourier space, the maximum spatial frequency is given by:

$$F_{max} = k_{max} \cdot \frac{2\pi}{\lambda f} = f \sin \alpha_{max} \cdot \frac{2\pi}{\lambda f} = \frac{2\pi NA}{\lambda}, \quad (1.1)$$

where f is the focal length, λ is the wavelength, NA is the numerical aperture of the lens, k_{max} is the maximum radius of the image allowed by the objective in the focal

plane. Therefore, the lens can be used as a low-pass filter. Loss of high spatial frequency components causes blurring and loss of sharpness which is the fundamental reason for the resolution limit of a microscope. We can assume that, after passing the lens, the frequency domain is multiplied by a circle function for the circular back aperture of the lens:

$$\begin{aligned} \text{circ}(r) &= 1 & r &\leq \frac{2\pi NA}{\lambda} \\ &= 0 & r &> \frac{2\pi NA}{\lambda} \end{aligned} \quad (1.2)$$

Since multiplication in the frequency domain will result in a convolution in the image domain, the image of one single point object after the lens (point spread function, PSF) can be written as

$$FT^{-1}(\text{circ}(r)) = A \frac{J_1\left(\frac{2\pi NA}{\lambda} r\right)}{\frac{2\pi NA}{\lambda} r}, \quad (1.3)$$

where FT^{-1} is the inverse Fourier transformation, J_1 is the first kind of Bessel function, A is a scaling factor. The intensity of the diffraction pattern of a single point is the so called Airy pattern. There are different methods for defining the resolving power of an optical system. One of the possibilities is the Rayleigh criterion, according to which two points are just resolved as long as the center of one of the Airy patterns does not coincide with the first zero of the other one. The first zeros of $J_1(x)$ can be found at $x \approx 3.83$, therefore, the first dark ring occurs (resolution limit) when

$$r = \frac{3.83\lambda}{2\pi NA} = \frac{0.61\lambda}{NA}. \quad (1.4)$$

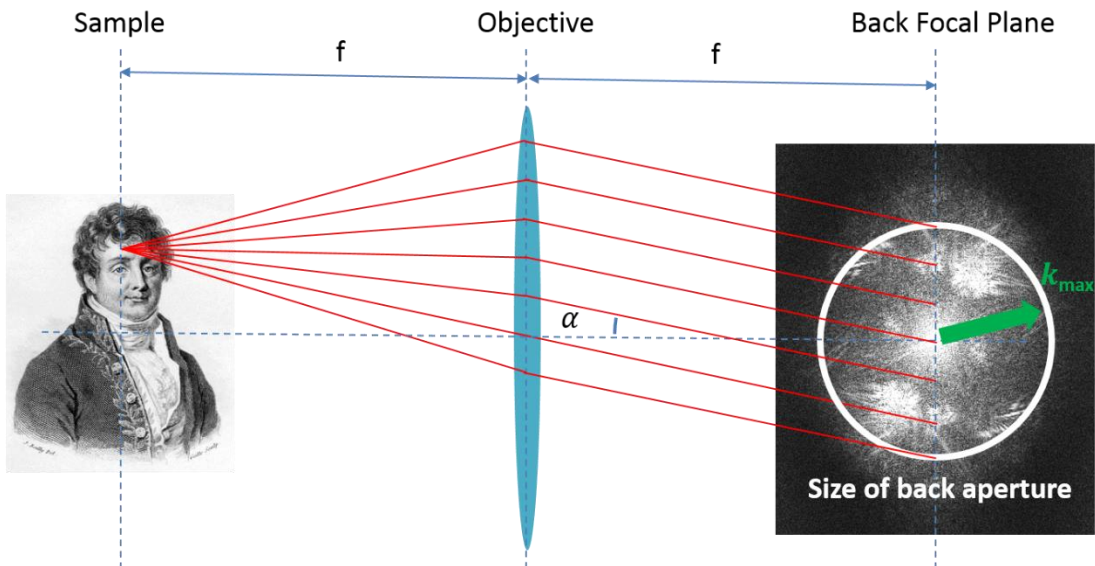


Figure 1.3 Fourier Optics and microscope resolution.

1.3.2 Far-field Fluorescence Nanoscopy Techniques

Although electron microscopy and other ultra-structure imaging methods based on ionizing radiation have the great advantage of an unprecedented resolution, the use of electron-dense tags for molecule-specific labeling in electron microscopy has limitations such as low labeling efficiency and the small number of species that can be simultaneously observed, making it difficult to map out molecular interactions in 3 dimensional (3D) intact cells, and rather difficult in living ones because electron microscopy requires ultra-high vacuum conditions⁶⁰. Another way to overcome the diffraction barrier is to use near-field optics⁶¹, which, however, is surface-bound and hence difficult to apply to (the interior of) a cell.

Since 1994, new optical fluorescence-based strategies have been developed that break the diffraction barrier in the far-field. These techniques prove that diffraction no longer poses a firm limit on the attainable resolution. The development of these fluorescence imaging techniques has pushed the boundaries of optical resolution to a few nanometers, so that an optical analysis of the nano-biostructures has become possible.

1.3.2.1 STED: Stimulated Emission Depletion Microscopy

Stimulated emission depletion microscopy uses the non-linear de-excitation of fluorescent dyes to overcome the resolution limit imposed by diffraction in standard confocal laser scanning microscopes and conventional far-field optical microscopes. The fluorescence excitation created by a focused beam of excitation light is narrowed down in space by simultaneously applying a second red-shifted spot of light featuring a central zero (*e.g.*, a doughnut, see **Figure 1.4**) for de-excitation. The de-excitation (STED) beam is used to trigger stimulated emission of the excited fluorophores. This effectively confines the fluorescence emission to a small region at the center of the donut, thereby reducing the size of the PSF and increasing the resolution.

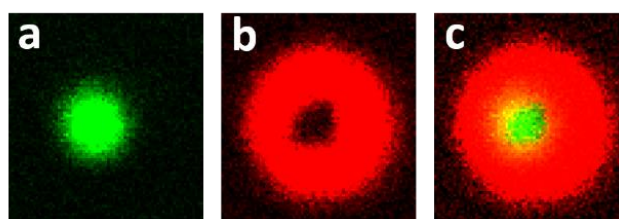


Figure 1.4 Excitation laser spot (a), de-excitation laser spot (b), overlay of excitation and depletion beam (c). Fluorescence emission occurs only from the central area.

Different implementations of STED have demonstrated resolutions as high as 5.8 nm in the lateral directions⁶², and 40 – 45 nm in all three dimensions simultaneously when lateral and axial STED beams are combined in a 4Pi geometry for 3D super-resolution imaging⁶³.

1.3.2.2 SPEM/SSIM: Saturated Pattern Excitation Microscopy or Saturated Structured Illumination Microscopy

As shown in **Figure 1.3**, there is a maximum spatial frequency that can be observed by the microscope. Information beyond the maximum frequency is fundamentally unobservable. When a sample is illuminated by wide-field, periodically patterned light, the excitation pattern mixes with the spatial information in the sample and shifts the high frequency structural information into the detection range of the microscope (**Figure 1.5**). To cover the field of view, the pattern is scanned across the specimen by phase-shifting the maxima of the interference pattern and reading out the fluorescence image onto a camera for each scanning step. Since resolution is improved only perpendicular to the line-shaped zeros, the pattern is tilted several times to cover all directions in the focal plane. For normal, linear, structured illumination microscopy, the maximum frequency shift cannot be larger than k_{max} . Therefore, its resolution can only be improved by a factor of 2. For SPEM/SSIM, higher frequencies are introduced by non-linear excitation of the fluorophores, which effectively expands the frequency space detectable by the microscope, thereby reducing the PSF size. Mathematical analysis of the data reveals super-resolved images. The experimental realization of SSIM attained ~ 50 nm in lateral resolution⁶⁴.

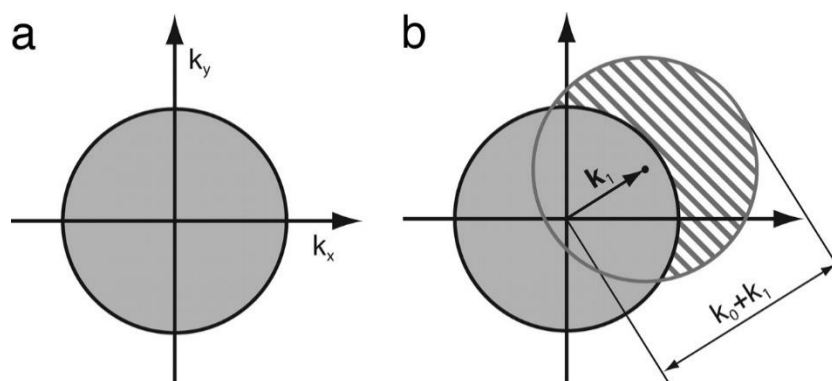


Figure 1.5 Concept of structured illumination. (a) Observable frequency region of conventional microscope with radius k_0 . (b) A new set of information becomes visible in the hatched circle when the excitation light contains the spatial frequency k_1 . The maximum detectable spatial frequency can reach $k_0 + k_1$. Image adopted from Ref. [64].

1.3.2.3 Localization Microscopy

(Fluorescence) Photoactivation localization microscopy and stochastic optical reconstruction microscopy rely on photoactivatable fluorophores to sequentially and stochastically localize each fluorophore with high precision. It has long been known that a simple fitting procedure on the single molecule PSF image allows a precision of position determination that significantly exceeds the width of the PSF^{65,66}, which governs the resolution limit of conventional fluorescence microscopy. However, most applications worked with well separated single molecules. In conventional fluorescence

microscopy, the sample has to be labeled with a high density of fluorescent markers to faithfully sample the structures. The PSFs of these fluorophores overlap and cannot be localized individually with high precision. This situation changed drastically when people realized that time could be used to separate the fluorophores in close proximity. By switching individual molecules stochastically and sparsely on by light-induced activation, fluorophores can be localized in densely labeled samples. The fundamental concept behind this technique is the controlled activation so that each fluorophore has a small probability of being photoactivated ('on' state) while the majority of the population is kept in the dark ('off' state). Therefore, the 'on' state fluorophores are well separated at each time instant. By calculating the centroid of the diffraction spot produced by each molecule, one can precisely determine the positions of the fluorophores. Then, the fluorophores are switched off and new ones are stochastically switched on. The process is repeated until all fluorophores have been localized. Up to 10^5 images are collected and subsequently analyzed by specialized software to identify the positions of individual molecules. All positions are then plotted to construct a high resolution image (**Figure 1.6**).

STORM has been initiated with pairs of photochromic cyanine dyes, one of which was used as an activation (switch-on) facilitator⁶⁷, while photoactivatable fluorescent proteins (*e.g.*, EosFP, paGFP) were used in the original PALM and (F)PALM papers^{68,69}. Variations of this method have also been published by numerous groups using a variety of excitation schemes and induced dark states with synthetic dyes and fluorescent proteins. Direct STORM (dSTORM)⁷⁰ and ground state depletion and individual molecule return (GSDIM)⁷¹ utilize the reversible photoswitching of organic fluorochromes to a metastable dark state (*e.g.*, a triplet or redox state), which extends this method in principle to any conventional dye. PALM with independently running acquisition (PALMIRA)⁷² allows the digital camera to run at high speed without synchronization to the activation laser or the switching cycles of the fluorophores.

The resolution of localization microscopy is no longer limited by the diffraction of light, but rather governed by how precise one can localize the diffraction limited PSF. The precision of this localization process is given by s/\sqrt{N} , where s is the standard deviation of the PSF, N is the number of photons detected⁶⁵. Additionally, the resolution is affected by the density of the labels (Nyquist criterion) in the structure. The Nyquist resolution is given by $2/(\text{localization density})^{1/D}$ according to Shroff *et al.* [73]. Here, D is the dimension of the structure. PALM, STORM and other concepts using a stochastic readout have achieved remarkable resolutions of <20 nm in the lateral dimensions. They are probably the simplest far-field nanoscopy approaches to implement because they require just uniform laser illumination, a freely running camera and appropriate software⁷. Another important aspect of localization microscopy is the requirement of specialized fluorophores which can be photoactivated by lasers so that only a few fluorophores are on at a certain time point.

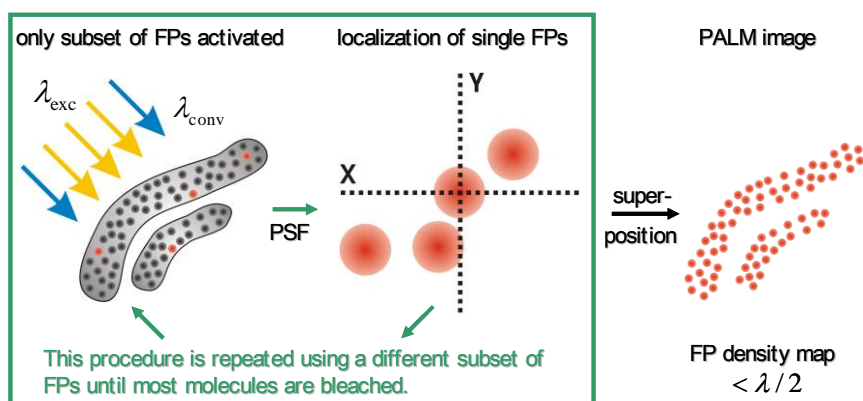


Figure 1.6 Schematic depiction of localization microscopy. Only a subset of fluorescent proteins is activated and localized with a precision of a few ten nanometers, depending on the brightness of the fluorophores. This process is repeated up to several thousand frames so that a large number of fluorophores can be localized. The final super-resolution image is a superposition of all individual. Image adopted from Ref. [74].

1.3.2.3.1 Limitations of Localization Microscopy

The main principle of localization microscopy is to sequentially image sparse subsets of photoactivatable molecules. Positions of individual molecules are precisely computed from low resolution molecular Airy patterns with subdiffraction accuracy. Unlike conventional fluorescence microscopy images, the raw data of these sparse patterns cannot be visualized directly. Instead, an additional data processing step is needed. In the beginning, the computational step took from several hours to days for a single dataset⁷⁵. Real time visualization of super-resolution images was impossible.

Owing to the intrinsic trade-off between spatial and temporal resolution, the temporal resolution is limited by the number of images needed for reconstructing a structure with a desired resolution. Although video-rate localization microscopy has been reported recently⁷⁶, such techniques are still limited by the brightness and fast blinking of the fluorophores due to the inherent nature of localization microscopy for collecting enough individual locations to reconstruct the structure. For most cases, the temporal resolution of this technique is in the range of seconds to tens of seconds depending on the complexity of the structure.

1.3.2.3.2 Photoactivatable Fluorescent Proteins (PA-FPs)

Fluorescent proteins of the green fluorescent protein (GFP) family consist of ~ 230 amino acids. They fold into a so-called beta-barrel. Its chromophore is formed from three amino acids, *e.g.*, serine, tyrosine and glycine for the GFP. One of the most interesting developments of fluorescent protein research has been the discovery of photoactivatable fluorescent proteins, which change color or emission intensity after external photon stimulation. EosFP, from the stony coral (*Lobophyllia hemprichii*), was used for super-resolution imaging in the present work. The fluorescence of the green form of EosFP stems from the chromophore formed by tyrosine, glycine and histidine

(**Figure 1.7**). After exposure to 405 nm light, an irreversible spectral shift of the excitation is induced from 506 nm to 569 nm while the emission is shifted from a green state (516 nm) to an orange state (581 nm) by the cleavage of peptide backbone between N_{α} and C_{α} of the histidine⁷⁷. It is the most commonly used PA-FP for super-resolution imaging as it has the highest contrast to the background and has been engineered into monomeric forms that are suitable for fusion constructs⁷⁸.



Figure 1.7 Mechanism of shifting the emission of the EosFP chromophore from green to red. Photoinduced cleavage of histidine extended the emission maximum from 516 nm to 581 nm. Image adopted from Ref. [79].

1.4 Outline of this Work

Interactions between NPs and cells are difficult to explore. Both high spatial and temporal resolution are needed to observe these processes in living cells. To realize this goal, we have started by further advancing super-resolution and high time resolution microscopy techniques and applied these methods to cellular experiments. This work involves the implementation of advanced algorithms to speed up the analysis software, the implementation of novel hardware components including 3D multicolor super-resolution microscopy, fast scanning devices and suitable control software in our existing experimental systems. The advanced techniques were then employed in systematic studies of NP-cell interactions.

In the cell imaging experiments, we have investigated the uptake of fluorescent NPs. We have used both bare NPs and NPs coated with Tf to enhance the interaction with the membrane bound TfR. The TfR regulates cell growth and cellular uptake of iron from Tf. Although TfR is probably expressed in all cells, it is overexpressed in many types of cancer cells. About 100-fold higher expression levels in cancer cells than the normal cells have been reported⁸⁰. Therefore, Tf has been used as one of the most promising cancer-targeting agents in various delivery systems. Many Tf conjugated NPs have been evaluated in clinical trials. Examples include: CALAA-01 (Tf-conjugated cyclodextrin polymer-based NPs was in a Phase I clinical trial), MBP-426 (Tf-bound liposome containing the cytotoxic platinum-based drug oxaliplatin is already in Phase II clinical trials), SGT-53 (a TfRscFv-conjugated liposome for delivery of p53 plasmid DNA is in Phase Ib clinical trials)⁸¹. To monitor endocytosis, clathrin was fused with mEos2. Therefore, the CCPs that are most likely involved in NP uptake could be

identified, based on the emission of mEos2. We have investigated the uptake of bare NPs and also of transferrin coated NPs to elucidate their affinity towards the transferrin receptor.

Chapter 2

Software Development of Localization Based Super Resolution Microscopy

In general, there are three steps involved in image analysis for localization microscopy: 1) molecule detection, where molecule candidates are identified and extracted from the raw image stack; 2) molecule localization, where cropped molecule candidates are localized to extract their physical parameters, most importantly, the centers of gravity of the PSF patterns; and finally 3) image reconstruction, where localized molecules are plotted as a density map depicting the spatial distribution of all emitters with a resolution well below the diffraction limit of visible light (in the range of a few tens of nanometers).

Recently, much work has been devoted to improve step 2), the localization of the individual markers, to achieve significant improvements in the precision and speed to get the center of gravity of individual molecules^{82–86}. An important aspect, which has often been overlooked in the successful application of any localization microscopy analysis is the efficiency and reliability of the identification of molecules out of the raw image for later fitting. Once molecules can be precisely localized by these advanced algorithms, the final image quality of the localization-based super-resolution microscopy critically depends on the efficiency of molecule detection, where the number of true positive molecules should be maximized while that of false positive molecules should be minimized. However, far less attention has been paid to improve the initial molecule detection step, perhaps based on the assumption that falsely identified molecules can be excluded later by rejecting badly fitted parameters (total signal counts, width of the point spread function, background, and localization precision).

Although little attention has been paid to molecule detection in the super-resolution community, molecule detection has been extensively studied in the broader image-processing field^{87,88}. In all cases, the performance of any detection algorithm critically depends on the signal-to-noise ratio (SNR)⁸⁹ and the signal-to-background ratio (SBR)⁹⁰. Setting the proper threshold for signal detection becomes a major challenge when working with biological samples, where the SNR and SBR can fluctuate during the data acquisition time and are often heterogeneous even within the same imaging area. This temporal and spatial heterogeneity in SNR and SBR distributions arises from the inherent nature of the biological sample, photobleaching of the fluorophores, or

from common technical problems, such as fluctuations of the laser intensity and inhomogeneous illumination of the sample. Typically, a molecule detection algorithm utilizes a single set of initial parameters, such as intensity count and SNR, for distinguishing the molecule pixels from the background, but often suffers from either over- or under-detecting molecules. Consequently, there is a clear need to develop a more robust approach to setting a threshold for molecule detection. In the following software development part, we will focus on algorithms for molecule detection and present our latest implementation. This work has been published in Ref. [91].

2.1 Fluorescence Image Formation and Noise Models

In fluorescence microscopy, images are generated from the fluorescence of the labels. After imaging by the objective lens, individual fluorophores which behave as point source emitters appear in the final image plane as blurred spots. Such blurred spots are relatively small and compact and have no clear borders. Classically, they can be characterized by the PSF of the system (**Figure 2.1**).

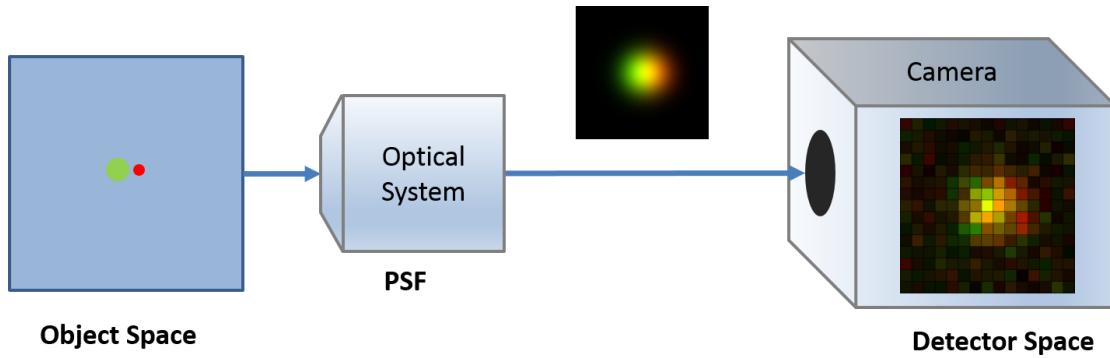


Figure 2.1 Object viewed through a microscope equipped with a camera. The image will be the convolution of the PSF and the object. During the process of recording the image in the detector array, the image quality is further deteriorated by additional noise from different sources.

There are many different models which are used to describe the PSF, accounting for the properties of the light and the optical components (*i.e.*, Richards-Wolf model⁹² and Gibson-Lanni model⁹³). However, the mathematical description of such models is often complicated. Therefore, many researchers approximate the PSF with simple model functions. The Airy function and the Gaussian function are two approximations which are most frequently used. Assuming unit magnification and that the point source is located at the origin of the object space in which it resides, the Airy profile is given by⁹⁴

$$PSF(x, y) = \frac{J_1^2\left(\frac{2\pi NA}{\lambda}\sqrt{x^2+y^2}\right)}{\pi(x^2+y^2)}, (x, y) \in R^2, \quad (2.1)$$

where NA is the numerical aperture of the microscope objective, λ is the wavelength of the emitted photons, J_1 is the first order Bessel function of the first kind and R^n , $n = 1, 2, \dots$, is the n -dimensional Euclidean space. For many practical calculations, even the Airy PSF is still too complicated. For further simplification, the 2D Gaussian profile is used⁹⁵,

$$PSF(x, y) = \frac{1}{2\pi\sigma^2} \exp\left(-\frac{x^2+y^2}{2\sigma^2}\right), (x, y) \in R^2. \quad (2.2)$$

The fluorescence is normally collected and recorded by a photosensitive detector (electron multiplying charge-coupled device (EMCCD) and scientific complementary metal-oxide-semiconductor (sCMOS) for wide field illumination, photomultiplier tube (PMT) and avalanche photodiode (APD) for point scanning). For wide-field localization microscopy, EMCCD and sCMOS cameras are normally used. The optical signal is converted eventually to electrical and digital signals. During conversion of detected photons to an electronic signal, the ideal PSF will be deteriorated by the detectors (**Figure 2.2**). First, the image is pixelated, which substantially lowers the resolution. The ideal PSF that appears in the pixelated image is considered as an integral over finite pixels given by

$$u_k(x, y) = I_0 \int_{A_k} PSF(\mu, \nu) d\mu d\nu + I_{bg}, \quad (2.3)$$

where $u_k(x, y)$ denotes the expected value in the k_{th} pixel, I_0 is the total number of photons, I_{bg} is the background noise from autofluorescence and inactive fluorescent molecules. The integral is over the finite pixel area A_k in the image plane, which is centered on (x, y) .

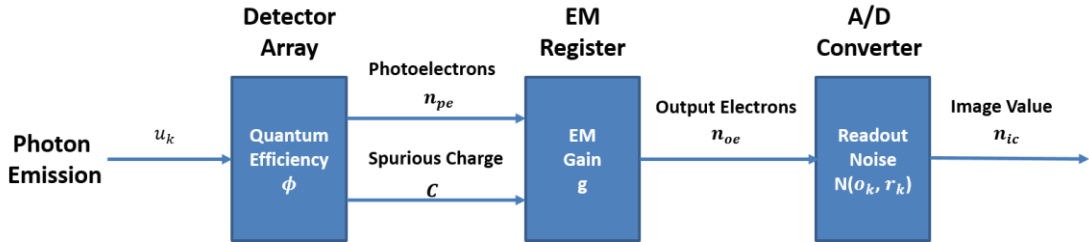


Figure 2.2 Schematic diagram of noise sources during the detection of photons. Emission of photons, u_k , from a light source following the Poissonian process is the first noise source. When a photon hits the detector array, there is a chance (ϕ) that it creates a photoelectron. This stochastic process adds the second kind of noise. The third noise source originates from spurious charge. For an EMCCD camera, the photoelectrons and spurious charges are further multiplied by the EM register, which introduces excess noise. The output electrons, n_{oe} , from the EM register are converted to the digital count, n_{ic} , by the A/D converter which introduces readout noise.

A lot of additional noise is introduced during the conversion of photons to electrons. The most common problem is shot noise. Even for constant illumination, the number of photons emitted in a given time interval is a random variable following a Poisson distribution⁹⁶. The probability that n_{ph} photons hit the detector pixel k is given by:

$$p_k(n_{ph}; u_k) = \frac{\exp(-u_k)u_k^{n_{ph}}}{(n_{ph})!} = P(n_{ph}; u_k), \quad (2.4)$$

where u_k is given by Eq. 2.3, $P(x)$ is the Poisson distribution with mean or rate x .

Each photon that hits the detector has a probability to generate a photoelectron. The probability of this event is described by the quantum efficiency, ϕ , which depends on the material of the detector and the wavelength of the incident light. The probability of obtaining n_{pe} photoelectrons from n_{ph} incident photons with quantum efficiency ϕ is given by a binomial distribution⁹⁷,

$$p(n_{pe}; n_{ph}, \phi) = \frac{n_{ph}!}{n_{pe}!(n_{ph}-n_{pe})!} \phi^{n_{pe}} (1-\phi)^{n_{ph}-n_{pe}} = B(n_{pe}; n_{ph}, \phi), \quad (2.5)$$

where $B(n, p)$ is the binomial distribution of n trials with probability p . The probability of getting n_{pe} photoelectrons from a light source is hence given by a combination of mutually exclusive events of joint probabilities of the Poisson distribution and the binomial distribution. The probability of obtaining n_{pe} photoelectrons at pixel k is given by

$$p_k(n_{pe}; u_k, \phi) = \sum_{n_{ph}}^{\infty} P(n_{ph}; u_k) B(n_{pe}; n_{ph}, \phi) = P(n_{pe}; u_k \phi). \quad (2.6)$$

The emission of a thermal and clock induced charge (CIC) is also governed by a Poisson distribution with emission rate c , which can be written as

$$c = t\dot{c}_{dark} + c_{CIC}, \quad (2.7)$$

where t is the exposure time. Therefore, an electron that enters the EM register can be either a photoelectron or a spurious charge. The probability density function (PDF) of the input electrons, n_{ie} , is the convolution of the two Poisson distributions for the photoelectrons and the spurious charge:

$$p_k(n_{ie}; u_k, \phi_k, c) = \sum_{n_{pe}=0}^{n_{ie}} P(n_{pe}; u_k \phi) P(n_{ie} - n_{pe}; c) = P(n_{ie}; u_k \phi + c). \quad (2.8)$$

For the sCMOS and the CCD camera, the input electrons are directly converted to digital counts by analog-to-digital converters (ADCs). This process will introduce readout noise. This noise can be modelled by a normal distribution with variance r_k . The image count can take negative values because of the readout noise, hence is normally offset by a factory-set positive constant, o_k , at the k -th pixel. Therefore, this noise can be modeled by $N(f(n_{ic} - o_k); n_{ie}, r_k)$ at the k -th pixel. n_{ic} is the image count, f is the A/D factor which indicates the number of electrons per image value. The PDF of the final image values is the convolution of the Poisson distribution with a

Gaussian distribution which can be described by:

$$p_k(f_k(n_{ic} - o_k); u_k, \phi, c, r_k, f_k, o_k) = \sum_{n_{ie}=0}^{\infty} \frac{1}{n_{ie}!} e^{u_k \phi + c} (u_k \phi + c)^{n_{ie}} \frac{1}{\sqrt{2\pi r_k}} e^{-\frac{[f_k(n_{ic} - o_k) - n_{ie}]^2}{2r_k}}. \quad (2.9)$$

For the sCMOS camera, o_k and r_k are different from pixel to pixel while they are the same for all pixels of the CCD camera, since all pixels are read through the same chip level output amplifier. In the EMCCD camera, extra electron multiplying (EM) processes, which can be considered as Bernoulli processes, are involved⁹⁸. Therefore, the model should be modified accordingly. EM occurs in the EM register by applying high voltages once the electrons have entered the register. The EM register contains many hundreds of cells, and the amplification process occurs in each cell via high voltage clocks. A given electron has a very tiny but finite probability to knock out another electron by a process known as ‘impact ionization’. Assuming that the probability to generate an additional electron is a and the probability of remaining unchanged is $1-a$, the total EM gain value is $(1+a)^N$ after N consecutive steps.

When the photon input level is relatively small and the gain is large, the probability to get n_{oe} output electrons from n_{ie} input electrons after an EM register with gain g follows the Gamma distribution,

$$p_k(n_{oe}; n_{ie}, g) = \gamma(n_{oe}; n_{ie}, g) = n_{oe}^{n_{ie}-1} \frac{\exp\left(-\frac{n_{oe}}{g}\right)}{\Gamma(n_{ie})g^{n_{ie}}}. \quad (2.10)$$

where $\Gamma(x)$ is the gamma function. Therefore, after the EM process, the PDF of each pixel of the EMCCD camera is the composition of the Poisson distribution and the gamma distribution,

$$p_k(n_{oe}; u_k, \phi, c, g) = \begin{cases} \sum_{m=1}^{n_{oe}} P(m; \lambda_k) \gamma(n_{oe}; m, g) & n_{oe} > 0 \\ \exp(-\lambda_k) & n_{oe} = 0, \\ 0 & n_{oe} < 0 \end{cases} \quad (2.11)$$

where $\lambda_k = u_k \phi + c$. Here, it is assumed that at least as many electrons are leaving the EM register as were entering the EM register. Therefore, the sum runs to $m = n_{oe}$.

For high gain, the composition can be approximated by

$$\begin{aligned}
p_k(n_{oe}; u_k, \phi, c, g) &= \begin{cases} \sum_{m=1}^{\infty} P(m; \lambda_k) \gamma(n_{oe}; m, g) & n_{oe} > 0 \\ \exp(-\lambda_k) & n_{oe} = 0 \\ 0 & n_{oe} < 0 \end{cases} \\
&= \begin{cases} \sqrt{\frac{\lambda_k}{n_{oe}g}} \exp\left(-\frac{n_{oe}}{g} - \lambda_k\right) I_1\left(2\sqrt{\frac{n_{oe}}{g}}\lambda_k\right) & n_{oe} > 0 \\ \exp(-\lambda_k) & n_{oe} = 0 \\ 0 & n_{oe} < 0 \end{cases} \\
&= \exp(-\lambda_k) \delta(n_{oe}) + \sqrt{\frac{\lambda_k}{n_{oe}g}} \exp\left(-\frac{n_{oe}}{g} - \lambda_k\right) I_1\left(2\sqrt{\frac{n_{oe}\lambda_k}{g}}\right),
\end{aligned} \tag{2.12}$$

where I_1 is the modified Bessel function of the first kind of order one, $\delta(x)$ is the Dirac delta function. This equation appeared in a similar form in Ref. [99]. Similar for sCMOS and CCD cameras, the readout noise is added when the electrons are converted to digital counts by the A/D converter. The PDF of the sum of two independent variables is the convolution of their separate density functions. Therefore, the PDF of the measured image value n_{ic} in the k -th pixel can be written as:

$$\begin{aligned}
p_k(f_k n_{ic}; u_k, \phi, c, g, r_k, f_k, o_k) &= \sum_{n_{oe}=0}^{\infty} \left[e^{-\lambda_k} \delta(n_{oe}) + \sqrt{\frac{\lambda_k}{n_{oe}g}} e^{-\frac{n_{oe}}{g} - \lambda_k} I_1\left(2\sqrt{\frac{n_{oe}\lambda_k}{g}}\right) \right] \frac{e^{-\frac{(f_k n_{ic} - o_k - n_{oe})^2}{2r_k}}}{\sqrt{2\pi r_k}} \\
&= \frac{e^{-\lambda_k} \left[e^{-\frac{(f_k n_{ic} - o_k)^2}{2r_k}} + \sum_{n_{oe}=0}^{\infty} e^{-\frac{(f_k n_{ic} - o_k - n_{oe})^2}{2r_k} - \frac{n_{oe}}{g}} \sqrt{\frac{\lambda_k}{n_{oe}g}} I_1\left(2\sqrt{\frac{n_{oe}\lambda_k}{g}}\right) \right]}{\sqrt{2\pi r_k}}.
\end{aligned} \tag{2.13}$$

A similar form of this equation was used in Ref. [97,100]. In practice, the noise of the EMCCD camera is often modeled using Poisson statistics only, usually achieving excellent precision⁸⁶. Such models are only an approximation of the real noise model. Only a few existing algorithms explicitly account for multiplication noise (excess noise)^{99,100}. However, Ref. [100] shows that the localization accuracy of an ultra-high accuracy imaging modality (UAIM), which considered both the excess noise and readout noise, could be improved by >200% for low-light imaging compared to conventional EMCCD modeling.

2.2 General Molecule Detection Framework

In general, the framework of molecule detection can be split into three subsequent steps: 1, noise reduction; 2, signal enhancement; and 3, signal thresholding (**Figure 2.3**). In practice, some of the steps can be combined or are optional⁸⁸.

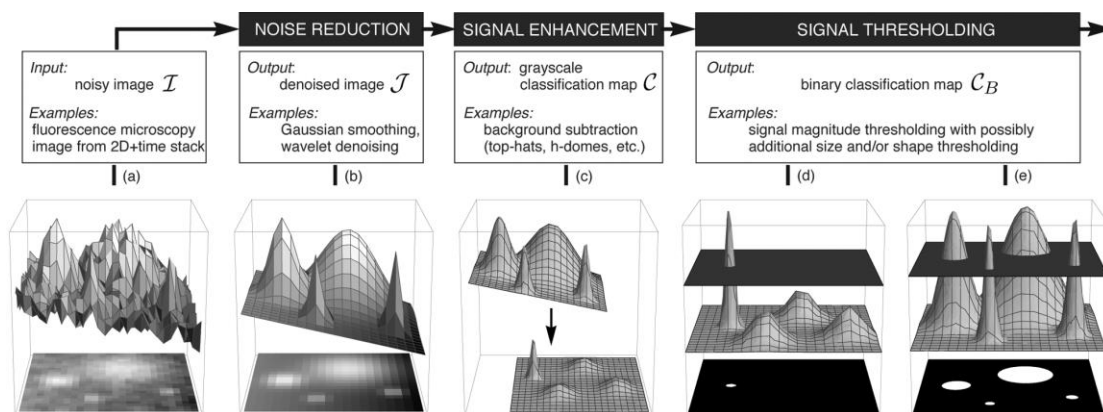


Figure 2.3 General molecule detection framework. The noise of the original image (a) is suppressed by noise reduction techniques. The resulting image (b) normally sits on a non-uniform background. A signal enhancement technique is applied to amplify the signal above the background (c). The image (c) is finally thresholded to find molecule candidates (d) and (e). Scheme adopted from Ref. [88].

- 1) **Noise Reduction:** As described in the previous section, the image quality can be degraded by various noise sources, resulting in a noisy observation of the underlying object. To reduce the effect of these errors, the image is preprocessed using noise reduction techniques. In most cases, a low pass filter for noise suppression can be applied, *i.e.*, Gaussian smoothing. Other noise reduction methods include wavelet based filtering¹⁰¹, median filtering, and path-based denoising¹⁰².
- 2) **Signal Enhancement:** Since the objects of interest are often embedded in a non-uniform background, a signal enhancement technique is used to make the objects more easily detectable than they are in the original image. Signal enhancement is the most characteristic feature of any detection method. Many methods have been developed to enhance the signal. Two types of methods can be distinguished, unsupervised and supervised signal enhancement. For unsupervised signal enhancement, frequently used methods include wavelet analysis¹⁰³, Top-Hat filter¹⁰⁴, spot-enhancing filter¹⁰⁵, H-dome based detection¹⁰⁶. Machine learning techniques are used for supervised signal enhancement, *i.e.*, the AdaBoost algorithm¹⁰⁷, Fisher discriminant analysis¹⁰⁸.
- 3) **Signal Threshold:** Finally, the object is obtained by thresholding the enhanced image. Normally, local maxima are isolated from the thresholded image. Pixels surrounding the local maxima are extracted and considered as object.

2.3 Description of the a-livePALM Algorithm

As the data analysis for image reconstruction is based on post-processing of thousands of acquired images, early versions of data analysis software for localization-based super-resolution microscopy were laborious and took many hours to analyze even one stack of images. Obviously, this made optimization of the imaging conditions (laser intensity, acquisition time, *etc.*) impossible during the experiment. Therefore, it is of utmost importance that the analysis algorithm can run at high speed to keep up with the image acquisition. As mentioned above, numerous algorithms have been developed to accelerate the analysis of super-resolution microscopy data, however, mostly in the molecule localization step^{75,85,86,109,110}. Relatively basic, hence fast, algorithms have been used for the molecule detection step, however, without a quantitative comparison. In the broader image-processing field, various molecule detection algorithms have been proposed to deal with images with a heterogeneous background^{87,88}. Naturally, an advanced molecule detection algorithm comes at the expense of added computational complexity. We have developed a fast yet efficient molecule detection algorithm termed a-livePALM for data analysis.

There are three steps to identify molecule candidates within the a-livePALM algorithm: noise reduction, local background estimation and the selection of appropriate local maxima according to the local background condition. The general outline of this process is shown in **Figure 2.4**.

For noise reduction, we convolute the raw images with a Gaussian kernel⁸⁹, which is a low-pass filter. The effect of Gaussian smoothing is to suppress the high frequency noise spikes, thus improving the SNR of the image. The degree of smoothing is determined by the standard deviation, σ , of the Gaussian (**Figure 2.5**). The σ of the Gaussian kernel depends on the dataset. Typically, we use a Gaussian kernel with $\sigma = 1$ pixel for 2D localization images and $\sigma = 1.5$ pixels for 3D astigmatic localization images.

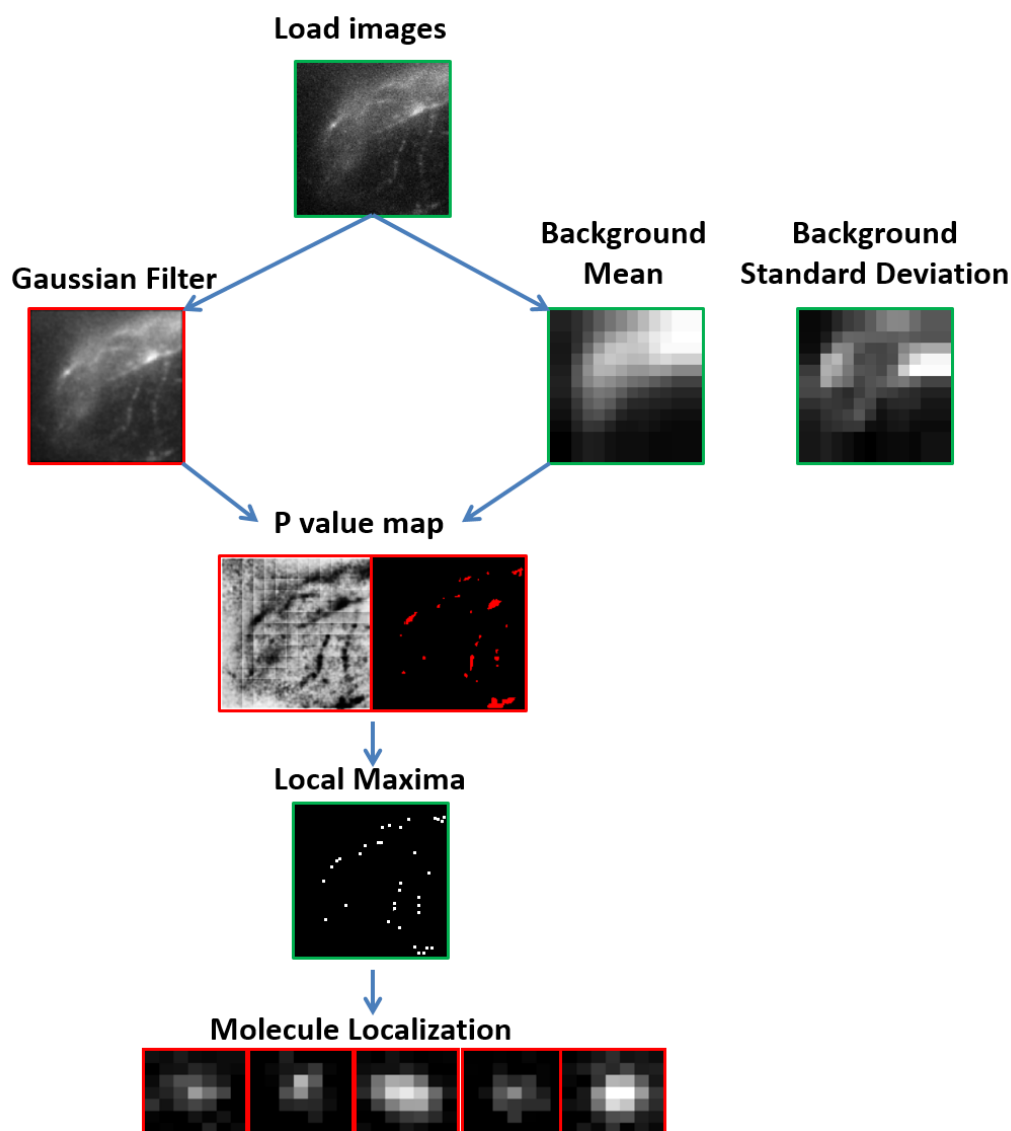


Figure 2.4 Work flow and software implementation of data processing. The green and red frames denote procedures run in central processing unit (CPU) and graphics processing unit (GPU), respectively. The images are first loaded into memory. The raw images are smoothed in the GPU, and the local background condition of the raw images is estimated in the CPU in parallel. With the smoothed raw data and local background information, the P value for each pixel is calculated and thresholded in the GPU. Then, the local maxima are determined from the pixels with P value below the threshold. The final selected molecules are localized in the GPU.

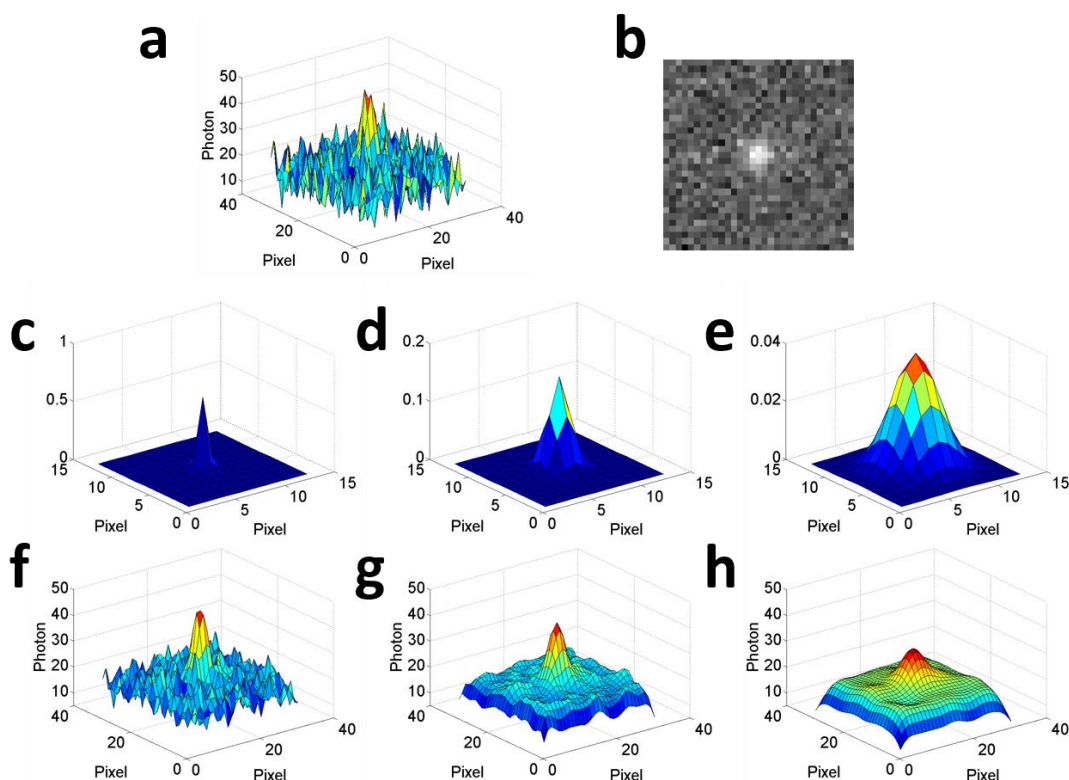


Figure 2.5 Convolution of a single molecule image with a Gaussian kernel of different σ . (a) and (b) are 3D and 2D representations of a single molecule with 500 signal photons and 10 background photons, respectively. Only Poisson noise and Gaussian noise with sigma 3 photons were added. (c), (d) and (e) depict Gaussian kernels with σ 0.5, 1 and 2 pixels. (f), (g) and (h) show the result of the convolution of the single molecule image and the Gaussian kernels in (c), (d) and (e), respectively.

To estimate the local background, each image is first subdivided into small local areas (11×11 pixels). The background of each local area is evaluated by the mean value and the standard deviation of its larger surrounding area (31×31 pixels). Using the local mean background and standard deviation, the normal cumulative distribution function (CDF) of each pixel value is calculated. The normal CDF stands for the probability of a pixel that it belongs to the molecule. Only pixels with a normal CDF above a user-defined threshold are selected, and local maxima (within 7×7 pixels) among these pixels are identified as molecule candidates. Small sub-images (7×7 pixels) around these local maxima are extracted for single molecule localization. For pixels on the boundaries, for which a 31×31 pixels surrounding area does not exist for background calculation, the background parameters were transferred from the nearest non-boundary pixels. Different P values were tested for the synthesized data (**Figure 2.6**). A P value ($P = 1 - \text{normal CDF}$) of 0.08 produced the best results for identifying molecules. Lower P values yield high precision, but lower recall (see **Section 2.7**). On the contrary, a too high P value yields a high recall, but a lower

precision. In practice, one can check for an appropriate P value by minimizing the number of molecules identified from areas void of cells (background).

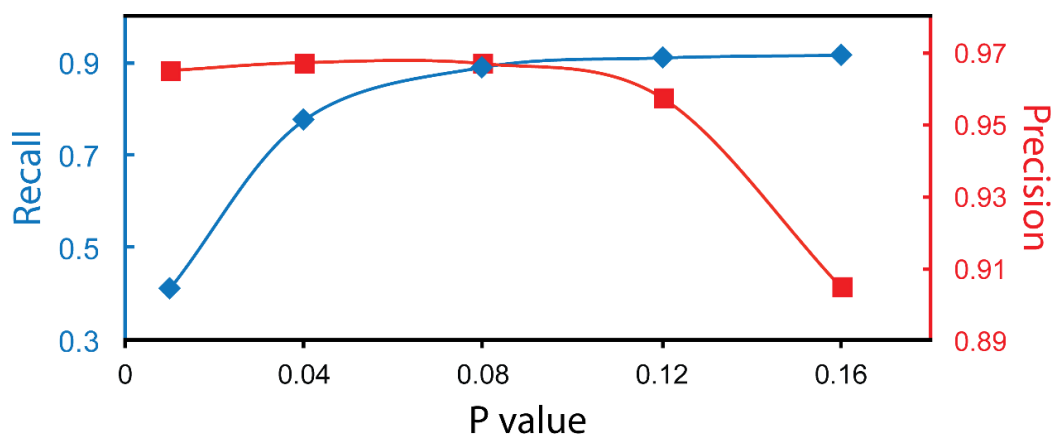


Figure 2.6 Performance of a-livePALM with different P values⁹¹. Reproduced with permission from the American Chemical Society.

After extracting the candidate sub-regions from the raw image as single molecules, those images are fitted with a model function. A two-dimensional Gaussian (plus a constant background) model was used. Many methods have been developed for molecule localization in the past years¹¹¹. Those localization algorithms can generally be divided into two types: numerical fitting (*e.g.*, least squares criteria⁶⁵, maximum likelihood criteria¹¹²) and non-fitting methods (*e.g.*, fluoroBancroft algorithm⁸², radial symmetry⁸⁴). In general, fitting methods are preferred since they offer the best localization accuracy. Though the non-fitting methods are computationally simple, the bottleneck for localization microscopy often lies on the molecule detection but not the molecule localization. We employed the GPU-based maximum likelihood estimator (MLE) algorithm for single molecule localization which can fit more than 200 molecules/ms⁸⁶. It also achieves theoretically minimum uncertainty (Crámer-Rao lower bound, CRLB). The molecule localization only consumed $\sim 10\%$ of the overall analyzing time. Therefore, the speed of the molecule localization algorithm is currently not the limitation of the software development.

It is worth pointing out that the noise model employed in Ref. [86 models the noise only with Poisson statistics. A more accurate model which accounts for multiplication noise (excess noise) for EMCCD has also been proposed^{97,100} (Eq. 2.13). However, such models are normally very difficult to implement into GPU. The simplified noise model which only accounts for Poisson noise has also been widely used^{85,86}. For the sCMOS camera, Gaussian readout noise should be added⁷⁶. As shown in Eq. 2.9, the PDF of the image value is the convolution of a Poisson distribution and a Gaussian distribution. By adding a pixel-dependent constant, r_k , the PDF can be rewritten as

$$\begin{aligned}
p_k (f_k(n_{ic} - o_k) + r_k; u_k, \phi, c, r_k, f_k, o_k) \\
= P(\phi u_k + c) \otimes N(r_k, r_k).
\end{aligned} \tag{2.14}$$

The normal distribution $N(r_k, r_k)$ can be further approximated by $P(r_k)$. Therefore, since the convolution of two Poisson distributions with expected values a and b is still a Poisson distribution with expected values $a+b$, we could approximate the PDF of the image values as

$$\begin{aligned}
p_k (f_k(n_{ic} - o_k) + r_k; u_k, \phi, c, r_k, f_k, o_k) \approx P(\phi u_k + c) \otimes P(r_k) \\
= P(\phi u_k + c + r_k).
\end{aligned} \tag{2.15}$$

Therefore, by using the analytical approximation of the PDF of the full likelihood function for the sCMOS camera as described by Eq. 2.9, one can greatly simplify the calculation while providing optimal accuracy and precision at the theoretical limit⁷⁶.

The final super-resolution image is reconstructed from fitted positions of the detected molecules. However, many fluorophores may have non-negligible light-induced fluorescence recovery and may be in the on state for many frames¹¹³. Photoblinking or light-induced reactivation of a single molecule may be erroneously interpreted as biological clusters¹¹⁴. As an example, we have plotted the PALM image of signalosomes¹¹⁵ formed by LRP6 molecules fused to mEosFP*thermo*¹¹⁶ (**Figure 2.7**). **Figure 2.7a** is the map of all localized events, and the color identifies the temporal instant of the molecular localization. We found that several molecules seemed to cluster in both space and time, which is an indication of events from the same molecule. If we group these events (**Figure 2.7b**), temporal clusters disappeared, yielding only a big cluster in space.

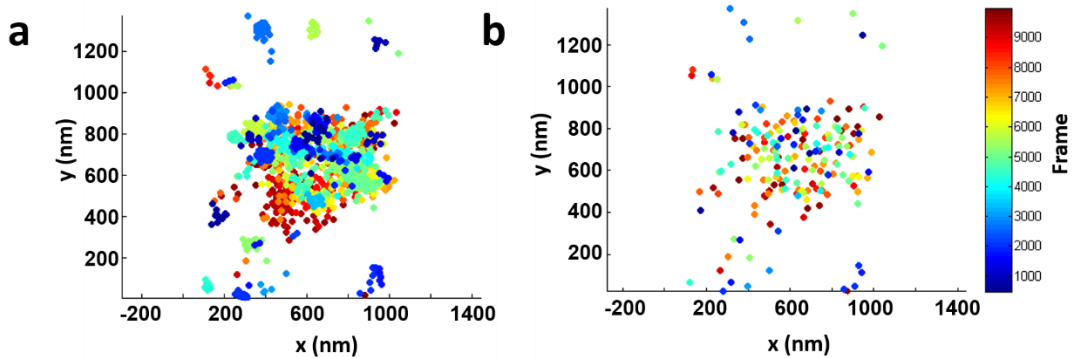


Figure 2.7 Plot of a PALM image of LRP6-mEosFP*thermo* with and without grouping. (a) Map of localized emission centers for all events detected. The color scale identifies the temporal instant. (b) Map of the same data after grouping with a dark time of 2 s and 100 nm distance between events.

Therefore, before plotting the localized molecules in the final reconstructed super-resolution image, we first grouped the events which were temporally and spatially close. In practice, molecules that appear in n successive frames and are spatially close (<100 nm) are considered to be identical, but not stationary. In the final super-resolution image, the molecule is plotted n times with the weighted value $1/n$ so that the intensity of the reconstructed image represents the real density of the molecules.

2.4 Comparison of a-livePALM and DAOFIND

Although there are many (F)PALM/STORM analysis programs available in the field, “DAOFIND” has been the most frequently used algorithm for molecule detection^{67,68,75,85,117,118}. In order to directly compare the “DAOFIND” algorithm and a-livePALM, we show the schematic workflow of both algorithms in **Figure 2.8**. In both approaches, the raw image (**Figure 2.12**) is first convoluted by a Gaussian kernel for noise reduction⁸⁹ (**Figure 2.8a**). DAOFIND directly identifies molecule candidates in the convoluted image by setting a threshold based on the SNR for each pixel upon its local background (**Figure 2.8b**). This step is time consuming since this process is performed for each pixel and cannot be parallelized. Instead of setting a threshold to the SNR, a-livePALM performs the adaptive histogram equalization technique for each pixel. We calculate a P value (**Figure 2.8f**) for each pixel using the standard deviation (**Figure 2.8d**) and the mean background of its surrounding region (**Figure 2.8e**). In practice, the image is divided into different blocks and the background is assumed to be constant in each block. After estimation of the background for each block, the P value calculation can be parallelized to speed up the analyzing process. The P value represents the probability of the pixel to be part of the surrounding background. Local maxima with a P value below the threshold are assigned to molecule candidates (**Figure 2.8g**). Squares and white dots in **Figure 2.8c** and **g** represent coordinates of molecule candidates identified by the algorithm and the actual coordinates of simulated molecules, respectively.

Another advantage of a-livePALM is that the P value is insensitive to changes of the SNR and the SBR, and significantly enhances the signal contrast without introducing noise peaks. In order to show the performance of the signal enhancement methods used by DAOFIND and a-livePALM, we generated an image of five molecules placed over a linearly increasing background and processed it by the DAOFIND and a-livePALM algorithms separately (**Figure 2.9**). The intensity profile of the molecules in the absence of noise is shown in **Figure 2.9a**. By adding linearly increasing background and Poisson noise to the molecules, a significant decrease of contrast is generated in the intensity profile (**Figure 2.9b**). The DAOFIND algorithm takes the Gaussian-convoluted image from **Figure 2.9b** and generates the SNR map for each pixel. A top-hat filter with grayscale opening was used to generate the SNR map (**Figure 2.9c**). However, background features are also stochastically enhanced in a way that resembles

signals from actual molecules. This could lead to registration of false positive molecules. For comparison, the P value map from the a-livePALM adaptive histogram equalization algorithm and its corresponding intensity profile are shown in **Figure 2.9d**. The contrast of the molecule signals is evenly enhanced over the entire image, and their intensity profile is easily distinguishable from the background.

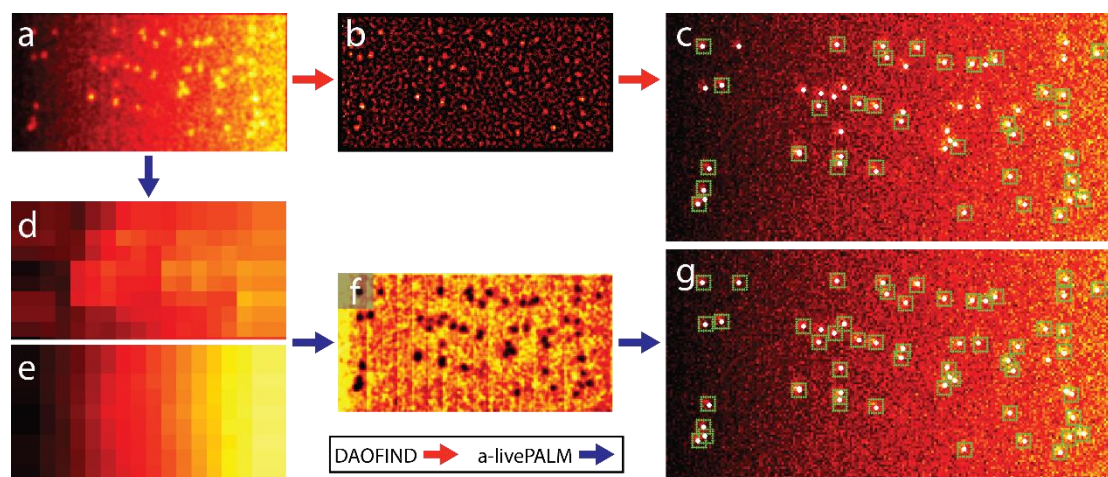


Figure 2.8 DAOFIND and a-livePALM molecule detection algorithms for localization microscopy. The red and blue arrows denote procedures run in DAOFIND and a-livePALM, respectively. In DAOFIND, the raw image is first convoluted with a Gaussian filter (a). The SNR for each pixel is calculated (b) and a threshold is set to identify molecule candidates (c). In a-livePALM, the local background parameters (standard deviation (d) and mean (e)) are computed from the raw image (**Figure 2.12**). A P value is calculated for every pixel (f). Molecule candidates are identified as local maxima with the P value below the chosen threshold (g)⁹¹. Reproduced with permission from the American Chemical Society.

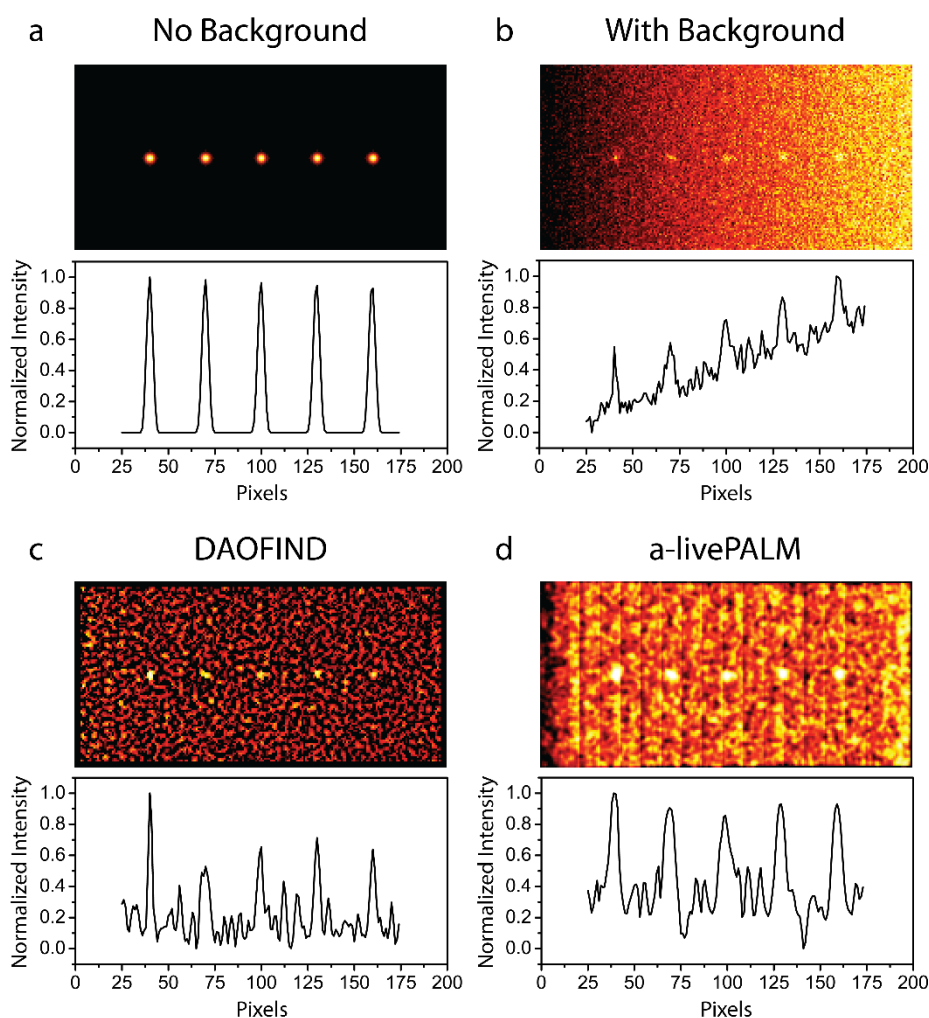


Figure 2.9 (a) Simulated image of five molecules without background (top). This intensity profile (bottom) serves as a reference. (b) Image after adding a linearly increasing background and Poisson noise (top) and its intensity profile (bottom). (c) SNR map of DAOFIND (top) and its intensity profile (bottom). (d) P value map of a-livePALM algorithm (top) and its intensity profile (bottom). The color scale of the P value map (d top) has been inverted in order to directly compare it with the other SNR maps⁹¹. Reproduced with permission from the American Chemical Society.

2.5 Software and Hardware Implementation

To avoid slowing of the analysis while maintaining performance, we have coded our algorithm so that it utilizes the parallel processing power of GPU for the molecule detection step. As a result, the software can achieve comparable processing speed to state-of-the-art fast software even with the additional background estimation (**Figure 2.10**).

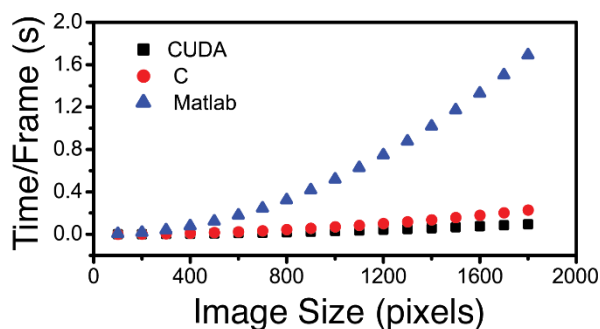


Figure 2.10 Benchmarking comparison of the a-livePALM algorithm implemented in Matlab, C and CUDA (GPU processing)⁹¹. Reproduced with permission from the American Chemical Society.

The data processing procedures were run in MATLAB R2010b (The Mathworks, Natick, MA, USA) environment. The workflow of the program is shown in **Figure 2.11**. Both the CPU based C-code (green boxes) and the GPU based C-code (red boxes, Nvidia CUDA, http://www.nvidia.com/object/cuda_home.html) are compiled to MATLAB mex files. The local background estimation (CPU) and the Gaussian noise filtering of the image (GPU) are run in parallel since those computations are totally independent of each other. On the basis of the background parameters and the denoised image, the normal CDF of each pixel is calculated in the GPU. Pixels with P values below a certain threshold are selected, and the local maxima among these pixels are determined as molecule candidates. The arrays around the candidates are extracted and finally passed into the GPU global device memory for single molecule localization.

The software is currently run on a personal computer using an Intel(R) Core(TM) i7-2600 processor clocked at 3.40 GHz with 8.0 GB memory. A NVIDIA GeForce GTX 560Ti graphics card with 1.0 GB memory was used for GPU based computation. For a typical image size of 512×512 pixels, acquired by the electron-multiplying charge-coupled device (EMCCD) camera, the processing time is 15 – 30 ms per image, depending on its complexity. The speed is comparable to the maximum full frame rate of current EMCCD cameras and, therefore, allows real-time data processing.

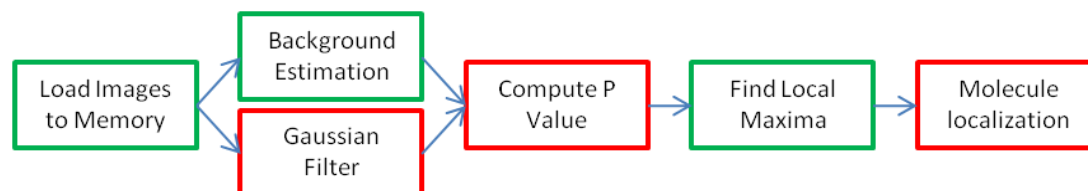


Figure 2.11 Software and Hardware Implementation. In this flow chart, procedures run in CPU and GPU are depicted by green and red boxes, respectively⁹¹. Reproduced with permission from the American Chemical Society.

2.6 Image Simulation

To evaluate the performance of super-resolution algorithms, synthesized test images are routinely used^{13,14}. Therefore, we simulated single fluorescence emitters with varying SNR and background to assess the performance of the search algorithm. Considering the finite pixel size, the final simulated signal is given by

$$F_{i,j} = \text{Pois}(I_0 \int_A \text{PSF}(\mu, \nu) d\mu d\nu + bg_{i,j}) \quad (2.16)$$

Here, $\text{Pois}(x)$ is a Poisson random number with a mean value of x . I_0 is the number of photons emitted by a given fluorophore. The integral extends over the area of each pixel, A . The point spread function, $\text{PSF}(x, y)$, is approximated by a two-dimensional Gaussian function, Eq. 2.2. The background noise in each pixel (*e.g.*, from diffusing impurity molecules or thermal noise),

$$bg_{i,j} = N_{bg} + N_{i,j}(\delta) \quad (2.17)$$

is modeled by a constant background or a linearly increasing background, N_{bg} , and is additionally varied by Gaussian noise, $N_{i,j}(\delta)$, with standard deviation, δ . All simulated images were generated by using MATLAB.

Molecules with different SNR and SBR were synthesized within the same image to model heterogeneous background. We generated 1,000 images (200×100 pixels) with simulated molecules (150 – 250 photons per molecule) randomly placed on a linearly increasing background (1 – 25 photons). This is the raw simulated image used to show the analysis procedures in **Figure 2.8**. We varied the molecule density from 0.1 to 1 molecule/ μm^2 (16 – 160 molecules/image). **Figure 2.12** is an example image with 0.5 molecule/ μm^2 .

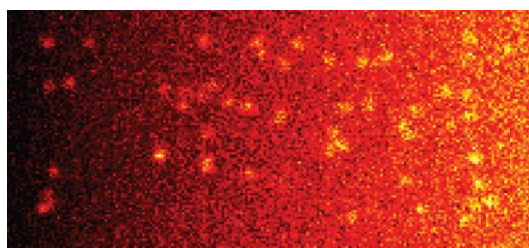


Figure 2.12 Raw image of simulated randomly distributed molecules⁹¹. Reproduced with permission from the American Chemical Society.

In order to quantify the performance of the software under different background conditions, we also simulated molecules with different SNR and SBR in the same image (**Figure 2.13**). Each molecule was randomly plotted in the center (10×10 pixels) of a block (30×30 pixels). Three types of molecules ($I_0 = 150, 200$ or 250 photons) were used for the evaluation. For each molecule, the background level (N_{bg}) was varied from 2 – 20 photons with the standard deviation of the additional Gaussian noise, δ , of 1, 2

or 3 photons. The resulting SNR of the final image ranges from 1.3 to 3.3; the SBR ranges from 0.4 – 6.8. The SNR of a molecule is defined as $SNR = (I - bg) / \sigma^{119}$, where I and bg are the maximum intensity of the single molecule signal and the background, respectively; σ is the standard deviation of the background.

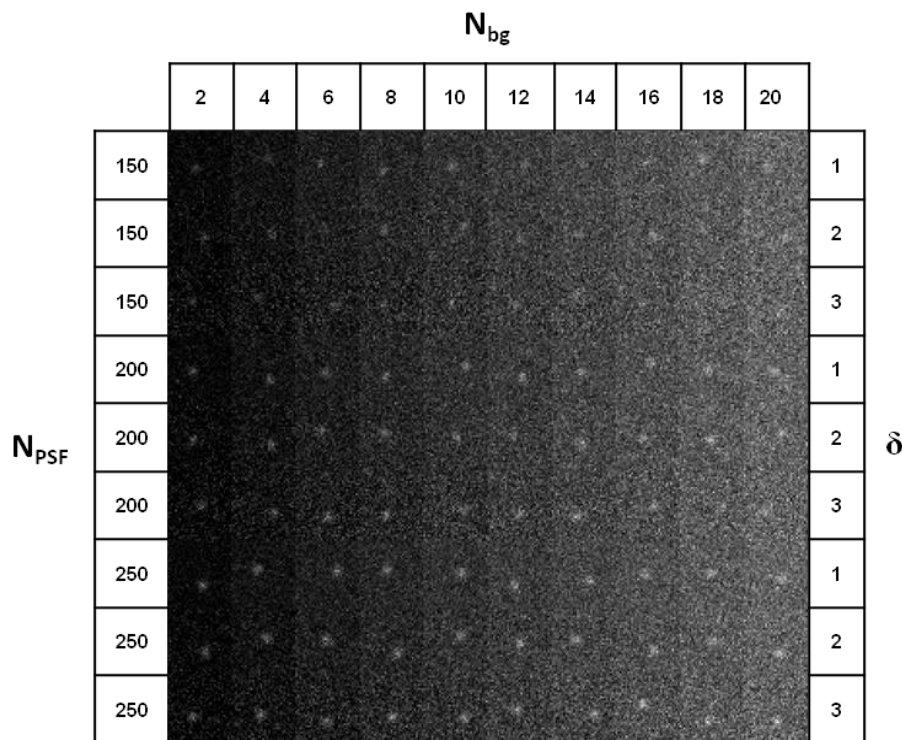


Figure 2.13 The upper row states the background level, N_{bg} (Eq. 2.17), of each column. The left column denotes the number of photons contributing to the signal of the molecules in the corresponding row. The right column indicates the standard deviation, δ , of the Gaussian background noise in the corresponding row. Each sub-block has a size of 30×30 pixels, and the molecule is plotted randomly within the center 10×10 pixels to exclude overlap. The width of the point spread function of the simulated molecules (Eq. 2.2) is fixed at $\sigma = 1.69$ pixels, which corresponds to the theoretical value of a molecule with a fluorescence emission at 581 nm, imaged by an objective lens with a numerical aperture of 1.46⁹¹. Reproduced with permission from the American Chemical Society.

2.7 Performance Assessment

2.7.1 Recall and Precision

There are two types of errors for molecule detection algorithms: false negative molecules and false positive molecules (**Figure 2.14**). Correctly detected molecules are defined as true positive molecules with returned coordinates within a certain distance (D) of the actual coordinates. Molecules outside of D are classified as false positive

molecules. Actual molecules without any returned coordinates within D are called false negative molecules. Two parameters, recall and precision, are employed to evaluate the performance of the search algorithm. They are defined as:

$$recall = \frac{\text{true positives}}{\text{true positives} + \text{false negatives}} \quad (2.18)$$

$$precision = \frac{\text{true positives}}{\text{true positives} + \text{false positives}} \quad (2.19)$$

The theoretical optimum for the detection algorithm is that both recall and precision are equal to 1. For comparison of different algorithms, the F -measure, which combines both precision and recall, was introduced:

$$F = 2 \times precision \times recall / (precision + recall) \quad (2.20)$$

Low values of F indicate both bad recall and precision while values approaching the theoretical optimum, 1, correspond to good recall and precision.

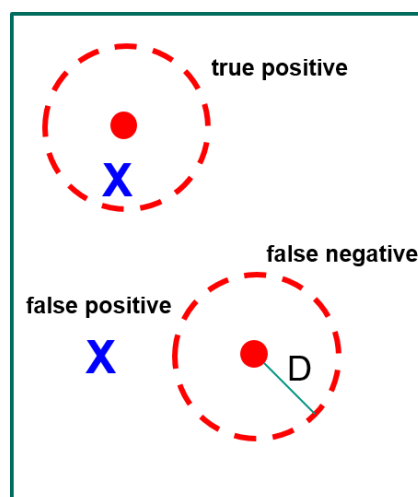


Figure 2.14 Typical detection errors for molecule detection algorithms. Red dots are actual simulated molecules, blue crosses are detected candidate molecules, and dashed circles indicate the defined threshold distance D , which is the maximum allowed distance between true positive molecules and actual molecules.

2.7.2 Software Comparison

In order to assess the efficiency and accuracy of the molecule detection, we compared a-livePALM against our previously published algorithm, livePALM¹¹⁰, and several publically available fast programs: QuickPALM⁷⁵, MaLiang⁸⁵ and rapidSTORM¹⁰⁹. 1000 images (100×200 pixels) with molecules randomly placed over a linearly increasing background (**Figure 2.12**) were simulated using the method described in section 2.6. This was repeated for different molecule densities ($0.1 - 1$ molecule/ μm^2).

2.7.2.1 Parameter optimization for the different softwares

In order to get the best overall performance, different parameters were tested for the three publicly available algorithms, QuickPALM, MaLiang and rapidSTORM. The tested dataset was the same as the one used in **Figure 2.12**, with a molecule density of $0.5 \text{ molecules}/\mu\text{m}^2$. Recall and precision performance for different parameter values are shown in **Figure 2.15**.

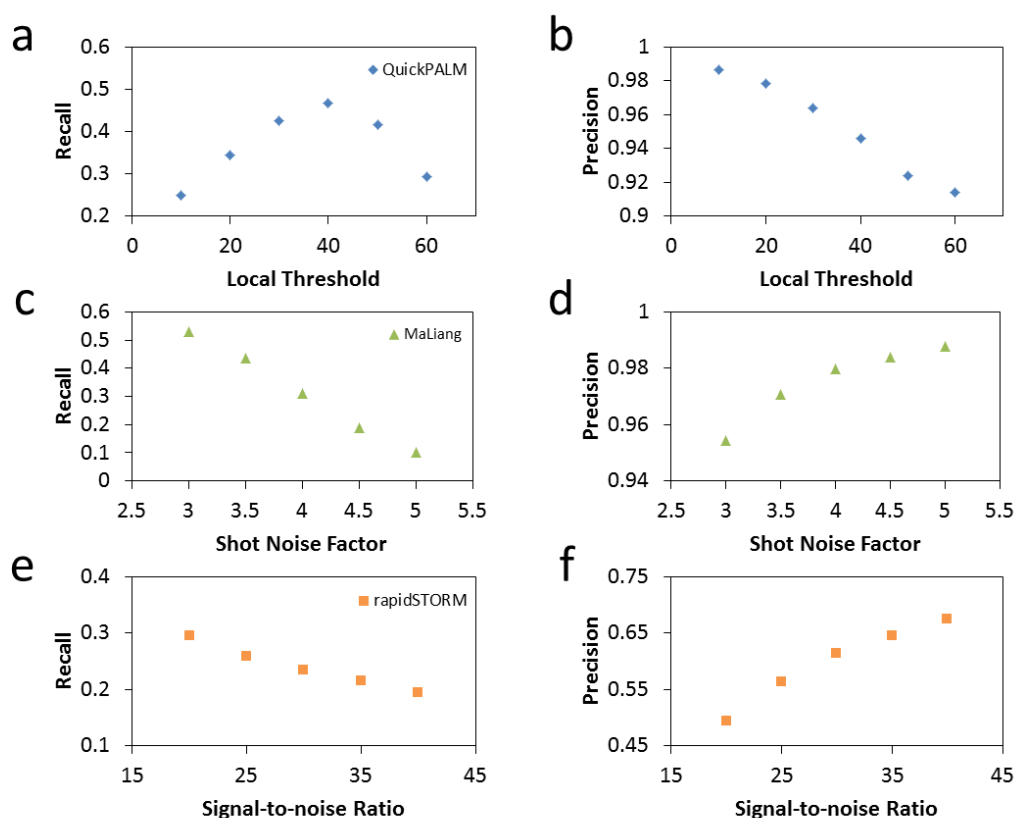


Figure 2.15 Parameter optimization for QuickPALM, MaLiang and rapidSTORM, (a) and (b) recall and precision as a function of local threshold for QuickPALM, (c) and (d) recall and precision as a function of shot noise factor for Maliang, (e) and (f) recall and precision as a function of signal-to-noise ratio for rapidSTORM⁹¹. Reproduced with permission from the American Chemical Society.

For QuickPALM, the result did not vary much with a change of the minimum SNR as long as an adequate SNR was selected (**Figure S1**). Therefore, we varied another parameter, the local threshold. The recall and the precision results are shown in **Figure 2.15(a)** and (b). We finally selected a local threshold of 40, which showed the highest F value.

For MaLiang, we kept the photon threshold relatively low, and assessed the performance of the algorithm by changing the shot noise factor (**Figure S2**). Thus, most of the molecules that exceeded the user-defined shot noise factor were taken as

molecule candidates. The recall and the precision results are shown in **Figure 2.15c** and **d**. Even though the highest F value was reached at a shot noise factor of 3 for this dataset, this setting did not perform well for the dataset with a molecule density of 0.1 molecules/ μm^2 (the precision was only 0.65). There seems to be a slightly different optimal setting for each dataset for this program. We finally decided to use a value of 3.5 as the shot noise factor.

For rapidSTORM, the performance was optimized by varying the signal-to-noise ratio parameter. The recall and precision results are shown in **Figure 2.15e** and **f**. They changed in an anti-correlated manner with small differences in F values (average 0.34 ± 0.02). We, therefore, chose a default value of the signal-to-noise ratio of 30. Other parameters used for rapidSTORM may be found in **Figure S3**.

2.7.2.2 Threshold Distance Selection

Different D values were also tried since different softwares have different sensitivities to the D value. Recall and precision performance results using $D = 1$ pixel (**Figure 2.16a** and **b**) and 0.5 pixel (**Figure 2.16c** and **d**) are shown. Both the recall and precision deteriorated when D was set to a lower value. However, different algorithms showed different sensitivities to a change in D value. In comparison to $D = 1.5$ pixel (**Figure 2.17**), the precision performance was nearly the same when $D = 1.0$ pixel was used. However, the precision of QuickPALM was outperformed by MaLiang, livePALM and a-livePALM when D was decreased to 0.5 pixel. This is most likely due to the fact that different molecule localization methods were utilized for different algorithms. For MaLiang, livePALM and a-livePALM, maximum likelihood estimation is used. QuickPALM only uses an algebraic solution for the final single molecule localization without any numerical fitting. Higher localization precision makes the software less sensitive to the D value.

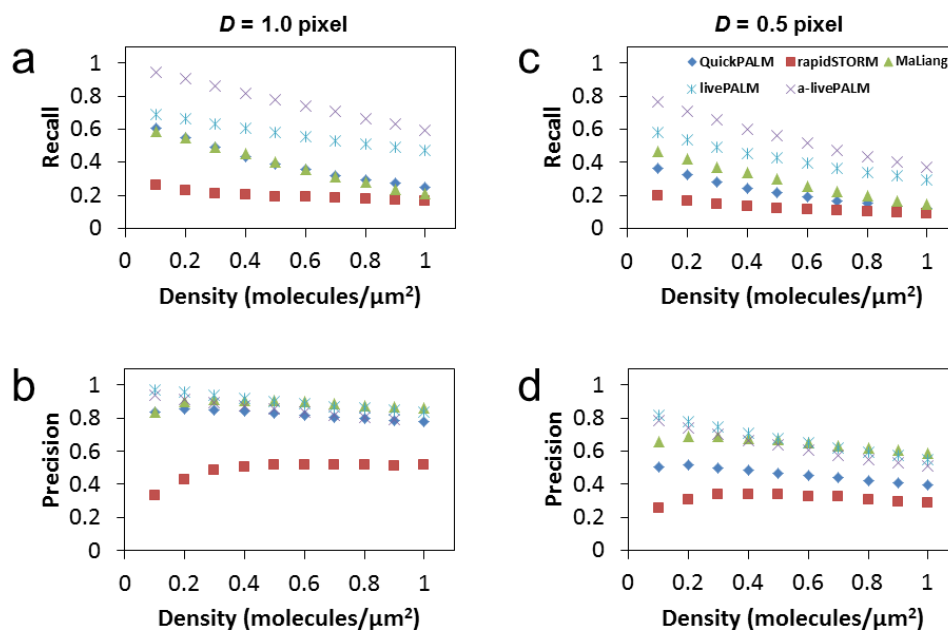


Figure 2.16 Algorithm performance with different D values. (a) and (b) Recall and precision for $D = 1.0$ pixel. (c) and (d) Recall and precision for $D = 0.5$ pixel⁹¹. Reproduced with permission from the American Chemical Society.

2.7.2.3 Recall and Precision Performance

To account for the fact that the different algorithms compared in this work use different molecule localization methods, we chose a rather large value of 1.5 pixels for D to minimize the influence of this variable on recall and precision. Recall and precision results are plotted as a function of molecule density (**Figure 2.17a** and **b**). The optimized parameters were used for each software as described before. The selected parameters used for the performance evaluation on our data are shown in **Figure S1 – 3**. In general, except for rapidSTORM, the precision was high over the entire range of the molecule density, while the recall rapidly dropped as the density increased. Among all, our new algorithm, a-livePALM, showed the highest efficiency (recall) in identifying molecule candidates while maintaining a high precision.

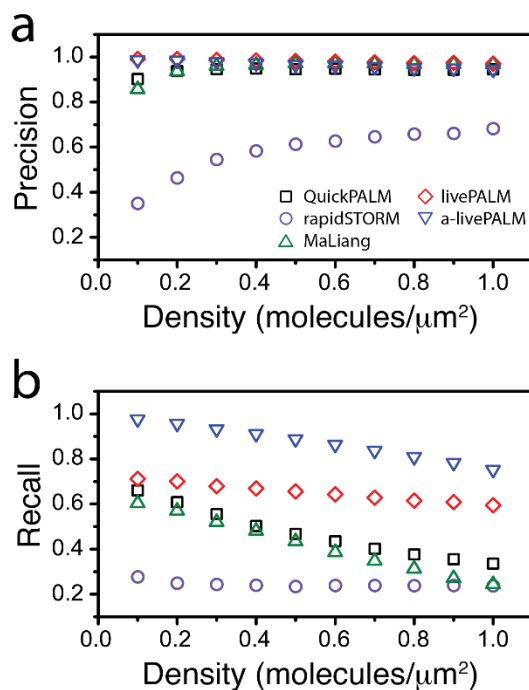


Figure 2.17 A set of simulated data images with varying molecule densities has been analyzed by the QuickPALM, RapidSTORM, MaLiang, livePALM and a-livePALM algorithms. Performances of these algorithms were evaluated by analyzing their precision (a) and recall (b)⁹¹. Reproduced with permission from the American Chemical Society.

To directly quantify the molecule detection performance of the algorithm, we tested two of the best algorithms from the first evaluation, livePALM and a-livePALM, on a different set of simulated molecules (intensity, I_0 , of 150, 200 or 250 photons) that are well separated from each other, placed over a range of background conditions (Gaussian noise, $N_{i,j}(\delta)$, and background (BG) level, N_{bg}) within the same image. A sample image is shown in **Figure 2.12**. To allow for a meaningful comparison of the molecule detection algorithm between livePALM and a-livePALM, we used the same molecule localization algorithm, the maximum likelihood estimation method⁸⁶. We conducted the molecule search on simulated images using two different thresholding methods for livePALM. The search parameters (low photon threshold and SNR) of livePALM were adjusted to either yield a high precision (precision >0.90 for over 50% of molecules, precision optimized, PO, **Figure 2.18b** and e) or to yield the high recall efficiency (maximum recall, recall optimized, RO, **Figure 2.18c** and f). a-livePALM (**Figure 2.18d**) and livePALM PO (**Figure 2.18e**) showed a comparable result for the precision, but a markedly lower recall for livePALM PO as the background level increased (**Figure 2.18b**). The recall also deteriorated as the number of photons decreased and the Gaussian noise increased. For livePALM, the recall of molecules with only 150 photons was low, especially at high background. The precision values computed from these few molecules were more prone to fluctuations and could result in non-incremental changes

in the precision with varying BG levels (**Figure 2.18e**). a-livePALM showed a high level of recall for the entire range of imaging condition. In real experiments, the recall should be maximized to improve the final image quality of the biological structure of interest. The recall can be improved by using the livePALM RO condition (**Figure 2.18c**), however, only at the expense of its precision performance (**Figure 2.18f**). These comparisons demonstrate the overall high efficiency and reliability of a-livePALM over wide ranges of SNR and SBR while using only a single thresholding parameter.

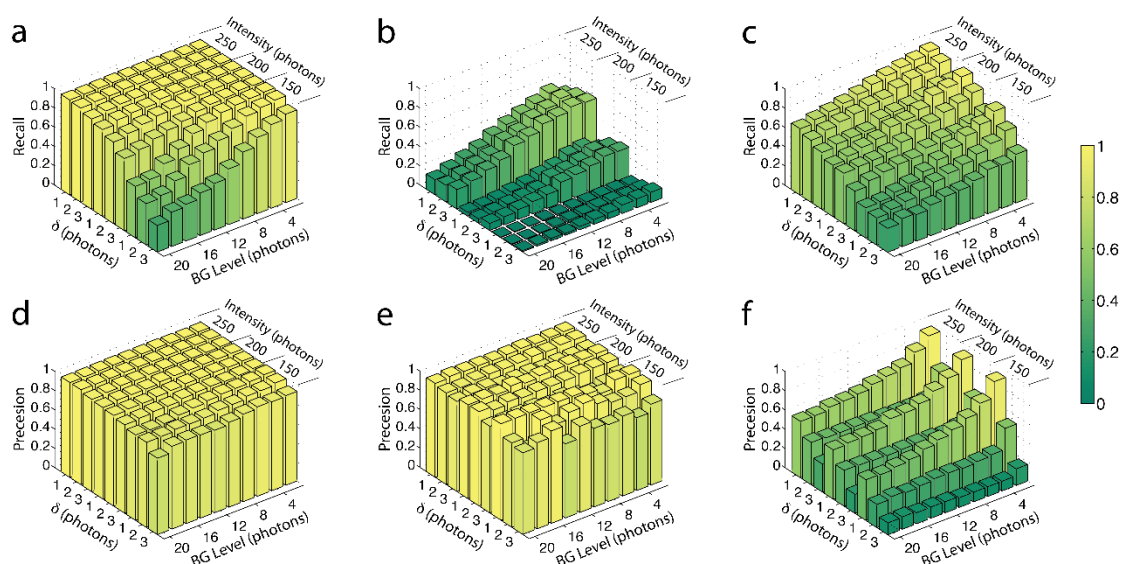


Figure 2.18 Recall and precision performances of the molecule detection algorithms. Three different sets of molecules (intensity of 150, 200 or 250 photons) synthesized over different background (BG) levels (2 to 20 photons) with additional standard deviation (δ) of Gaussian noise (1, 2 or 3 photons) were tested by a-livePALM and livePALM. The molecule detection performance evaluated by recall and precision values from a-livePALM (a, d), livePALM based on PO threshold condition (b, e) and livePALM based on RO threshold condition (c, f) are shown⁹¹. Reproduced with permission from the American Chemical Society.

2.7.2.4 Molecule Rejection by Post-filtering

One assumption is that the overall precision of the coarsely selected molecule data set can still be improved if false positive molecules can be efficiently filtered. Molecule filtration is routinely done by rejecting molecules with bad returned fit parameters¹²⁰. However, the efficiency of molecule rejection has not been discussed in the literature. Therefore, we took the data set which yielded $\sim 50\%$ precision using livePALM analysis from **Figure 2.18** with the following image condition: intensity 150 photons, $N_{bg} = 12$ photons and $\delta = 1$ photon.

The distribution of returned fit parameters for the number of photons per molecule (**Figure 2.19a**), background photons (**Figure 2.19b**), width of the point spread function, σ (**Figure 2.19c**), and localization precision (**Figure 2.19d**) are shown. Red and blue

bars represent false positives and true positives, respectively. The strongly overlapping distributions imply that false positives cannot be identified unambiguously. The number of photons of true positive molecules (**Figure 2.19a**) has a distribution centered at ~ 150 photons. In contrast, for false positive molecules, the distribution of photons peaks at lower photon numbers (~ 50) but has a long tail, so there is significant overlap (30%) between the two distributions. The distribution of background levels peaks at ~ 12 photons for true positive molecules, in close agreement with the background parameter used to generate the data image. The maximum is slightly lower, at ~ 11 photons, for false positives. The distribution of the PSF width parameter σ (**Figure 2.19c**) mainly covers the range between 1.1 and 1.9 pixels for true positives, whereas a large fraction of false positive molecules has $\sigma < 1$ pixel. There is, however, 44% overlap. The distribution of the localization precision (**Figure 2.19d**) is located at lower values for true than for false positive, but there is still 38% overlap.

Since the single fit parameters show strong overlap with each other for the true positive and false positive molecules, we still found 20% of livePALM-identified molecules to be false positive molecules, whereas only 1% of a-livePALM-identified molecules were false positive. There were 26% more total molecules detected by a-livePALM even with stringent thresholding conditions. These results underscore the importance of properly identifying molecules from the raw images in the first place and not to rely on post-filtering.

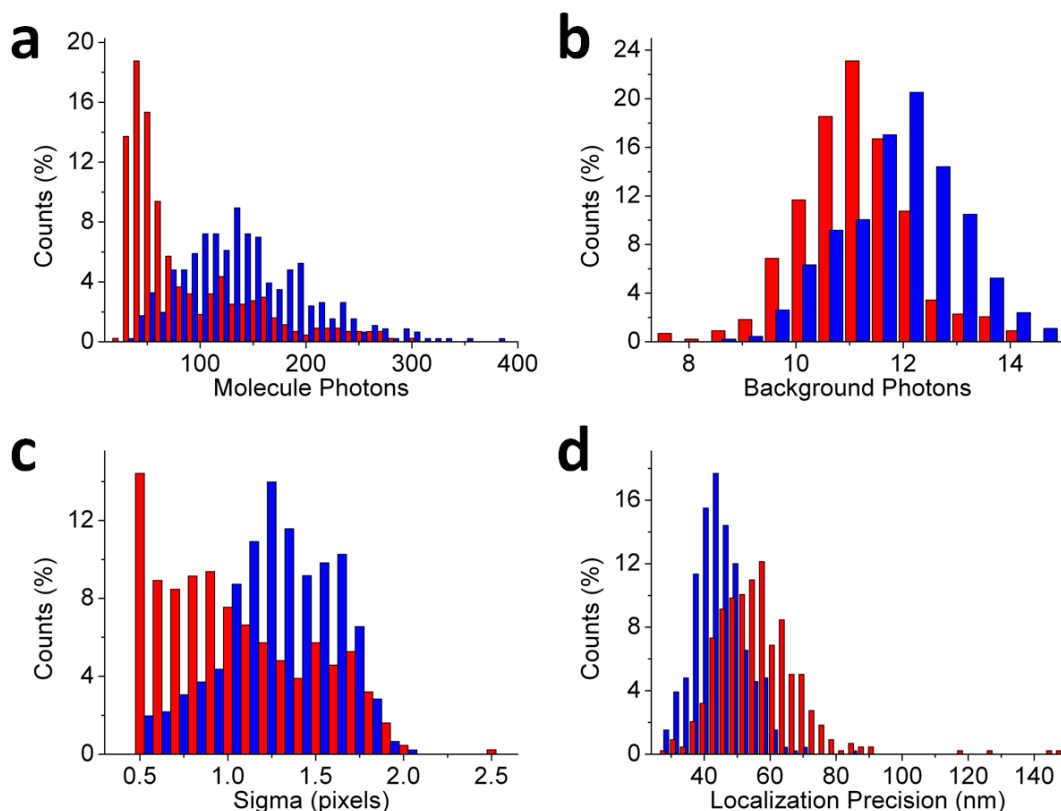


Figure 2.19 Histograms of parameter distributions of false positive and true positive molecules found in simulated data with livePALM. Simulated images were generated with 150 photons for each molecule, background, $N_{bg} = 12$ photons and $\delta = 1$ photon standard deviation of Gaussian noise. The distributions of returned fit parameters for (a) the number of photons per molecule, (b) background photons, (c) width of the point spread function, σ , and (d) localization precision are shown. Red and blue bars represent false positive and true positive molecules, respectively⁹¹. Reproduced with permission from the American Chemical Society.

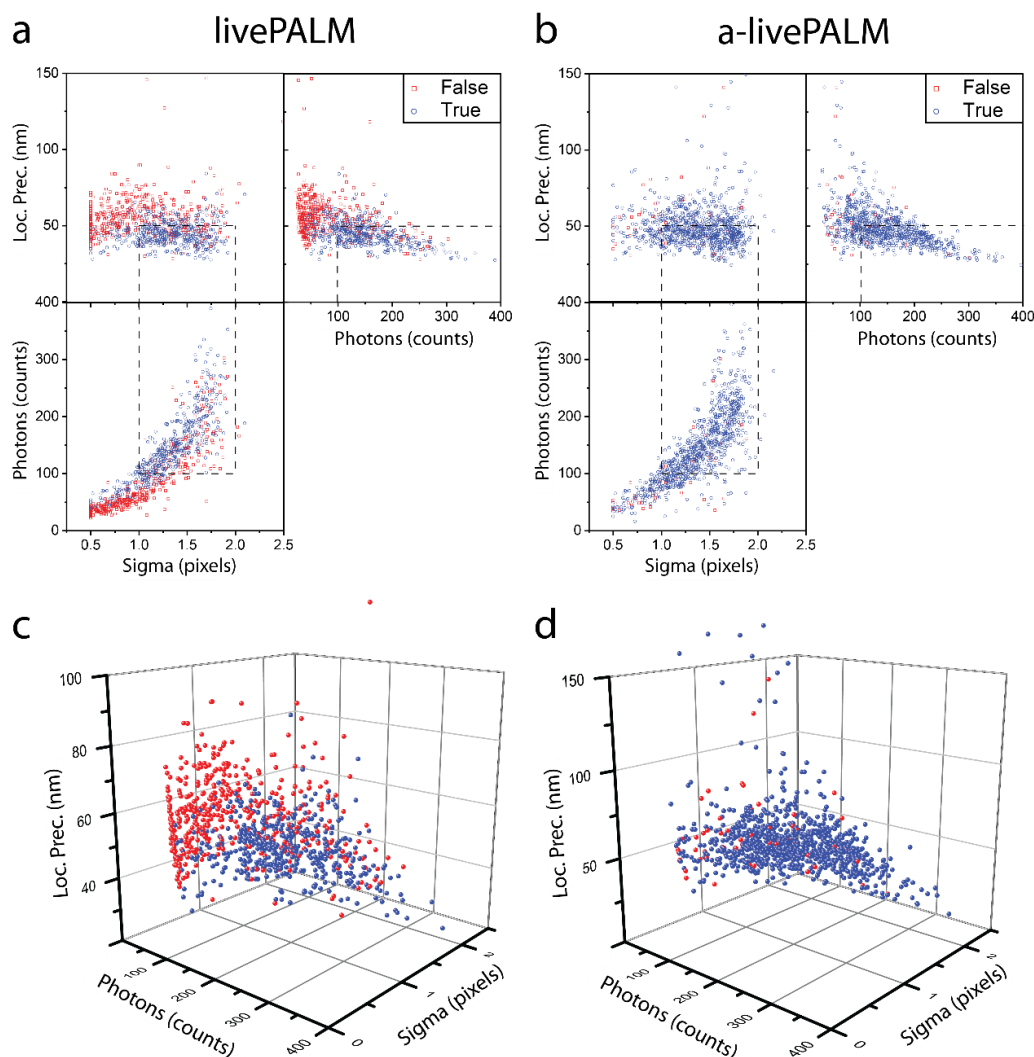


Figure 2.20 2D/3D plots of fitted parameters (photons, localization precision and σ) from livePALM (RO) and a-livePALM on simulated data (**Figure 2.13**). 2D plots of fitted parameters of livePALM and a-livePALM are shown in (a) and (b). We filtered the data with 100 – 500 photons, <50 nm localization precision and 1 – 2 pixels σ (shown by dotted lines). (c) and (d) are the corresponding 3D plots of (a) and (b). Red and blue dots represent false positive and true positive molecules, respectively⁹¹. Reproduced with permission from the American Chemical Society.

Table 2. 1 Summary of the post-filtered data

		Total	Photons 100-500	σ 1-2	Localization < 50 nm
livePALM	TRUE	458	354	345	282
	FALSE	437	129	126	69
	% FALSE	49%	27%	27%	20%
a-livePALM	TRUE	852	630	620	438
	FALSE	56	22	22	4
	% FALSE	6%	3%	3%	1%

2.7.2.5 Speed Comparison

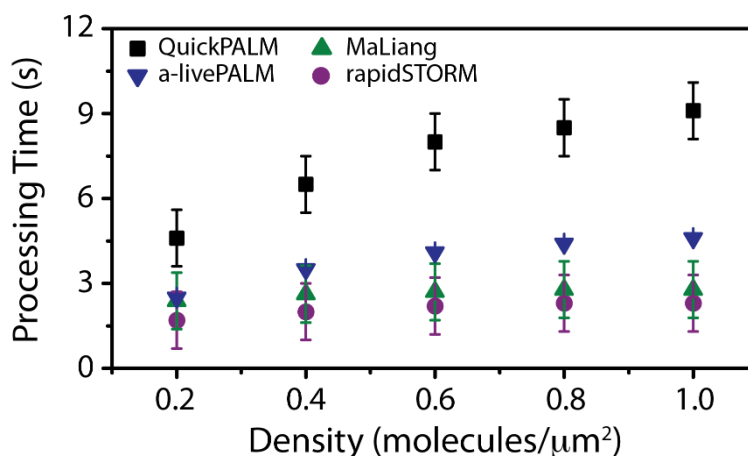


Figure 2.21 Processing time comparison⁹¹. Reproduced with permission from the American Chemical Society.

The image processing time of the a-livePALMa algorithm was compared against QuickPALM, MaLiang and rapidSTORM (**Figure 2.21**). The same sets of simulated images used for the recall and the precision performance tests were used. The processing times for QuickPALM, MaLiang and rapidSTORM were manually measured by using a stopwatch and were given an error of 1 s for the human response time variation. The error for a-livePALM was calculated from the reported processing time from MATLAB. As a result, our software can achieve a processing speed that is comparable to state-of-the-art fast software even with the additional background estimation.

2.7.2.6 Performance on Experimental Data

Finally, the software was applied to experimental data. A RITA-mcavRFP fusion construct was transiently transfected into HeLa cells. RITA is a tubulin binding protein, and was fused with the green-to-red photoconvertible fluorescent protein, mcavRFP¹²¹. PALM image acquisition was performed at 24 °C on a modified inverted microscope (Axiovert 200, Zeiss, Jena, Germany) equipped with a high NA oil immersion objective (Plapon 60x, 1.45- NA oil immersion, Olympus, Hamburg, Germany). The fluorescent proteins were converted from their green to their red emitting forms using 405-nm light of low intensity (0 – 10 W/cm²) and subsequently imaged by 561-nm illumination (200 – 400 W/cm²) with an EMCCD camera (iXon DV887ECS-BV, Andor, Belfast, Northern Ireland) at 100 ms time resolution. The overall fluorescence intensity varied in time due to power adjustment of the 405-nm laser and photobleaching of molecules (**Figure 2.22**). The raw wide field image also showed considerable SNR heterogeneity within the image (**Figure 2.23**).

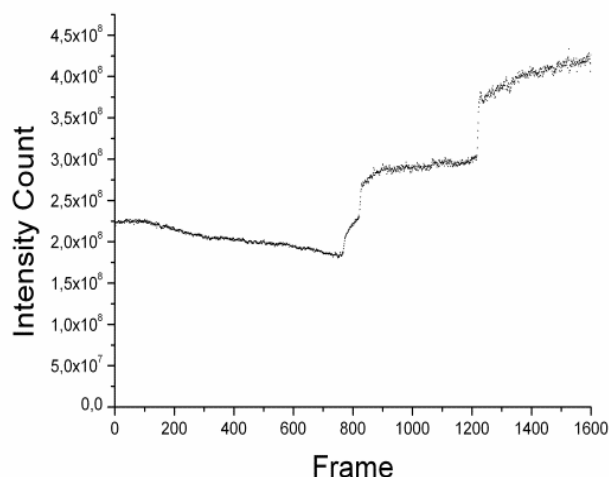


Figure 2.22 Intensity variation during PALM image acquisition. The overall fluorescence intensity was observed to change with time due to power adjustment of the 405-nm laser during the measurement as well as photobleaching of fluorescent molecules⁹¹. Reproduced with permission from the American Chemical Society.

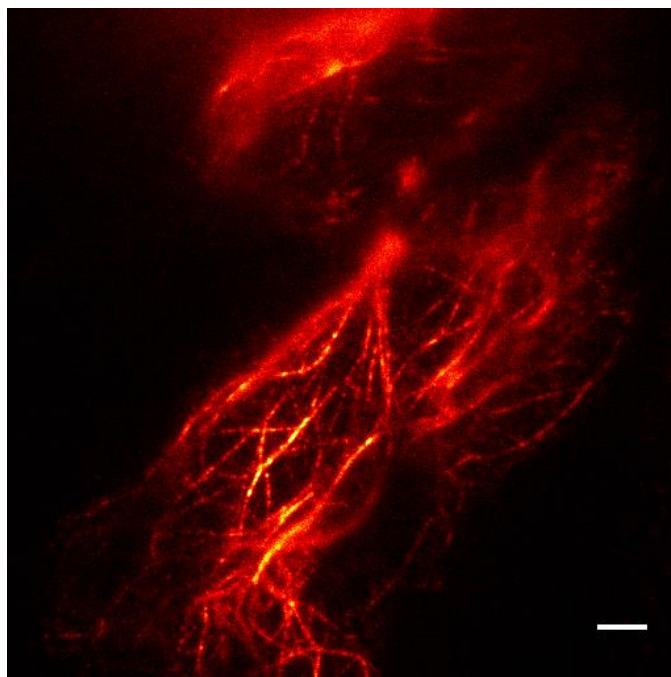


Figure 2.23 Widefield image of RITA-mcavRFP labeled microtubules in a live HeLa cell. Scale bar: 5 μm ⁹¹. Reproduced with permission from the American Chemical Society.

Comparison of the two algorithms on the experimental data further highlighted the strengths of the new software, a-livePALM. **Figure 2.24** shows PALM images reconstructed from 1,600 frames of raw data of the fusion protein RITA-mcavRFP in live HeLa cells analyzed by livePALM RO and a-livePALM. We could observe a

significantly higher molecule detection efficiency using the new algorithm, in agreement with the findings on simulated data. A total of 273,751 and 474,385 molecules were identified by livePALM RO and a-livePALM, respectively (**Figure 2.24e**). livePALM PO detected even less molecules: 98,013. We plotted these molecules with the same brightness and contrast setting for a direct comparison (**Figure 2.24a-d**). In regions with high SNR, livePALM performed equally well as a-livePALM. In regions with lower SNR, livePALM performed poorly, as we already saw with simulated images (**Figure 2.18**). As a result, some structures were missing from the image (indicated by arrows). In particular, for livePALM, the microtubules located in the upper third of the reconstructed image were missing due to high background (**Figure 2.23**).

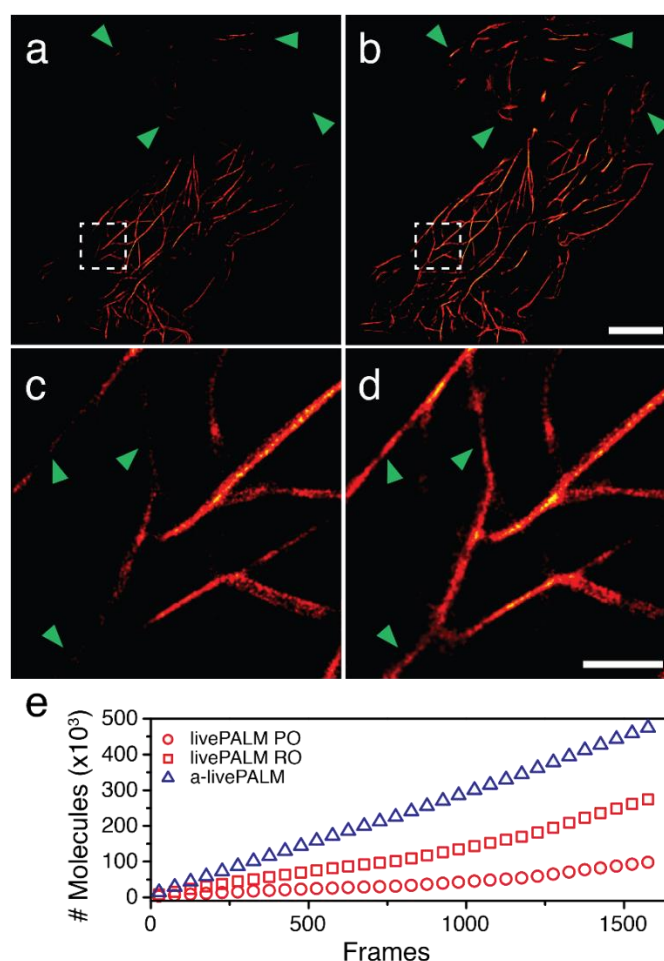


Figure 2.24 Performance of livePALM and a-livePALM molecule detection algorithms applied to experimental data. PALM images of microtubules in live HeLa cells, labeled with the fusion protein RITA-mcavRFP, were reconstructed by using the livePALM RO (a, c) and a-livePALM (b,d) algorithms. Arrows indicate structures reconstructed by a-livePALM, but missed by livePALM. Scale bar 5 μm (a, b) and 1 μm (c, d). (e) Accumulated number of molecules identified by the livePALM PO, livePALM RO and a-livePALM search algorithms during processing of 1,600 image frames⁹¹. Reproduced with permission from the American Chemical Society.

2.8 ISBI Localization Microscopy Challenge

In 2013, the IEEE International Symposium on Biomedical Imaging (ISBI) conference organized the localization microscopy challenge. The challenge has also been turned into a permanent online challenge (<http://bigwww.epfl.ch/smlm/challenge2013/>). About 30 programs from groups all over the world have been examined, mostly by the authors of the software. The a-livePALM software has been one of the earliest participant programs in 2013.

The goal of the challenge is to have a better view and understanding of available algorithms. This is achieved by benchmarking them using the same set to data. The general framework of dataset simulation and software assessment is shown in **Figure 2.25**. Synthetic datasets with ground truth (*i.e.*, images with known molecule localizations) that contain biologically-inspired structures, such as tubulins were generated. A continuous-spatial structure and associated fluorophore markers with random positions on its surface was defined. Then, sparse activation-excitation cycles at each time instant were simulated. Once excited, a single fluorophore was imaged by a realistic PSF while taking the average nature of the EMCCD detector into account. The noise sources included were non-homogenous excitation intensity over the field of view, background scatter noise, auto-fluorescence, EMCCD multiplicative noise, read-out noise and dark pixels. The challenge datasets were categorized into two groups: low density data and high density data, and it provided training datasets and tests datasets for each category. The same dataset was then evaluated by different analysis software. The main criteria for assessing the performance include detection rate, localization accuracy, computation time, usability, and accessibility for the end-user.

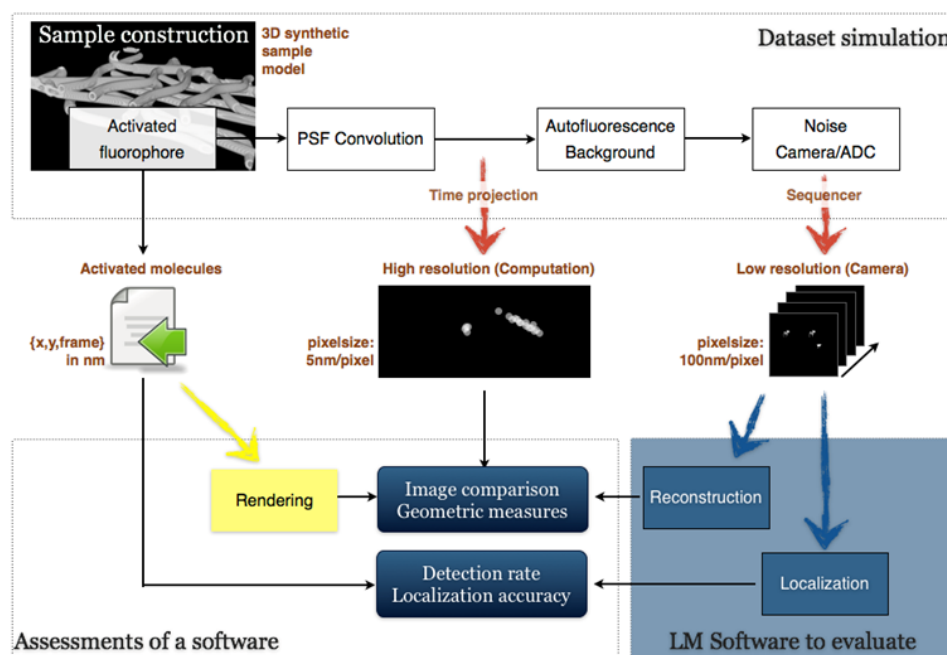


Figure 2.25 General framework of data simulation and software evaluation. Image adopted from Ref. [122].

In this challenge, we evaluated our software using the low density dataset. There are three different datasets in this category which have different SNR for each set of data. For simplification, we used the mean value of F and the mean computational time for these three datasets for comparison (**Figure 2.26** and **Figure 2.27**). Programs without any value (**Figure 2.26**) did not submit full results or only evaluated the high density dataset.

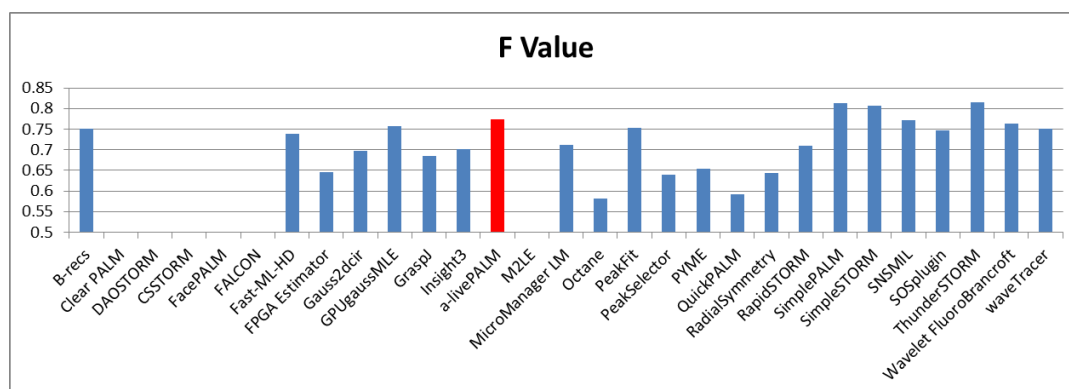


Figure 2.26 F value performance of 29 analysis programs from different groups worldwide.

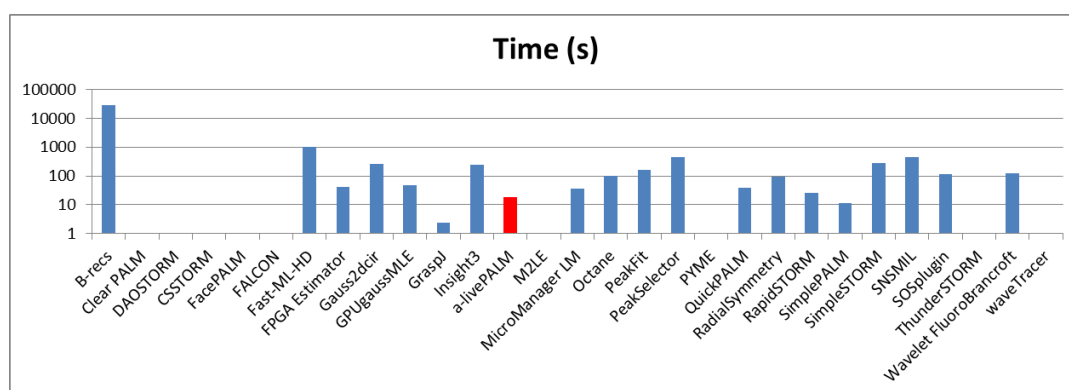


Figure 2.27 Computational time of 29 analysis programs from different groups worldwide.

In a recent publication, a revised comprehensive evaluation of localization software packages was published¹²². The number of the overall software packages evaluated had increased and the performance of some old programs had also improved compared to the initial report from 2013. In the latest paper, a number of criteria were employed to evaluate the output results from different programs: detection rate, accuracy, quality of image reconstruction, resolution, software usability and computational resources. The cumulative grades from these six aspects for the low density data sets were shown in **Figure 2.28**. Higher cumulative grade shows better performance. Various tradeoff of the analysis software packages were shown by these metrics (*i.e.*, accuracy and detection rate tend to change in an anti-correlated manner). Therefore, It could help users to choose the program which fit their needs best.

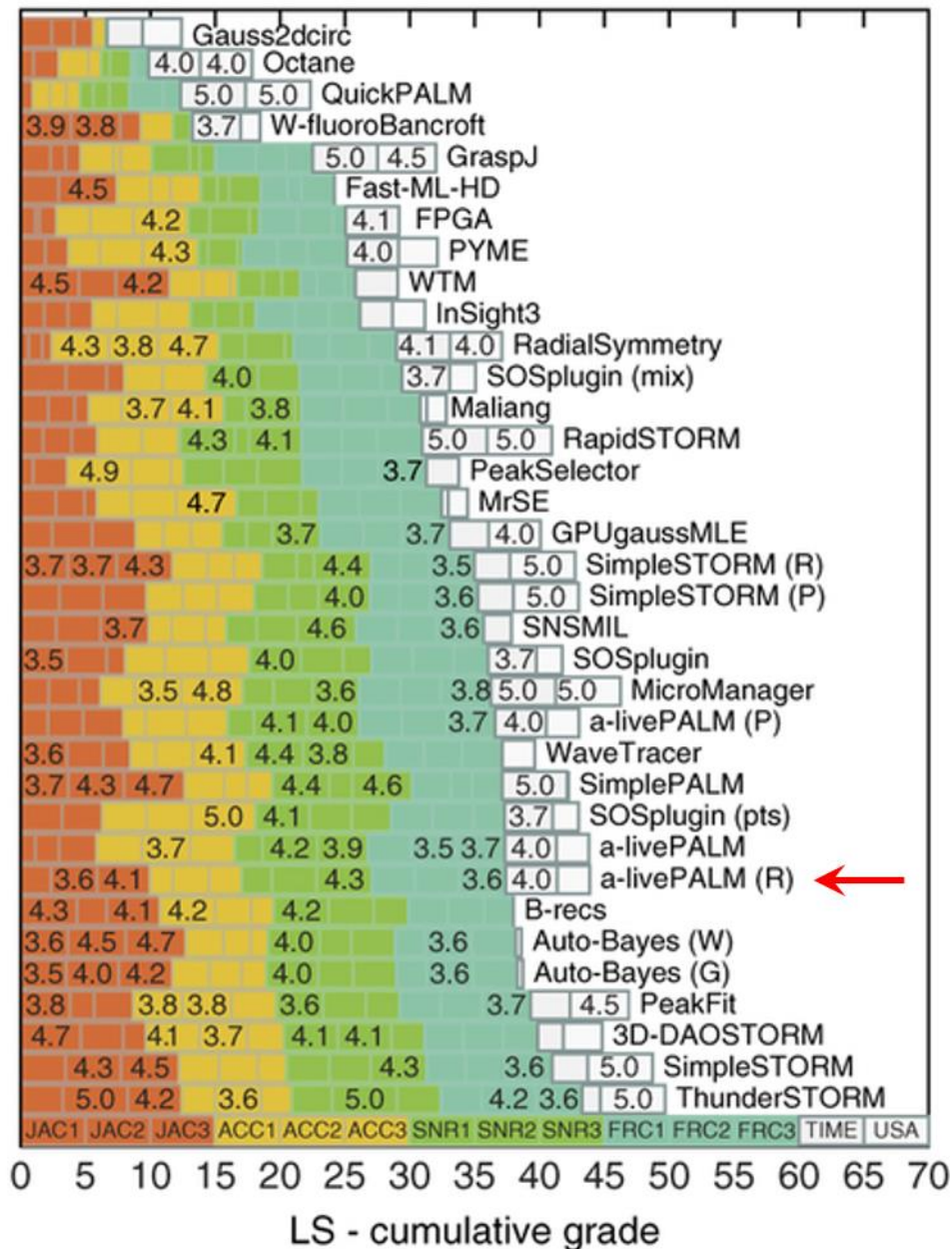


Figure 2.28 Cumulative grades for the three synthetic low density data sets. The grades of the three data sets were measured by the detection rate (Jaccard index), JAC1 – JAC3; localization accuracy, ACC1 – ACC3; image quality assessment, SNR1 – SNR3; and image resolution, FRC1 – FRC3. The subjective parameters of computational time (TIME) and usability (USA) are shown in light gray bars. The Red arrow indicates the rank of a-livePALM.

Chapter 3

Experimental Setup for 3D Localization Microscopy

In this chapter, we will introduce the microscope used for the experiments. Based on this apparatus, we have built a 3D-astigmatism super-resolution imaging setup for localization microscopy.

3.1 The TIRF Microscope

Total internal reflection fluorescence microscopy (TIRFM) is the most used microscope configuration for single molecule super-resolution imaging since it can offer a very good SNR of single molecule fluorescence. It exploits the physical phenomenon of total internal reflection, which appears when light propagating within a dense medium reaches an interface with a less dense medium at large incident angles. According to Snell's law, the critical angle, θ_{crit} , is given by

$$\sin\theta_{crit} = \frac{n_2}{n_1}, \quad (3.1)$$

where n_1 is the refractive index of the microscope slide or coverslip (*i.e.*, glass slide, $n = 1.518$). n_2 is the refractive index of the sample medium (*i.e.*, aqueous medium, $n = 1.33 - 1.37$). Total internal reflection is achieved at all angles greater than θ_{crit} , where all the light is reflected. Even though the light no longer propagates into the sample medium, the reflected light generates a highly restricted electromagnetic field adjacent to the interface in the lower-index medium. This field is parallel to the surface and termed evanescent field. It only extends a few hundred nanometers into the specimen in axial direction and decays exponentially in intensity with the distance, d , from the interface,

$$I(z) = I_0 \exp(-z/d), \quad (3.2)$$

where $I(z)$ is the intensity at the distance z perpendicular from the interface, and I_0 is the intensity at the interface. d defines the penetration depth and is dependent on the wavelength of the incident light, λ , the angle of incidence, θ , and the refractive indices of the interface, n_1 , and the medium, n_2 , according to:

$$d = \frac{4\pi n_2 \sqrt{n_1^2 \sin^2 \theta - n_2^2}}{\lambda} \quad (3.3)$$

The penetration depth usually ranges from 30 – 300 nanometers. Thus, only fluorophores within this region are excited.

Generally, there are two types of TIRF microscopes: (1) Prism-based TIRF, and (2) Objective-based TIRF as shown in **Figure 3.1a** and **b**. The prism TIRFM is easily accomplished since it requires only an additional prism compared to the normal microscope equipped with an objective lens. However, the drawback is that the sample is placed between the prism and the microscope objective. The fluorescence emitted from the top surface of the sample has to go through the sample before being collected by the objective which leads to wavefront aberrations. Also, sample handling is more difficult in prism-based TIRF since the position of the prism has to be adjusted each time after changing the sample. The more frequently used objective-type TIRFM greatly benefits from an objective with a high numerical aperture ($NA > 1.4$). Due to the high NA of the objective, the incident angle of the excitation laser can be larger than the critical angle when the light is directed into the objective off center. The fluorescence excited by this configuration can directly be collected by the objective.

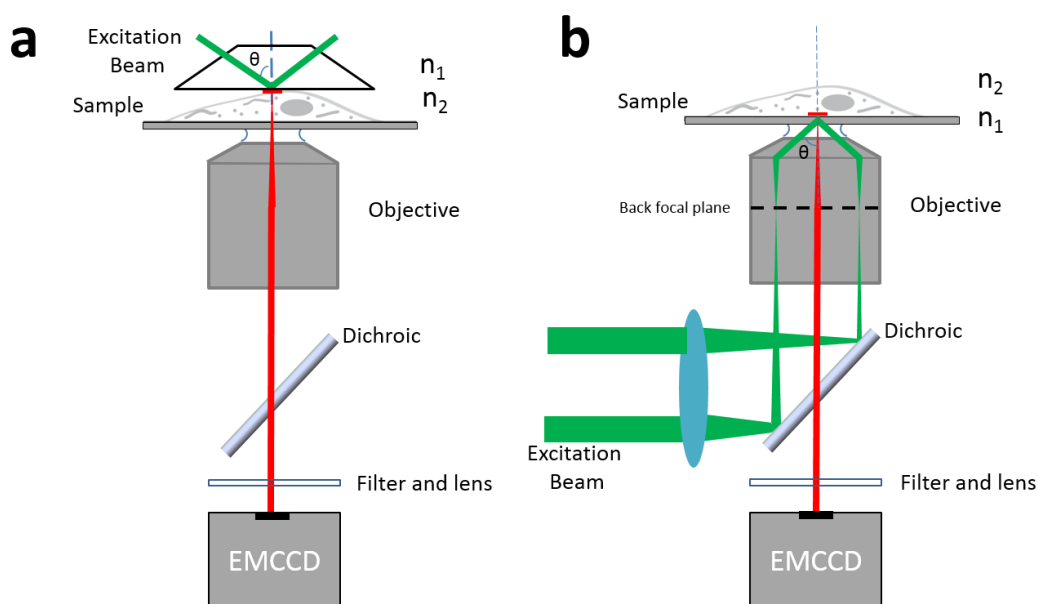


Figure 3.1 Two types of TIRFM configuration. (a) Prism-based TIRFM. (b) Objective-based TIRFM. In a prism-based TIRFM, the excitation and emission paths are decoupled. The sample is placed between prism and objective. In an objective-based TIRFM, the specimen is excited and the fluorescence is collected *via* the same objective lens.

3.2 Experimental Setup

A custom-built TIRF/epi fluorescence microscope was used. It was based on a modified inverted Zeiss Axio ObserverZ1 microscope equipped with a high NA oil immersion objective (Zeiss alpha Plan-Apochromat 63x/1.46 Oil). Four diode-pumped solid-state lasers with wavelengths 640 nm (OXX-LBX, Laser 2000, Wessling, Germany), 561 nm (GCL-150-561, CrystaLaser, Reno, USA), 473 nm (LSR473-200-T00, Laserlight, Berlin, Germany) and 405 nm (CLASII 405-50, Blue Sky Research, Milpitas, USA) were employed for excitation and photoactivation of the fluorophores. The laser sources were combined *via* appropriate dichroic mirrors (AHF, Tübingen, Germany) and guided through an AOTF (AOTFnC-400.650, A-A, Opto-Electronic, Orsay Cedex, France) to control the laser intensity at the sample. After passing the AOTF, the laser beam was expanded (3.75 \times) by a telescope (L1 and L2 in **Figure 3.2**). If a smaller EMCCD camera (iXon 860, 128 \times 128 pixels, field of view 15 \times 15 μm^2 , Andor, Belfast, UK) was used, the telescope was removed from the excitation path. Lens L3 focused the parallel beam into the back focal plane of the objective lens, providing wide field illumination of the sample. By tilting the mirror M1, TIRF or highly inclined and thin beam (highly inclined and laminated optical sheet, HILO)¹²³ excitation could be achieved. The emission fluorescence was first collected by the same objective lens. After passing a quad band dichroic mirror (HC Quadband Emitter 446/523/600/677, AHF), an additional filter could be added (F1) before imaging through the tube lens L4. The fluorescence was either guided to an iXon DV 897 or an iXon 860 EMCCD camera. In the iXon DV 897 path, a commercial beam splitting device (OptoSplit II unit, Cairn Research, Kent, UK) was used. The fluorescence was split into two color channels by a 640 nm short pass dichroic or a 555 nm long pass dichroic mirror depending on the application. Additional filters could also be used in each channel (HC 525/50 for green channel, center wavelength 525 nm with a FWHM 50 nm; HC610/75 for red channel; HC697/75 for far red channel; HC 523/610 for both green and red channel; all of the filters are from AHF). The image was magnified two-fold by a set of relay lenses in this device so that the final pixel size was 110 nm. Alternatively, the fluorescence was directed to the iXon 860 EMCCD by a flip mirror. In this optical path, the image formed by tube lens L4 was additionally magnified (2 \times) by a single lens L5. A cylindrical lens L6 (LJ1516L1-A, $f = 100$ cm, Thorlabs, New Jersey) was added before the camera to modify the PSF enabling 3D astigmatism super-resolution imaging.

The signals to control all shutters and the AOTF were generated by a data acquisition card (NI USB-6229 BNC, National Instruments, Austin, USA) and controlled by a custom written software in LabVIEW (National Instruments). To avoid photobleaching between camera frames, the camera fire pulse was connected to the AOTF blanking pin. Image acquisition was done by the Solis software provided by the camera manufacturer (Andor Technologies). An incubator (XL-5 DARK, Pecon, Erbach, Germany) covering the microscope stage was used to control the sample temperature.

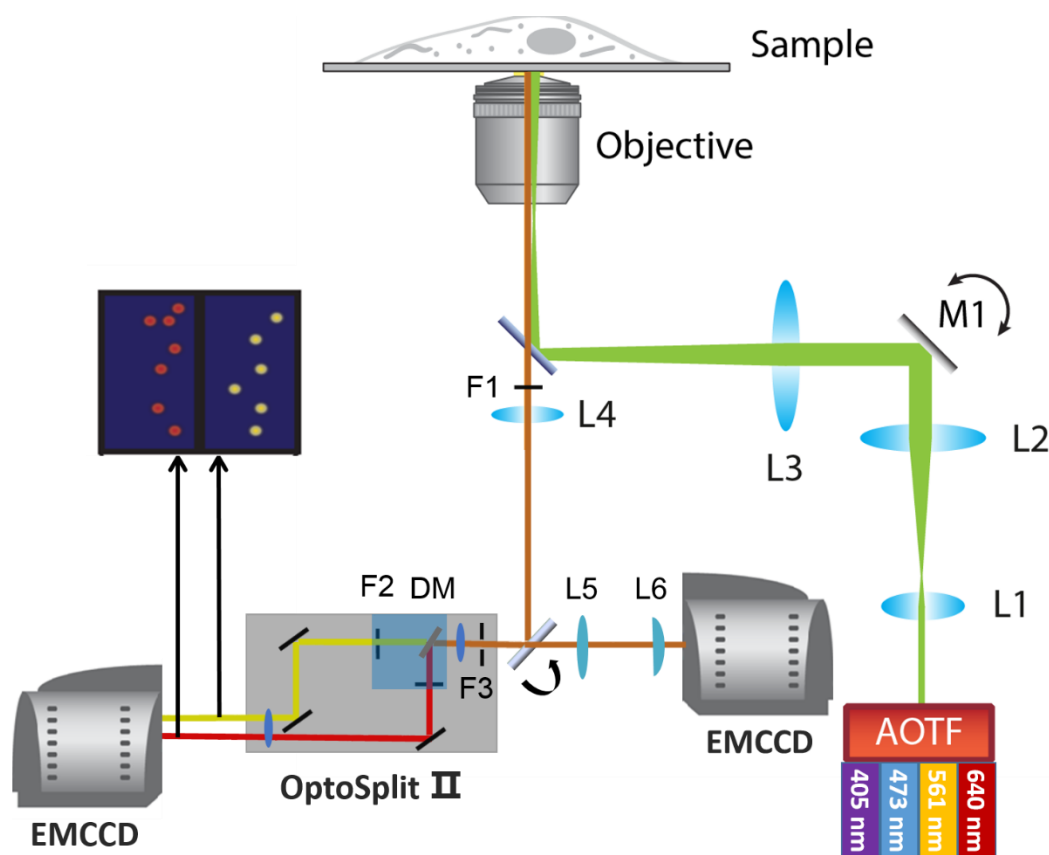


Figure 3.2 Schematic of the microscope setup. Laser light from four lasers is combined and guided through an AOTF. A telescope (lenses L1 and L2) is added in the excitation beam path to change the size of the illuminated area in the sample. The emitted fluorescence is collected by the objective and passes filter F1. After traversing a tube lens L4, the fluorescence is collected either by the iXon897 or the iXon860 EMCCD depending on the application.

3.3 3D Super-resolution Imaging

Various strategies have been proposed to localize fluorescent molecules in three dimensions in 3D super resolution imaging. All the methods are based on engineering the shape of a molecule's PSF as a function of its distance from the focal plane. These methods include simultaneous imaging at two different focal planes¹²⁴ and altering the PSF so that its shape encodes the axial position. For instance, with a spatial light modulator in the imaging path¹²⁵, a double-helix PSF can be produced.

3.3.1 3D Astigmatism Super-resolution Imaging

We have used an approach that introduces astigmatism to the PSF by adding a weak cylindrical lens to the imaging path^{126–128}. The scheme of this method can be seen in **Figure 3.3**. The weak cylindrical lens creates two slightly different focal planes for the x and y directions. Therefore, the ellipticity of the PSF varies as the position changes in

z . If the fluorophore is in the averaged plane of the x and y focal planes, the PSF shows equal widths in the x and y directions (round). When the fluorophore is moved out of the averaged focal plane, the image will be more focused in either x or y direction and thus appears ellipsoidal with a long x axis or y axis. By determining the width of the PSF along the x and the y directions, we can estimate the z coordinate of the fluorophore with very high precision. This astigmatic approach requires only minimal changes of both the optical setup and the analysis software. Thus it is the most frequently used approach in the field.

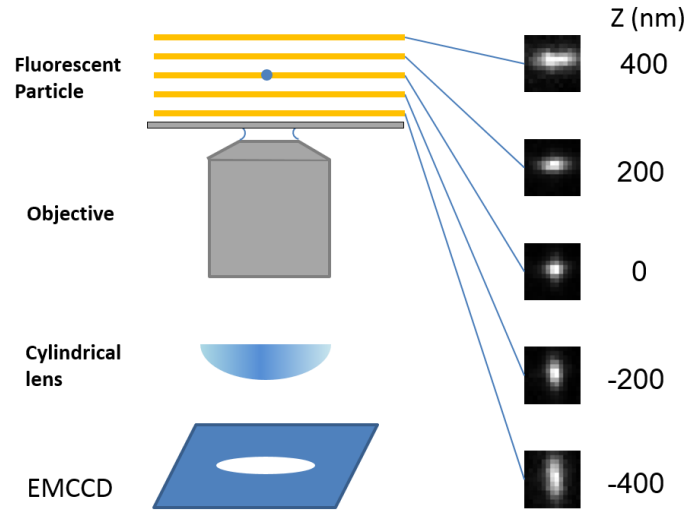


Figure 3.3 The scheme of 3D PALM. After introducing a cylindrical lens in front of the camera, a fluorescent particle shows different ellipticity in the imaging plane at different z coordinates (right panels). By measuring the ellipticity of the PSF, we can determine the z coordinate of the fluorescent object.

The PSF modified by a cylindrical lens can be modeled as an elliptical Gaussian function,

$$PSF(x, y) = \frac{1}{2\pi\sigma_x\sigma_y} \exp\left(-\frac{x^2}{2\sigma_x^2} - \frac{y^2}{2\sigma_y^2}\right), \quad (x, y) \in \mathbb{R}^2, \quad (3.4)$$

where σ_x and σ_y are the widths of the PSF in the x and y directions, respectively. The combination of σ_x and σ_y encodes the axial position z . A calibration is necessary to derive the z coordinates.

To experimentally generate a calibration curve showing σ_x and σ_y as a function of z , dye molecules or small fluorescent beads are attached to the coverslip and imaged at different z positions. Here, a bead sample was prepared by adsorbing a dilute solution of ~ 100 nm Tetraspeck fluorescent beads (~ 0.3 pM, Invitrogen, Grand Island, USA) on glass cover slips. The beads were imaged in deionized water. The bead density was chosen so that about 7 – 12 beads were visible in the field of view (128×128 pixels) when imaging. Images were recorded with an acquisition time of 50 ms at 50 nm axial

piezo steps over a z range of 1.2 μm (600 nm above and below the averaged focal plane) by moving the objective automatically using the piezo stage (PD72z1x PIFOC® lens scanning system, Physik Instrumente, Karlsruhe, Germany). 100 frames were taken for each step. Only the center 50 frames of each set were analyzed to exclude images recorded during movement of the objective between two positions.

For each z position, the σ_x and σ_y values were then fitted to a modified equation describing a typical defocusing curve:

$$\sigma_x = \sigma_{x0} \sqrt{1 + \left(\frac{z-r_x}{d_x}\right)^2 + A_x \left(\frac{z-r_x}{d_x}\right)^3 + B_x \left(\frac{z-r_x}{d_x}\right)^4}, \quad (3.5)$$

$$\sigma_y = \sigma_{y0} \sqrt{1 + \left(\frac{z-r_y}{d_y}\right)^2 + A_y \left(\frac{z-r_y}{d_y}\right)^3 + B_y \left(\frac{z-r_y}{d_y}\right)^4}, \quad (3.6)$$

where σ_{x0} and σ_{y0} are the widths of the PSF at the focal plane, r_x and r_y are the offsets of the x and y focal planes from the average focal plane. d_x and d_y indicate the focus depth of the microscope and were included as a fit parameter. A_x, A_y, B_x and B_y are coefficients of higher order terms to correct for the non-ideality of the imaging optics. The obtained calibration curves in $z - \sigma_x$ and $z - \sigma_y$ space and $\sigma_x - \sigma_y$ space are shown in **Figure 3.4** and **Figure 3.5**.

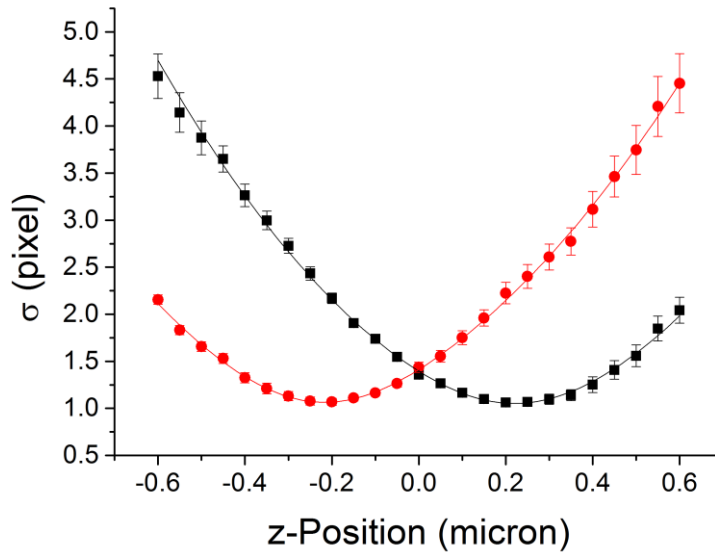


Figure 3.4 Calibration curve of the image widths σ_x and σ_y as a function of z , obtained from a single fluorescent bead. Each data point is the average value obtained from 7 beads. The data were fitted to the defocusing functions, Eqs. 3.5 and 3.6.

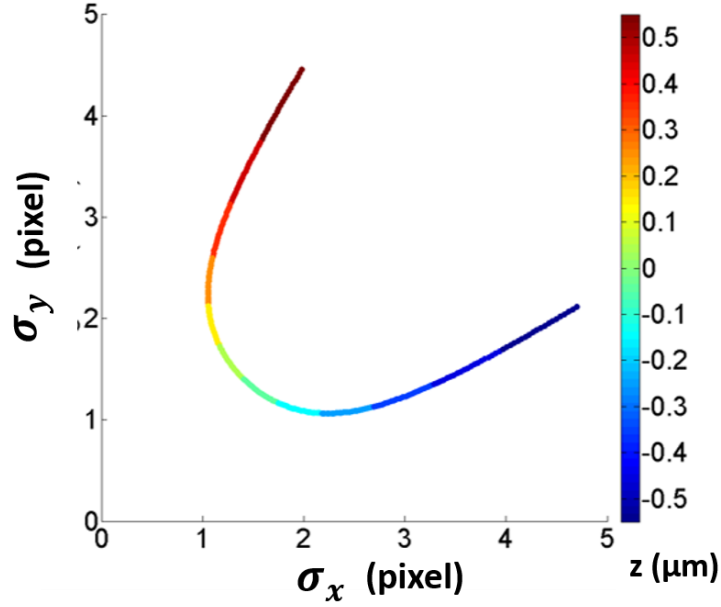


Figure 3.5 Calibration curve in σ_x - σ_y space. The color represents the z position.

In all actual experiments, the σ_x and σ_y values were determined for each molecule. These parameters were used to find the axial position of the molecule that best matched the calibration curve. This was done by minimizing the distance in the $\sigma_x^{1/2} - \sigma_y^{1/2}$ space:

$$D = \sqrt{(\sigma_x^{1/2} - \sigma_{x,cali}^{1/2})^2 + (\sigma_y^{1/2} - \sigma_{y,cali}^{1/2})^2}. \quad (3.7)$$

To evaluate the range and accuracy of the z localization, the multicolor beads were imaged on the coverslip while moving the piezo-driven sample stage. The stage was moved by 50 nm every 50 frames. Localization analysis of the astigmatic images reproduced the z -direction movement very accurately (**Figure 3.6**). The standard deviation of the z position near the focal plane (distance <200 nm) was $\sim 5 - 7$ nm, while the standard deviation of the z positions far away from the focal plane (400 – 600 nm) was $\sim 8 - 13$ nm.

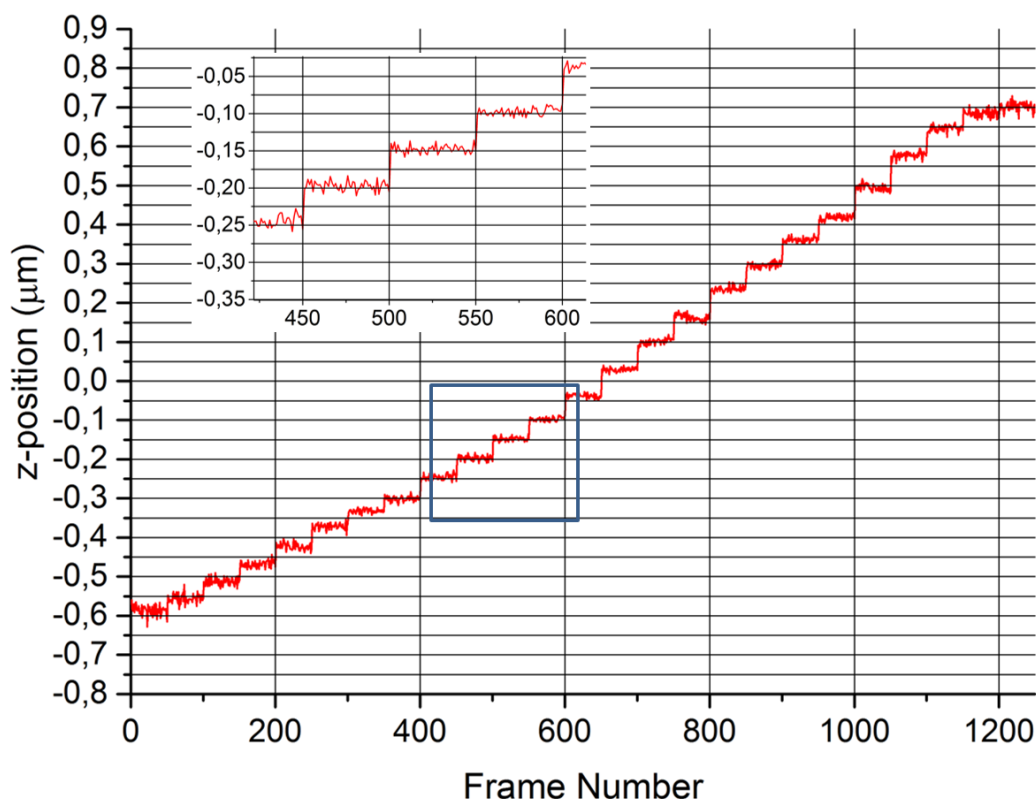


Figure 3.6 Axial localization of a 100 nm diameter fluorescent bead. A fluorescent bead was imaged on the coverslip with the piezo stage being axially translated by 50 nm every 50 frames. The axial position was then determined from the regular astigmatism 3D PSF calibration data. The figure shows the resulting returned axial positions. The determined positions are remarkably close to the piezo positions. The inset shows a close-up of the region marked by the blue box.

3.3.2 Experimental Note on Calibration Curve Generation

The shape of the elliptical PSF on the image plane is usually determined by the focal length of the cylindrical lens and the distance d between the cylindrical lens and the camera. The focal length of the cylindrical lens in front of the EMCCD camera (**Figure 3.2**) was 1 m. The value d will affect the σ_x and σ_y range that is covered before defocusing of the PSF occurs. If d is too small, σ_x and σ_y will not change much before defocusing. Small changes of the calibration curve while changing the axial position will result in a low axial resolution. If d is too large, the PSF will change too fast and defocus already at a short distance away from the averaged focal plane. Therefore, the cylindrical lens is placed in a position that maximizes the σ_x and σ_y range while keeping the PSF focused over a wide range. A typical range for σ_x and σ_y in our setup is from 100 to 600 nm, and the working distance before defocusing is ± 600 nm.

Asymmetry of the σ_x and σ_y curves was observed rather often (**Figure 3.7**). This

may result in a relatively poor axial position on one side of the averaged focal plane. It is probably due to spherical aberrations which are introduced by the refractive index mismatch when imaging with an oil immersion objective into an aqueous sample¹²⁹. Adjusting the objective correction collar (**Figure 3.8**) could compensate for this error. The correction collar is supposed to correct for aberration artifacts caused by the thickness of the glass slide. To demonstrate the effect of the different collar positions on the PSF shape at different axial positions, we adjusted the collar to 3 different correction collar positions and recorded the PSF while changing the objective's axial position (**Figure 3.9**). **Figure 3.9a** shows the PSF when the red mark on the collar was at the smallest value (0.14, **Figure 3.8**). The PSF shows a ring structure at -300 nm and below which cannot be fitted well by the elliptical Gaussian function. The PSF above the focal plane defocused and faded very fast, resulting in a smaller σ_y above the focal plane. **Figure 3.9b** shows the PSF when the red mark of the collar was set to ~ 0.18 . At this collar position, the PSF shape did not diverge in a relatively long range both below and above the focal plane (from -600 nm to 600 nm). The PSF could be well fitted by the elliptical Gaussian function and returned a symmetric calibration curve as shown in **Figure 3.4**. **Figure 3.9c** shows the PSF when the red mark of the collar was at the largest value (0.19, **Figure 3.8**). The PSF behaved opposite to **Figure 3.9a**. The PSF appeared as a ring shape at 300 nm and above and faded fast below the focus plane. The returned σ_x was relatively small below the focal plane in this case.

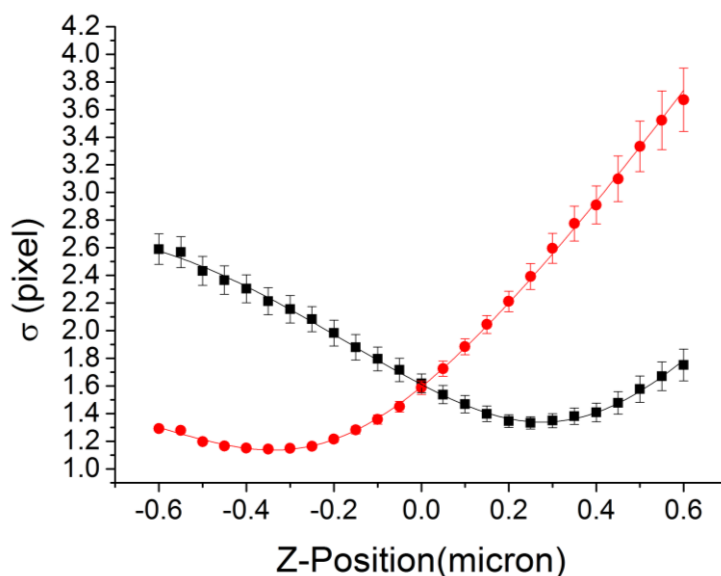


Figure 3.7 Asymmetric calibration curve of the PSF widths σ_x and σ_y as a function of z obtained from single fluorescent beads. Each data point is the average value obtained from 5 beads.



Figure 3.8 Alpha Plan-Apochromat 63×/1.46 Oil Corr M27. Image adopted from Ref. [130].

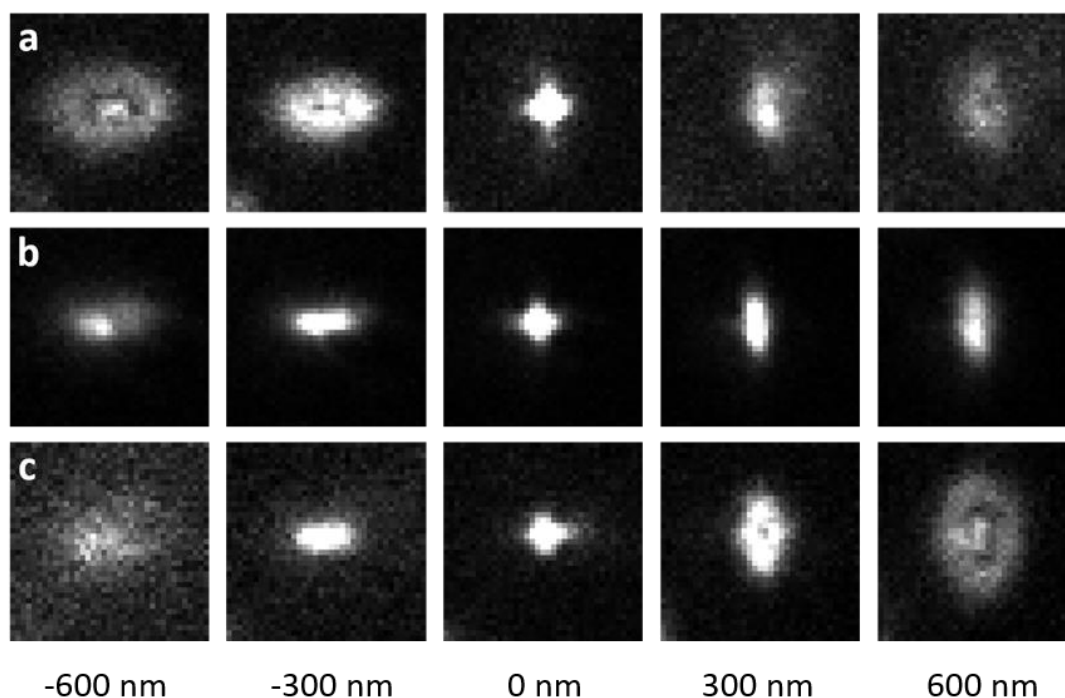


Figure 3.9 The PSF shape changes with different collar settings (red mark). (a) Collar value 0.14. (b) Collar value 0.18. (c) Collar value 0.19. From left to right, the objective was moved from -600 nm to 600 nm, with the focal plane at 0 nm.

Besides the width of the PSF, the lateral positions of the PSF upon changing the z position also need to be considered. Since most microscope applications are only interested in images at the focal plane, it is often overlooked how the PSF drifts out of focus. We realized that the lateral positions of the PSFs also shifted at different axial positions as shown in **Figure 3.10a** and **c**. The standard deviation of the x and y positions was 66 nm and 11 nm when moving the objective from 600 nm below the objective to 600 nm above the focus plane, respectively. The x position changed

linearly from ~ -125 nm to ~ 100 nm. The variation was much larger than the localization precision. **Figure 3.10b** and d shows the lateral positions at different axial positions after the objective was corrected by the vendor. The standard deviations for the x and y directions were comparable: 16 nm and 11 nm, respectively. The shift in x direction had improved dramatically.

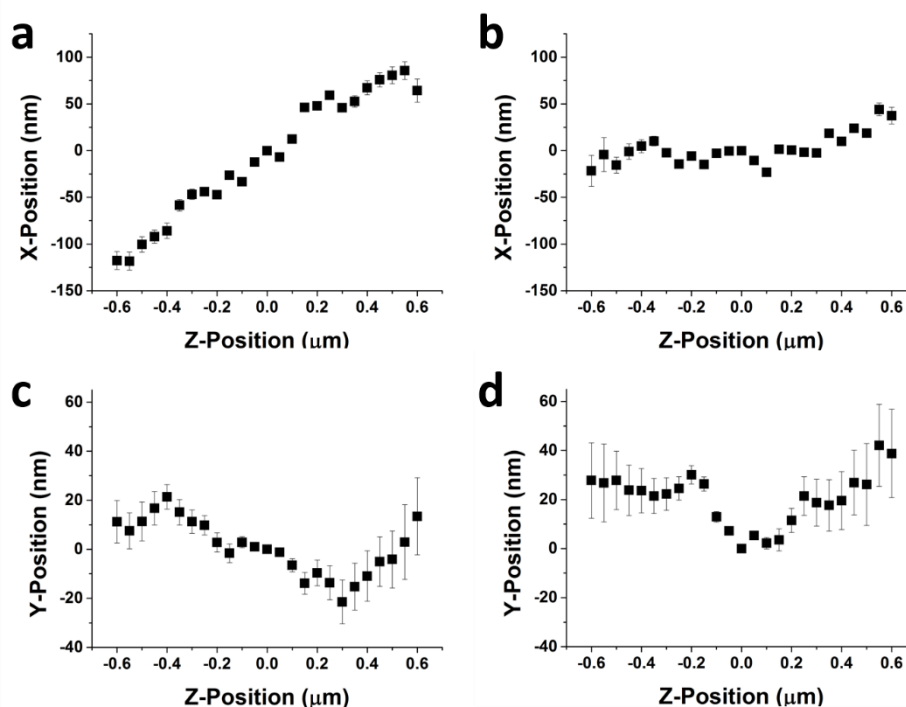


Figure 3.10 Lateral shift of PSFs when changing the axial position. (a) and (c) show the x and y positions as a function of z position before objective correction by the manufacturer. (b) and (d) are the x and y position as a function of z position after correction by the manufacturer.

After obtaining a suitable calibration curve, the final step of the 3D reconstruction of PALM images is to convert the σ_x and σ_y of the sample molecules into z positions. As described in Eq. 3. 8, this is done by minimizing the distance of the molecule's σ_x and σ_y to the calibration curve in the $\sigma_x^{1/2} - \sigma_y^{1/2}$ space. However, the σ_x and σ_y distributions were often quite broad in biological samples due to the fact that many background fluorophores were excited during 3D imaging (**Figure 3.11a**). To estimate how the algorithm assigns a molecule with σ_x and σ_y far off the calibration curve, 20,000 molecules were simulated with σ_x and σ_y evenly distributed in the range from 0.5 to 6 pixels. These molecules returned by the software were then plotted with color coding of the axial positions (**Figure 3.11b**). As we can see from **Figure 3.11b**, slight changes of σ in the region marked by the circle result in changes of the assigned z position of hundreds of nanometers. This makes the returned axial position distribution very broad, which will reduce the image quality. Therefore, the molecules

were often filtered based on the distance to the calibration curve before assigning z positions to them.

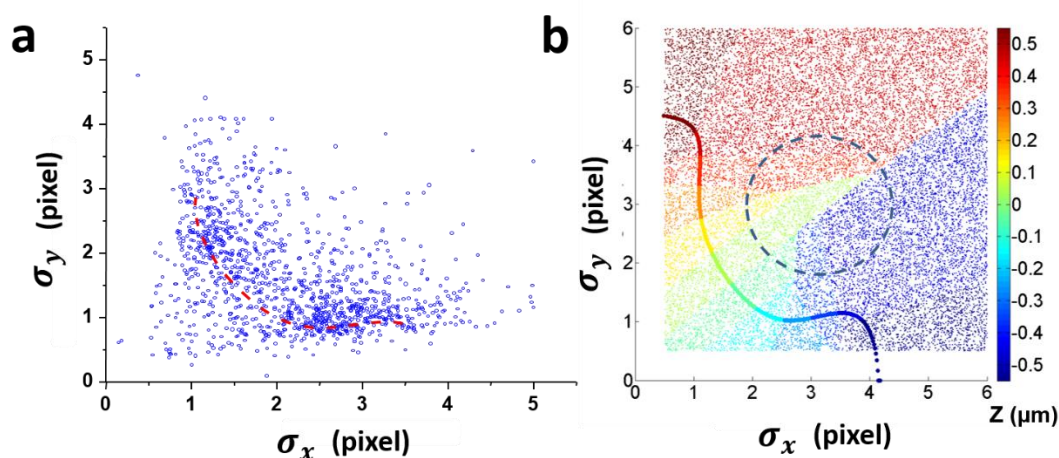


Figure 3.11 σ_x , σ_y and corresponding z position. (a) Scatter plot of the σ_x and σ_y from a typical biological sample. The dashed red line represents the calibration curve. (b) Simulated molecules and their corresponding z position encoded by color.

3.3.3 Dual Channel 3D Astigmatism Super-resolution Imaging

By inserting an additional cylindrical lens between F1 and objective lens (**Figure 3.2**), it is also possible to image the beads in two color channels with 3D super resolution. Due to the fact that the filter slot inside the microscope body is fixed, the position of the cylindrical lens could not be varied much. Therefore, the focal length of the cylindrical lens is important for the final shape of the PSF. A cylindrical lens with 10 m focal length (SCX cylindrical lens 10 m focal length, CVI Melles Griot, Rochester, USA) was used. Calibration curves of multi-color beads in the 582/50 nm channel and the 697/75 nm channel are shown in **Figure 3.12**.

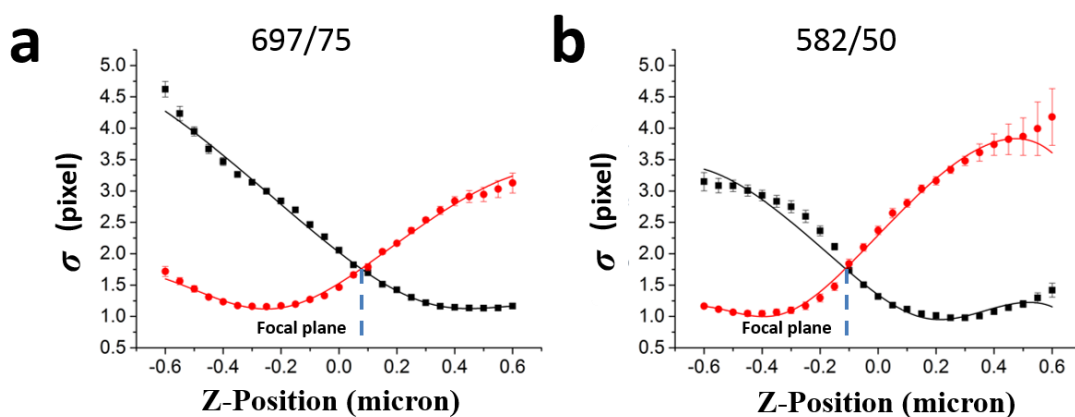


Figure 3.12 Calibration curves of the same multi-color beads in two channels: (a) far red (697/75) channel; (b) red channel (582/50).

By using the OptoSplit, the PSFs from the same beads could be displayed with astigmatism in both channels. It was possible to image in two color and with 3D super-resolution simultaneously using this setup. However, a focal shift of ~ 200 nm was observed between the two channels (**Figure 3.12**) because the focal length of the cylindrical lens changes as a function of the wavelength. Therefore, one should compensate this chromatic aberration in the final data when merging the two channels.

Chapter 4

Combination of Single Particle Tracking and Localization Microscopy

Since a PALM image is a sum up of all molecules acquired in many individual frames during data acquisition, the temporal resolution is limited by the number of frames needed to reconstruct the biological structure. A typical CME process happens on the time scale of tens of seconds²⁸, and it also typically takes ten of seconds to reconstruct a PALM image⁷³. Thus, the uptake process appears blurred in the final reconstructed PALM image. Although researchers have attempted to push the temporal resolution of localization microscopy to the sub-second range^{76,131}, such techniques are still limited by the brightness and fast blinking of the fluorophores due to the inherent requirement of collecting enough individual locations to reconstruct the structure. Therefore, we have combined localization microscopy with single particle tracking (SPT) to image the cellular uptake of NPs with both high temporal and spatial resolution.

4.1 Combination of PALM and SPT

SPT allows imaging single NPs with high temporal resolution. However, it only monitors individual particles with high precision and lacks the ability to provide structural information of the membrane receptors. Here, we have combined PALM and SPT to image the interactions between membrane carriers and single NPs, so that both high spatial and temporal resolution are achieved. A schematic view of this method is shown in **Figure 4.1**. NPs and CCPs were imaged simultaneously in two color channels using only one camera to speed up the measurement. The positions of the NPs in the individual frames recorded in the far red channel (697/70) were linked to create NP trajectories. In the red channel (582/50), a PALM image of the receptor was reconstructed. The trajectories and the PALM image were then overlaid with high precision. With the high temporal resolution of the trajectories and the high spatial resolution of the PALM image, mapping the interaction between NPs and membrane receptors with both high spatial and temporal resolution was possible.

Overlaying of fluorescence images in different channels is commonly used in cell biology. Since the resolution limit of conventional optical microscopy is on the order of ~250 nm, there has been no need for accurate image registration. However, with the advent of super-resolution techniques, the precision of the image overlay also needs to

be improved. In the following, we introduce an image registration method using fiducial beads to achieve a colocalization precision of at least 20 nm.

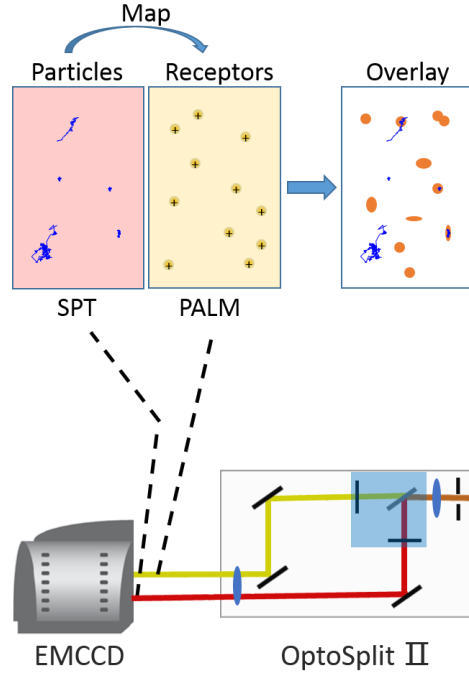


Figure 4.1 Schematic of the experimental set-up. The fluorescence emission from particles and membrane receptors was split into two channels and imaged simultaneously onto one camera. The SPT trajectories were obtained in the particle channel, while the PALM image was reconstructed in the receptor channel. By applying a locally weighted image registration procedure, the two images were overlaid with registration errors smaller than the localization precision.

A bead sample was prepared by adsorbing a dilute solution of ~ 100 nm Tetraspeck fluorescent beads (~ 0.3 pM, Invitrogen) on poly-L-lysine coated glass cover slips. The beads were imaged in deionized water. The bead density was chosen such that 50 – 80 beads (**Figure 4.2a**) were visible in the field of view when imaging. Images of different areas were acquired to randomly sample different parts of the field of view. For each image, pairs of locations which appeared in both channels were determined. These pairs of locations are called control points. A mapping function based on this set of control points was calculated and applied to any future data points. We have used a local weighted mean (LWM) mapping¹³²:

$$f(x, y) = \frac{\sum_i W_i(R) P_i(x, y)}{\sum_i W_i(R)}, \quad (4.1)$$

where the local weight $W_i(R)$ is defined as:

$$\begin{aligned} W_i(R) &= 1 - 3R^2 + 2R^3 & 0 \leq R \leq 1 \\ W_i(R) &= 0 & R > 1 \end{aligned} \quad (4.2)$$

and

$$R = \frac{[(x-x_i)^2 + (y-y_i)^2]^{1/2}}{R_n}. \quad (4.3)$$

R_n is the distance of position (x, y) to the n -th closest control point. $P_i(x, y)$ is the quadratic mapping function of control point i based on its n nearest control points. Here, we obtained the best results with $n = 400$.

To estimate the mapping error, the target registration error (TRE) was used. The TRE is calculated using the following function:

$$TRE = \left(\frac{1}{N} \sum_{i=1}^N [X_{i,1} - T_i\{X_{i,2}\}]^2 \right)^{1/2}, \quad (4.4)$$

where N is the number of control points, $X_{i,1}$ and $X_{i,2}$ are a pair of control points i in channel 1 and channel 2, respectively. T_i is the LWM mapping function from channel 2 to 1 without control point i .

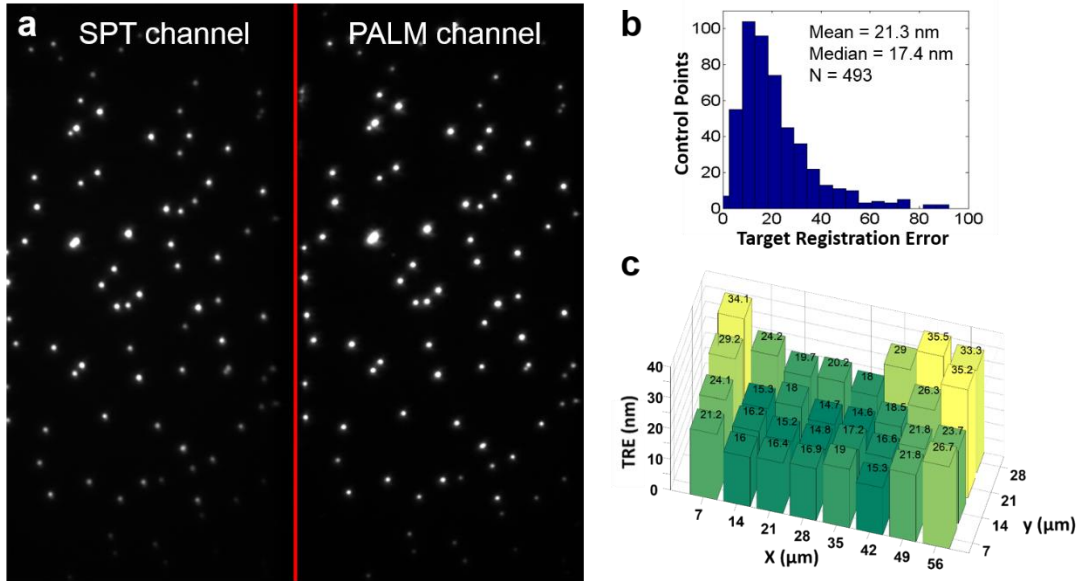


Figure 4.2 Accurate image registration using multicolor beads. (a) The bead density was chosen such that $\sim 50 - 80$ beads were visible in the field of view. (b) The target registration error (TRE) was computed for each control pair by iteratively removing a given control pair and computing the mapping function with the remaining control pairs. The mean TRE was 21 nm, the median TRE was 17 nm. The mapping function was calibrated before each experiment. (c) The distribution of mean TRE s for different sub-regions of the field of view. In the central area (~ 15 nm), the TRE is smaller than in the periphery (>30 nm), presumably due to spherical aberrations of the optical system.

As shown in **Figure 4.2b**, the mean *TRE* was 21 nm and the median *TRE* was 17 nm. The mapping function was determined before each experiment. The optical components except the filter block (F1, **Figure 3.2**) in the emission path were not touched after the calibration. The *TRE* was different in the different regions of the field of view, as shown in **Figure 4.2c**. In the central area, the *TRE* was ~ 15 nm while the *TRE* was >30 nm in the boundary area. This difference is probably due to spherical aberrations of the optical system, where the central part of the field of view is more linear than the boundaries.

4.2 Fluorophore Selection

Generally, there are two different approaches for multicolor imaging in localization microscopy. One approach is to use fluorescent probes that have the same emission wavelength but can be activated by light of different wavelengths^{120,133}. The advantage of this approach is that one does not need to align different emission channels, which can be challenging at the nanometer scale¹³⁴. However, it may induce more crosstalk due to spontaneous activation¹³⁵. It also cannot be used to simultaneously image in two channels which could lower the temporal resolution. The other approach is to use fluorescent proteins or dyes with different emission wavelengths^{136,137}. In conventional fluorescence microscopy, crosstalk of the fluorescence between the two detection channels can be negligible compared to the background signal when the excitation laser power is low. For localization microscopy, high laser power is required to induce ‘blinking’ of the fluorophores. As a result, the crosstalk emission can be much higher than the background. Moreover, the usual approach of crosstalk correction by subtracting pixel values cannot be applied in localization microscopy to preserve the single molecule feature in the fluorescence image. Therefore, the sequential multicolor separation approach is often used. For instance, the molecules in the red channel are first detected, localized and bleached and then the molecules in the green channel are imaged¹³⁶. For live cell samples, simultaneous imaging in multi-channels is preferred as short image acquisition time is needed. For simultaneous imaging, people often separate the signal based on the individual and characteristic emission spectra of the different fluorophores^{137,138}. The photons from the fluorophores emitting at different emission wavelengths are detected in different channels. However, the number of photons detected in each channel depends on the characteristics of the emission spectra, *i.e.*, green fluorophores have more photons in the green/short channel than in the red/long channel while red fluorophores have more photons in the long channel than in the short channel. When the relation between the number of photons detected in the different channels is plotted for each event, separate populations become visible (**Figure 4.3**).

However, since the photons of the fluorophores can be detected in both channels, this method restricts the density of events and thus limits the temporal resolution of

super-resolution imaging. To find the optimal dye pair, we have tried different combinations of fluorophores. Normally, the crosstalk is high in the red region since the emission spectra of dyes often have a long tail in the red region (**Figure 4.4**). Therefore, we have used relatively dark fluorophores for detection in the green channel and bright fluorophores for detection in red channel. Even if the dark green fluorophore has crosstalk in the red channel, it can easily be filtered out due to its low photon count compared to the bright red fluorophores.

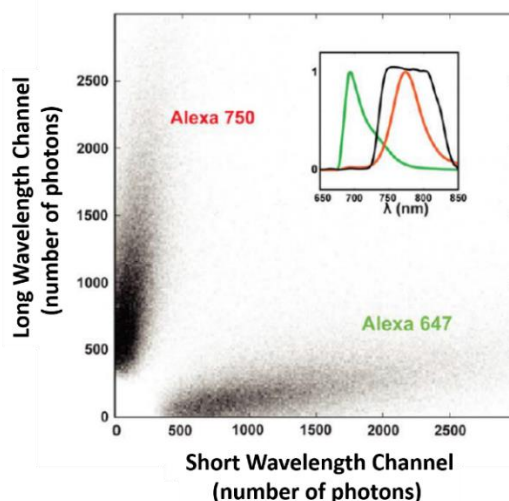


Figure 4.3 Two dimensional distribution of the detected fluorescence photons from switching events in two channels. For Alexa647, the photon count is high in the green (short wavelength, 680 – 740 nm) channel and low in the red (long wavelength, 740 – 830 nm) channel. For Alexa750, the number of photons is low in the short wavelength channel and high in the long wavelength channel. Therefore, events from each dye can be distinguished. Inset: Emission spectra of Alexa750 (red) and Alexa647 (green), the black trace is the transmission curve of the dichroic mirror in the splitter device. Image adopted from Ref.[138].

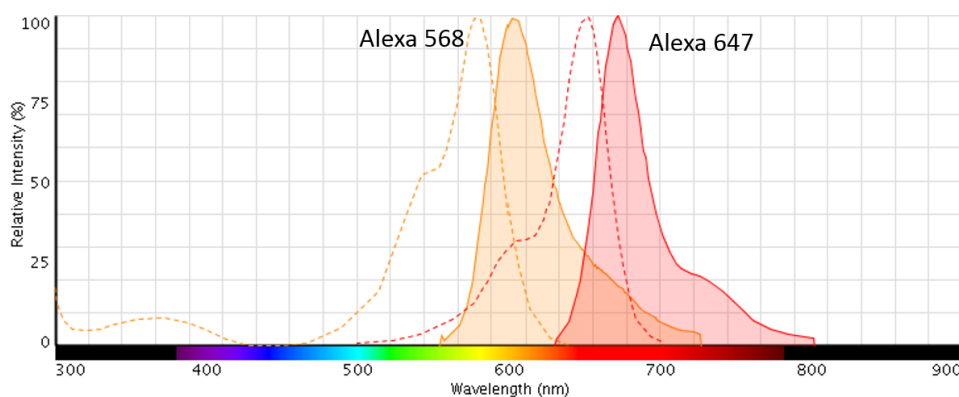


Figure 4.4 Excitation and emission spectra of Alexa568 and Alexa647. Dotted line and solid line represent excitation and emission spectra, respectively. Image created with the Fluorescence Spectra Viewer.

The first combination of fluorophores we have tried was mEos2 to tag clathrin light chain (CLC) and fluorescent Qdot® 705 (Invitrogen) quantum dots (QDs) as NPs. The advantage of QDs is that they have a wide absorbance and narrow, symmetric emission with a size-dependent emission maximum. However, upon steady illumination, the QD emission continuously shifted toward shorter wavelengths due to a continuous size reduction of the CdSe core due to photooxidation¹³⁹. This process happened in less than 1 min in our experimental setup, leading to pronounced crosstalk with mEos2. Next we tried to combine mEos2 and Alexa647 which are both good fluorophores for localization microscopy. However, we quickly found that the emission of Alexa647 was very strong in the 582/50 (mEos2) channel upon 561 nm laser illumination. It was very hard to distinguish mEos2 and Alexa647 in this channel which makes dual color super-resolution imaging difficult¹⁴⁰. Similar results were also obtained for Atto655.

Finally, we have selected dark red (Ex/Em: 660/680 nm) carboxylated polystyrene (PS40) NPs (Invitrogen) with a nominal size of 40 nm because they were found to have negligible crosstalk with mEos2 (**Figure 4.5**). PS40 NPs were added to the CLC-mEos2 transfected COS-7 cells. The emission of the PS40 NPs was detected in the red channel (697/75) and the emission of mEos2 was detected in the green channel (582/50). For each channel, 4,086 images were averaged, and the intensity in the same area (yellow line in **Figure 4.5a** and **b**) was plotted (**Figure 4.5c**). The crosstalk between the two channels was very low.

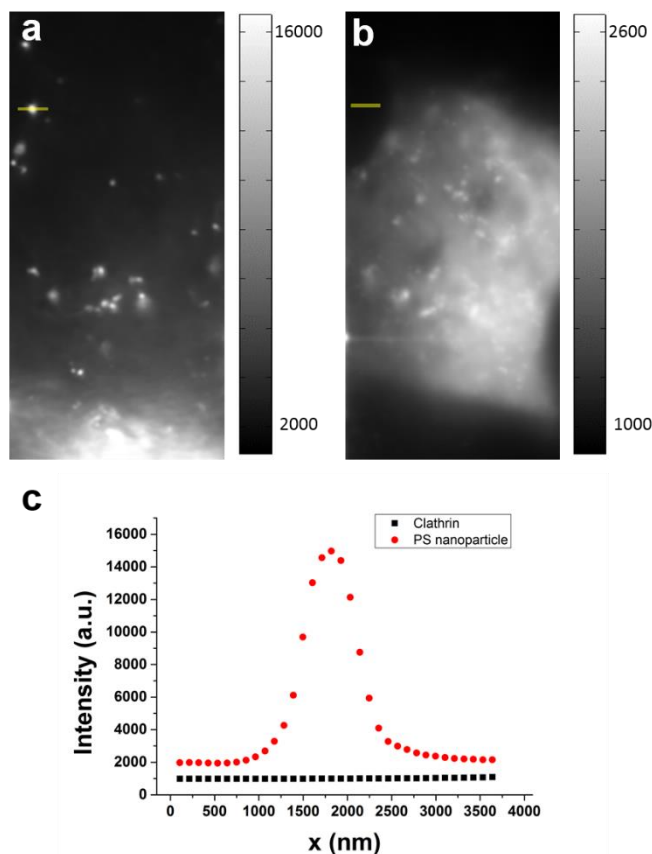


Figure 4.5 Raw two-color TIRF image of a CLC-mEos2 expressing COS-7 cell exposed to PS40 NPs. PS40 NPs and CCPs were simultaneously imaged with the iXon897 camera in two color channels. (a) Average of 4,086 images in the PS40 NPs channel. (b) Average of 4,086 raw images in the CLC-mEos2 channel. (c) Fluorescence intensity plot of cross sections (500 nm wide) through the same position of the PS40 NP channel (yellow line in a) and the CLC-mEos2 channel (yellow line in b) indicating that crosstalk between the two channels is negligible. The columns on the right hand side in panels a and b represent the intensity values.

4.3 Single Particle Tracking and Moment Scaling Spectrum Analysis

Single-molecule fluorescence techniques are particularly appealing to investigate the NP-cell interactions in live cells as the entry of NPs into cells is often heterogeneous. Compared to ensemble methods (*i.e.*, flow cytometry, gene expression studies), where the information on inhomogeneous behavior, kinetic variability or local heterogeneity is often lost¹⁴¹, single particle tracking provides detailed kinetic information during the entire entry pathway.

In most cases, the raw data from SPT experiments comprise a series of time-lapse images acquired by the microscope camera. To quantitatively analyze the motion of individual particles, their trajectories need to be reconstructed from the raw data. The

image analysis methods can generally be divided into two steps: (i) particle detection and (ii) particle linking. Particle detection has already been discussed in Chapter 2. After molecule localization, the positions were passed to a tracking program (<http://physics.georgetown.edu/matlab/>) which is based on the nearest neighbors algorithm written in Matlab.

The motional behaviour was obtained by analyzing the resulting trajectories. The most common approach is to analyze the mean square displacement (MSD) as a function of time to determine the motion type (diffusive, directed, confined) and yield the relevant parameters (diffusion coefficient, transport velocity, size of confinement domain, *etc.*). Normal and anomalous diffusion in 2D are described by

$$\langle \mathbf{R}^2 \rangle = \Gamma t^\alpha, \quad (4.5)$$

where Γ is the transport coefficient, t is the time interval, and the exponent, α , distinguishes the motion type: anomalous subdiffusion ($\alpha < 1$), anomalous superdiffusion ($\alpha > 1$) and normal or Brownian diffusion ($\alpha = 1$)^{142,143}. For anomalous diffusion, the diffusion coefficient is time dependent, with $D(t) = \frac{1}{4} \Gamma t^{\alpha-1}$. In normal diffusion, the MSD is proportional to the time interval and the diffusion coefficient is constant, with $D = \frac{1}{4} \Gamma$.

To characterize the motion of the NPs, we have performed a moment scaling spectrum (MSS) analysis^{144,145}. This analysis is based on calculating different moments of displacements,

$$\mu_\nu(\delta t) = \langle |\mathbf{R}(t + \delta t) - \mathbf{R}(t)|^\nu \rangle, \quad (4.6)$$

where $\mathbf{R}(t)$ is the position vector at time t , δt is the time interval, ν is the order of the moment. The special case of $\nu = 2$ is called MSD. Assuming that each moment obeys a power law, $\mu_\nu \propto \delta t^{\gamma_\nu}$, the scaling coefficients γ_ν were determined by linear regression to the double-logarithmic plots of μ_ν versus δt . Here, the value of $D(t)$ at 1 s, D_0 , was obtained from the y-axis intercepts y_0 of the second order as: $D_0 = 4^{-1} \exp(y_0)$. The plot of γ_ν versus ν is termed moment scaling spectrum according to Ferrari *et al.*¹⁴⁶. The slope of this line (S_{MSS}) characterizes the modes of motion within the same trajectory. S_{MSS} values of 0, 0.5, 1 correspond to immobility, free diffusion and directed movement, respectively. S_{MSS} values between 0 and 0.5 indicate confined motions and values between 0.5 and 1 show superdiffusion. The main advantages of the S_{MSS} method over the $\langle \mathbf{R}^2 \rangle = \Gamma t^\alpha$ classification are a smaller error because of the good linearity of the MSS (**Figure 4.6**) and a clearer distinction between modes of motion¹⁴⁵.

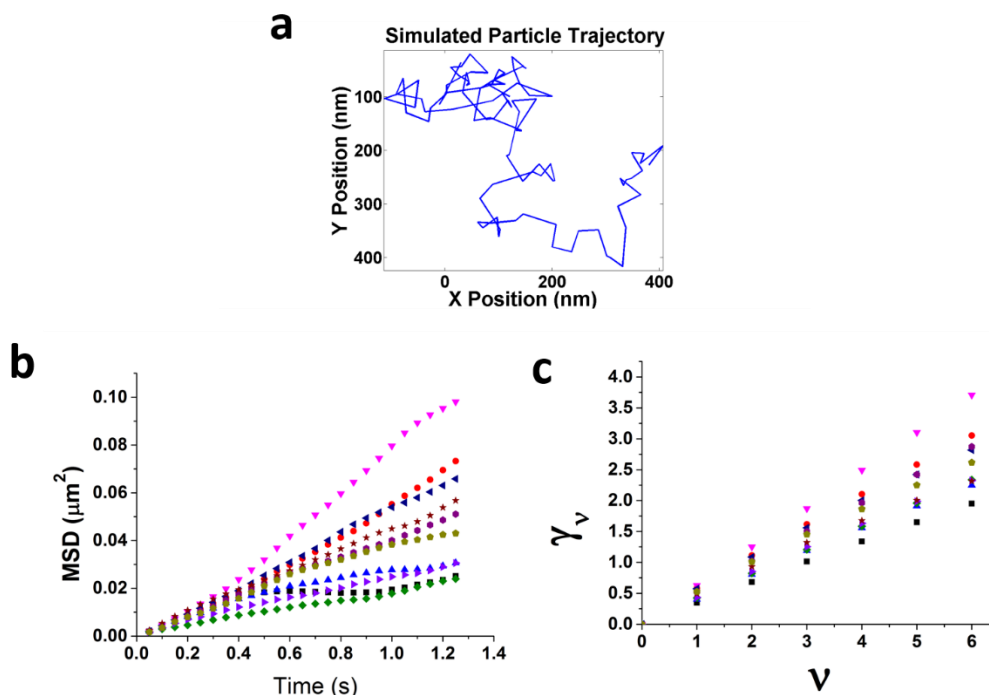


Figure 4.6 Mean square displacement and slope of the MSS analysis. (a) Simulated particle trajectory with a Brownian diffusion coefficient of $0.01 \mu\text{m}^2/\text{s}$. (b) MSD as a function of time for ten simulated particle trajectories with the same Brownian diffusion coefficient of $0.01 \mu\text{m}^2/\text{s}$ versus time. (c) Corresponding MSS of the trajectories in (b). Different from the temporal dependence of the MSD, the MSS analysis shows a straight line.

By plotting D_0 versus S_{MSS} , we can compare all trajectories in a single plot without arbitrary selection. Three modes of motion can be distinguished: (i) immobile ($D < 2 \times 10^{-3} \mu\text{m}^2/\text{s}$; **Figure 4.7**, trajectory 1); (ii) confined diffusion ($D > 2 \times 10^{-3} \mu\text{m}^2/\text{s}$, $S_{MSS} < 0.5$; **Figure 4.7**, trajectory 2); (iii) directed movement ($S_{MSS} > 0.5$; **Figure 4.7**, trajectory 3).

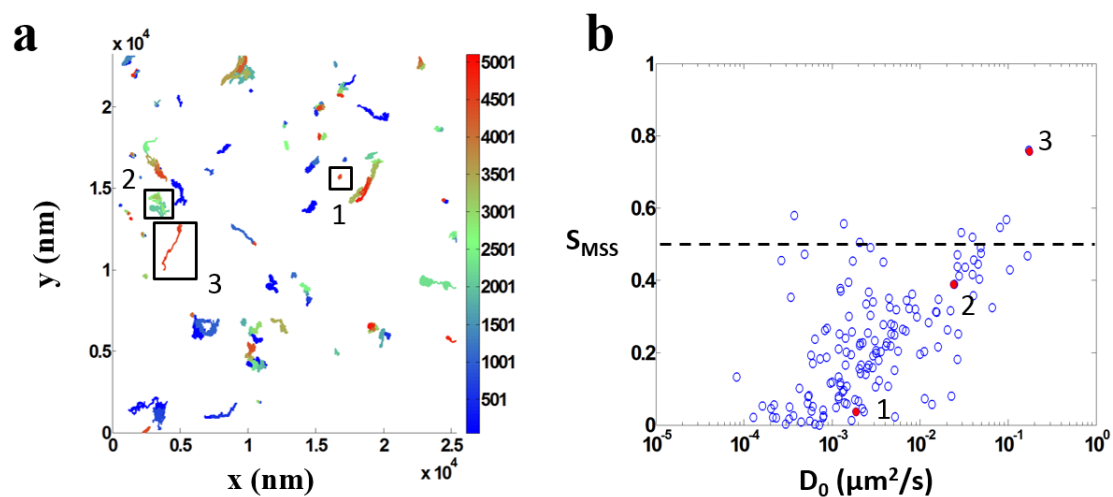


Figure 4.7 Representative trajectories in the S_{MSS} versus D_0 plot. (a) Trajectories of PS20 NPs diffusing on a COS-7 cell. The color scale represent the frame number. (b) Scatter plot of the diffusions coefficients versus the slope of the moment scaling spectrum. The dots marked 1 – 3 represent the trajectories shown in (a).

Chapter 5

Materials and Methods

In this chapter, we will introduce the techniques to fluorescently label cellular samples and purified proteins, and to functionalize the NP surface. Two basic labeling techniques will be discussed: immunohistochemistry and genetic labeling, both of which have been widely applied in cell biology. Furthermore, the imaging buffer for localization microscopy will be introduced.

5.1 Immunostaining

Immunofluorescence utilizes fluorescently labeled antibodies to detect specific target antigens. These labeled antibodies bind to the antigen of interest which allows antigen detection through fluorescence techniques. One can distinguish between direct and indirect immunofluorescence labeling methods. For direct immunofluorescence labeling, the antibody against the molecule of interest is chemically conjugated to a fluorescent dye. More frequently used, however, is indirect immunofluorescence labeling, where two types of antibody are used: the antibody specific for the molecule of interest (primary antibody, unlabeled) and a second anti-immunoglobulin antibody (secondary antibody, tagged with a fluorescent dye) that targets the constant portion of the first antibody. The advantage of direct immunofluorescence is the fast and simple staining procedure. In cases where multiple antibodies are employed in the same species, *e.g.*, two mouse monoclonals, only direct labeling can be used. However, the drawback of this method is the low signal and low flexibility of the labeling procedure due to the fact that there are not many commercially labeled direct conjugates available. In indirect immunofluorescence, the labeling signal is amplified since more than one secondary antibody can attach to each primary antibody. Additionally, commercial secondary antibodies are relatively inexpensive and available with a wide variety of dyes in different colors. The limitations include cross-reactivity when the primary antibody for multi-labeling experiments was raised in the same species. Moreover, samples with endogenous immunoglobulin may exhibit a high background.

We have used indirect immunofluorescence labeling for the cellular samples. It was performed according to the protocol reported in Ref. [147], shown in **Figure 5.1**.

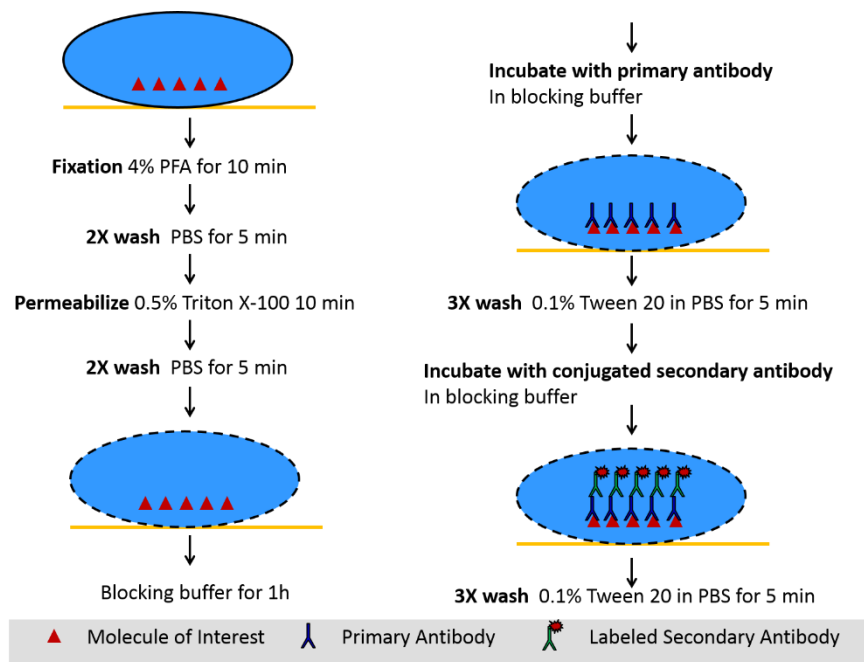


Figure 5.1 Workflow of the protocol for immunostaining. Cells are first fixed with 4% PFA. After washing with PBS, the membrane is permeabilized by 0.5% Triton X-100. After washing, blocking buffer is added to cover the non-specific binding sites. Then, the primary antibody is added. After washing with 0.1% Tween 20, the labeled secondary antibody is added. The final sample is kept in PBS.

- (i) COS-7 cells or HeLa cells were first fixed with 4% paraformaldehyde (PFA, wt/vol, 4 g PFA in 100 ml final PBS solution, pH 7.4) for 10 min at room temperature. Afterwards, two washing steps with phosphate buffered saline (PBS) were performed.
- (ii) After fixation, the cells were permeabilized by 0.5% Triton X-100 in PBS (vol/vol) for about 10 min. After permeabilization, the sample was washed twice with PBS.
- (iii) Then, the cells were incubated in blocking buffer (5% bovine serum albumin in PBS, wt/vol) for 30 min.
- (iv) Cells were then incubated with primary antibody in blocking buffer at different concentrations. For tubulin staining, a 1:2000 dilution ($\sim 1 \mu\text{g}/\mu\text{l}$) of the stock mouse primary antibody was used (monoclonal anti- α -tubulin, T6074, Sigma-Aldrich, St. Louis, USA). For clathrin staining, $1 \mu\text{g}/\mu\text{l}$ rabbit anti-clathrin heavy chain (ab 21679 from Abcam, Cambridge, UK) was applied. The incubation time was either 30 – 60 min at room temperature or overnight at 4°C . Afterwards, the cells were washed three times (each time 5 min) with 0.1% Tween-20 in PBS.
- (v) The fluorescent secondary antibody in blocking buffer was applied to the sample. Since a commercially labeled secondary antibody typically has 2 – 8 fluorophores per IgG molecule (Invitrogen), one should do the labeling in

house, so that the degree of labeling can be adjusted to 0.2 – 0.8 dyes per antibody. Then, the majority of dye-labeled antibody molecules are labeled with only one dye molecule as required in localization microscopy¹⁴⁸. Moreover, different concentrations of secondary antibody should be tried. For dyes with high on/off duty cycles, the concentration should be low. We have used 4 – 7 $\mu\text{g}/\mu\text{l}$ Alexa647 labeled antibody for labeling. After washing three times with 0.1% Tween-20 in PBS, the sample was ready for imaging. Optionally, post-fixation (fix cells for 5 min using 4% PFA in PBS and wash three times with PBS) was applied for longer storage.

The protocol was slightly modified for tubulin labeling. 3% PFA and 0.1% glutaraldehyde in PBS were used to fix the cells for 10 min¹²⁰. Glutaraldehyde is supposed to preserve the structure. Afterwards, the sample was quenched with 0.1% sodium borohydride in PBS for 7 min to reduce the unreacted aldehyde groups and the fluorescent products formed during fixation. A comparison of a fixation with 4% PFA and fixation with glutaraldehyde is shown in **Figure 5.2**. The microtubules of both samples were labeled with Alexa647 (**Figure 5.2a** and **b**). In the zoomed image (**Figure 5.2c** and **d**), microtubules without glutaraldehyde fixation appear blurred, whereas the structure is much better defined with glutaraldehyde fixation.

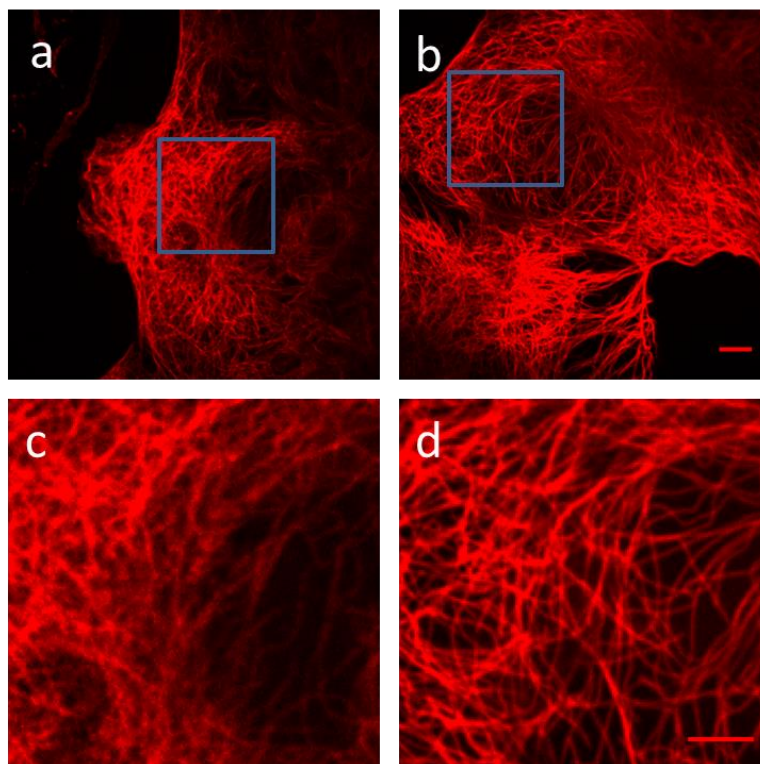


Figure 5.2 Immunostaining of microtubules with and without glutaraldehyde. (a) Fixation of the cell with 4% PFA only. (b) Fixation of the cell with 3% PFA and 0.1% glutaraldehyde. (c) and (d) are the close-ups of the boxed regions in (a) and (b), respectively. Alexa647 were used for labeling. Scale bars, 10 μm (b) and 5 μm (d).

After immunostaining, the fixed sample can be imaged for a long time in order to activate all the fluorophores. However, artifacts may arise due to inadequate labeling. Imperfect sample fixation may lead to broken structures. Low labeling efficiency may limit the ability to resolve small structures by localization microscopy. Clustering of the fluorescent probes due to the amplification effect of indirect immunofluorescence labeling may also generate some artificial clusters. These artifacts are not observed when using conventional fluorescence microscopy techniques since they don't have the ability to resolve them. Higher resolving power demands more stringent sample preparation.

5.2 Tagging by Fluorescent Proteins

Another method to label a protein of interest inside a cell is the use of fluorescent proteins. Genetically expressed PA-FPs may be used for localization microscopy. Compared to immunostaining, this approach has some key advantages¹³⁶: (i) When fused to an endogenously expressed PA-FP, the target protein can be viewed in living cells; (ii) sample preparation is much easier than immunostaining. The genes of the fusion constructs can be introduced into cells using an appropriate vector (*i.e.*, plasmids, viral, cosmids and artificial chromosomes). Transfection can either be transient or stable. Those vectors are widely accessible. After expression of the fluorescent protein, no potentially perturbing detergents, oxygen scavenging agents, or other treatments to manipulate the molecular photophysics need to be applied. (iii) PA-FPs are expressed bound to their respective targets. Therefore, issues such as targeting specificity and unspecific background are eliminated. (iv) The distance between the target protein and the PA-FP (<5 nm) is much less than the distance between secondary antibody and its target protein (>10 nm). With small PA-FP tags, higher labeling densities can in principle be achieved than with an antibody.

There are various transfection reagents that can be used to assist the delivery of plasmid DNA into cells. Most frequently used techniques which can achieve efficient protein expression are calcium phosphate transfection, lipid-based transfection, electroporation and micro-injection. Typically, the most efficient means of delivery, associated with low toxicity, are lipid-based methods. They employ cationic lipids to assist the cell in the uptake of DNA from outside of the cell. The cationic lipids can associate with the negatively charged nucleic acid to form a 'transfection complex'. It mediates the fusion of the complex with the negatively charged cell membrane. Following endocytosis of the DNA by the cells, the complex appears in endosomes and later escapes the endosomal pathway and enters the nucleus for transcription. It is still unclear how the nucleic acids are released from the endosomes and transverse the nuclear envelope.

Many factors may influence the transfection efficiency: 1, cell health. 2, degree of confluency. 3, purity of DNA, 4, amount of DNA used. Therefore, one should try to

optimize parameters such as the ratio of transfection reagent and DNA, the amount of DNA to be transfected, the time that the cells are exposed to transfection reagent, and the presence or absence of serum to achieve optimal transfection efficiency.

In the present work, the transfection procedure was done using PromoFectin (PromoCell, Heidelberg, Germany). This transfection reagent has lower toxicity than the lipofactamine® reagent from Invitrogen. The following protocol describes the transfection of COS-7 cells in 8-well Lab-Tek II chambered cover glass with the CLC-mEos2 plasmid¹³¹. For other cells, optimization may be needed.

Use 1.2 µl of PromoFectin and 375 ng of DNA per well as follows. Scale up and down for other culture vessels according to surface area. Transfection starts when the cells have a density of ca. 50% confluence.

1. For each well, dilute 375 ng of DNA into 40 µl of culture medium without serum (*i.e.*, Dulbecco's modified Eagle's medium, DMEM) or Opti-MEM. Mix with pipette.
2. For each well, dilute 1.2 µl of PromoFectin solution into 40 µl of culture medium without serum or Opti-MEM. Mix with pipette.
3. Add the 40 µl PromoFectin solution to the 40 µl DNA solution, mix immediately with pipette.
4. Incubate for 15 – 30 min at room temperature.
5. Add the 80 µl PromoFectin/DNA mixture drop-wise onto the serum containing medium in each well and homogenize the mixture by gently swirling the plate.
6. After 24 to 48 h, the cells are ready for imaging.

After transfection with CLC-mEos2, mEos2-labeled clathrin in cells shows a punctate structure indicative of CCPs (**Figure 5.3b**). However, in the transfected cells, both non-labeled endogenous CLC and mEos2-labeled CLC (overexpression) are expressed. To test whether the mEos2 image reveals all CCPs, we immunolabeled all CLC with Alexa647, *i.e.*, both the CLC-mEos2 and endogenous CLC (**Figure 5.3a**). As shown in the overlay image, all of the discrete structures in the immunofluorescence image co-localize with those in the mEos2 image.

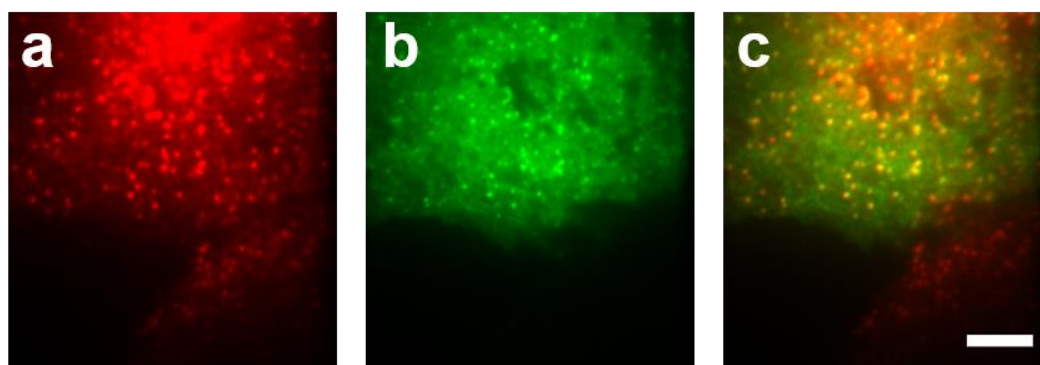


Figure 5.3 Dual-color TIRF image of a COS-7 cell expressing CLC-mEos2. (a) The image in the red channel shows the immunofluorescence of CCPs in a cell that was transiently transfected with CLC-mEos2. Cells were immunostained using an anti-clathrin heavy chain primary antibody and a Alexa 647-labeled secondary antibody. (b) The image in the green channel shows CCPs via mEos2 fluorescence. (c) Overlay image of the two color channels, so puncta with both red and green emission appear in yellow. Scale bar, 5 μm .

5.3 Imaging Buffer

Under standard pressure at 20 °C, the concentration of molecular oxygen in aqueous solutions is typically between 200 to 300 μM ¹⁴⁹. However, in the presence of oxygen, the triplet state lifetime decreases. Reactions between molecular oxygen and fluorophores permanently destroy fluorescence and yield a free radical singlet species that chemically modify other molecules in living cells. Therefore, oxygen scavengers are employed to create anaerobic conditions so that the lifetime of fluorophores is increased by preventing oxygen-based reactions. The most common oxygen scavengers for single molecule experiments are glucose oxidase and catalase (GOC) and protocatechuate dioxygenase (PCD)¹⁵⁰⁻¹⁵². Primary thiols (either β -mercaptoethanol (β ME) or mercaptoethylamine (MEA)) can also be added to the buffer. However, the switching behavior of some dyes (especially red cyanine dyes) is rather sensitive to the thiol concentration^{153,154}.

Our imaging buffer contained TN buffer (50 mM Tris (pH 8.0) and 10 mM NaCl), an oxygen scavenging system (100 U/ml glucose oxidase (Sigma-Aldrich), 1690 U/ml catalase (Merck Millipore, Billerica, MA, USA) and 2% (w/v) glucose) and 143 mM β ME (Sigma-Aldrich). The imaging buffer was only applied to immunostained samples where organic dyes were used. It was prepared freshly and was added immediately before image acquisition.

5.4 Protein labeling

Dyes were purchased as NHS derivatives (succinimidyl ester) and attached to IgG antibodies and transferrin. All dyes were dissolved in dimethyl sulfoxide. Aliquots were

stored at $-20\text{ }^{\circ}\text{C}$. For antibody labeling, $50\text{ }\mu\text{l}$ of the secondary antibody (1 mg/ml , 610-701-124, Rockland Immunochemicals, Gibertsville, PA) was mixed with $40\text{ }\mu\text{l}$ PBS, and then the dye was added at varying concentrations (typically at a final concentration of $10\text{ }\mu\text{M}$). Finally, $10\text{ }\mu\text{l}$ of 1 M NaHCO_3 was added. The mixture was incubated at room temperature in the dark for 30 min. Afterwards, the labeled antibodies were purified by gel filtration columns (Bio-Spin 6 Columns, Bio-Rad). The labeling ratio was determined by using a UV-Vis spectrophotometer (NanoDrop 2000c, Thermo Fisher Scientific, MA, USA). For Tf labeling, $50\text{ }\mu\text{l}$ of 1 mg/ml Tf solution in PBS were mixed with another $40\text{ }\mu\text{l}$ of PBS, $1\text{ }\mu\text{l}$ of $2.5\text{ }\mu\text{g}/\mu\text{l}$ Alexa 647 succinimidyl ester (Invitrogen) in DMSO and, subsequently, $10\text{ }\mu\text{l}$ of 1 M NaHCO_3 ($\text{pH } 8.0$) were added. The solution was shaken for 30 min at room temperature in the dark. Labeled Tf were purified by gel filtration using Bio-Spin 6 column (Bio-Rad, CA, USA). The Tf:dye labeling ratio was determined by a Nanodrop 2000c spectrometer (Thermo Fisher Scientific) to be about 3 dye molecules per Tf.

5.5 Cell Culture

The COS-7 cells were cultured at $37\text{ }^{\circ}\text{C}$ and 5% CO_2 in Dulbecco's modified Eagle's medium (DMEM), supplemented with 10% fetal bovine serum, 100 U of penicillin, and $100\text{ }\mu\text{g/ml}$ streptomycin. Cells were seeded in eight well LabTek chambers to a density of ca. 50% confluence. 1 day after seeding, cells were transfected with CLC-mEos2 (gift of X. Zhuang, Harvard University) using promofectin (PromoCell, Heidelberg, Germany) according to the protocol given above. COS-7 cells were exposed to carboxylated PS NPs (Fluospheres, dark red 660/680, Invitrogen, Grand Island, NY, USA). Before exposing the PS NPs to cells, cells were incubated with serum free DMEM for 30 min. For PS20, PS40, PS200 and PS40-PEG(10k)-Tf NPs, 0.5 nM NPs were applied. For the PS40-Tf NPs, 20 nM NPs were added due to the low binding affinity of PS40-Tf NPs to the cell membrane. Only higher concentrations of PS40-Tf NPs enabled the observation of PS40-Tf NPs on the basal membrane.

5.6 Inhibitor Studies

To examine the effect of chlorpromazine, an inhibitor of clathrin-mediated endocytosis, cells were pre-incubated for 30 min with $10\text{ }\mu\text{g/ml}$ chlorpromazine hydrochloride in serum-free DMEM medium prior to their exposure to NPs. Then, $200\text{ }\mu\text{l}$ of a solution containing the same inhibitor concentration plus PS40 or PS200 NPs (final concentration $20\text{ }\mu\text{g/ml}$ in serum-free DMEM, $\sim 1\text{ nM}$ for PS40 and 0.01 nM for PS200) were added to the cells grown in eight-well LabTek chambers and incubated for 2 h. After 2 h incubation, $200\text{ }\mu\text{l}$ of $0.5\text{ }\mu\text{g/ml}$ CellMaskTM Orange (Invitrogen) in DMEM were added to the COS-7 cells and incubated for 5 min. The cells were washed three times with PBS before imaging. For a quantitative analysis of NP uptake, we acquired

dual-color spinning disk confocal images at cross sections $\sim 2 \mu\text{m}$ above the bottom membrane. For each cell, the fluorescence intensity of the internalized PS NPs was quantified by dividing the integrated intensity by the cell area¹⁵⁵. The intracellular region was identified manually based on the membrane staining using ImageJ.

5.7 PS40 Nanoparticle Functionalization

The PS40 NPs were functionalized with Tf. Either Tf was directly bound at the PS40 surface or Tf was modified with a PEG linker before attaching on the PS40 NPs.

5.7.1 Directly Coupled PS40-Transferrin NPs

To directly conjugate Tf to the PS40 NP surface, EDC (or EDAC; 1-ethyl-3-(3-dimethylaminopropyl)carbodiimide hydrochloride) was used. EDC is the most popular carbodiimide used for conjugating carboxylates and amines. The schematic of the synthesis is shown in **Figure 5.4**.

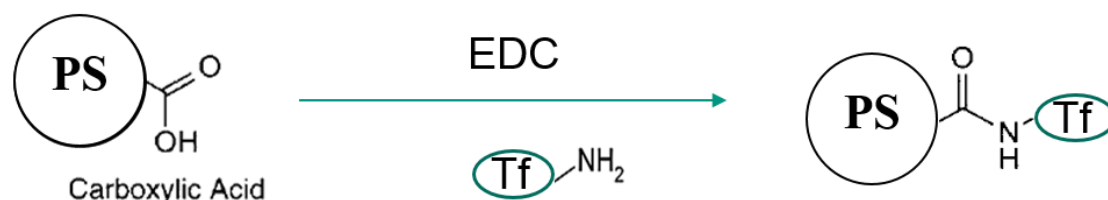


Figure 5.4 Direct coupling of Tf on the carboxylated PS40 NP surface.

96 μl of 1 μM carboxylated polystyrene NP (PS40, 40 nm nominal diameter, Ex/Em:660/680 nm, Invitrogen, Grand Island, USA) suspension were mixed with 304 μl MES buffer (50 mM, pH 6.0) and added dropwise, while shaking, to 400 μl of apo-Tf (freeze-dried powder, Sigma-Aldrich) dissolved in MES buffer at a concentration of 5 mg/ml. 4 mg of EDAC were freshly dissolved in 20 μl MES buffer and added to the suspension. The particle-transferrin solution was kept for 2 h in the dark, and then purified by three dialysis runs of 24 h each against phosphate buffer solution (PBS, Invitrogen, pH 7.4) at 4 $^{\circ}\text{C}$. The selectivity of the conjugation and the final orientation of the Tf on the NP surface depend on the number of nucleophilic functions on the protein¹⁵⁶. Proteins may also crosslink and, therefore, the Tf coating on the PS40 NP surface may not be a monolayer.

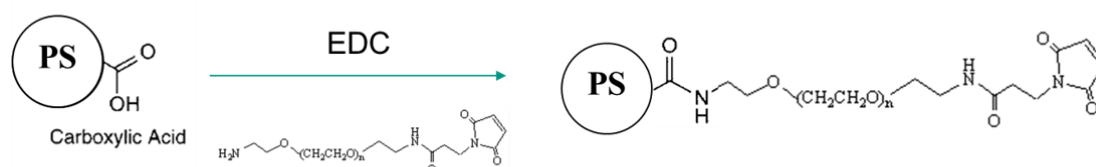
5.7.2 Tf modified with a PEG linker (PS40-PEG10k-Tf)

PEG spacers are expected to preserve the protein function by moving the active moiety away from the particle surface¹⁵⁷ and to obtain a protein surface monolayer. In order to introduce a PEG linker between Tf and PS40 NP, a two step reaction was used (**Figure 5.5**). 1. Both PS40 and Tf were functionalized with a different reactive group. A Mal-

PEG_n-NH₂ PEG-Linker was used to introduce a maleimide group on the PS40 NP surface. SAT(PEG)₄ was used to react with an amine group on the Tf and add the sulfhydryl group to the protein. 2. In the final conjugation step, the maleimide group on the PS40 NP surface was coupled with the thiol group present on the Tf to form a stable thioether bond.

Tf was dissolved in degassed PBS (pH 7.4) at a concentration of 5 mg/ml. 20 μl PEGylated N-succinimidyl S-acetylthioacetate (SAT(PEG)₄, 1 mg/ml, Thermo Fisher Scientific) in dimethyl sulfoxide (0.047 μmol SAT(PEG)₄) was added to 1ml of this solution (0.0625 μmol Tf). After 30 min shaking at room temperature, 100 μl deacetylation buffer (0.5 M hydroxylamine, 25 mM ethylenediaminetetraacetic acid (EDTA) in PBS, pH 7.4) was added. After 2 h reaction while shaking, tris(2-carboxyethyl) phosphine (TCEP) (1 mM) was added and incubated for 5 min. The solution was then run through a Sephadex G25 spin column in deoxygenated HEPES buffer (pH 7.4). A PS40 NP suspension (10 mg/ml) was added dropwise to a stirring equal volume solution of NH₂-PEG_n-Mal linker (M.W. = 10 kDa, 10 mg/ml, Creative PEGWorks, Winston-Salem, NC, USA), both in MES buffer (50 mM, pH 6.0). EDAC (final concentration 1 mg/ml) was then added to the suspension. The reaction was allowed to proceed under stirring for 2 h. Following the reaction, the suspension was purified by a Sephadex G25 column with PBS buffer. The resulting suspension was added to the suspension of SAT(PEG)₄ modified Tf. Following another 2 h of reaction, the NP suspension was purified by three dialysis runs against PBS (pH 7.4) at 4 °C for 24 h each.

1. PS conjugation with Mal-PEG_n-NH₂ Linker



2. Tf conjugation with SAT(PEG)₄

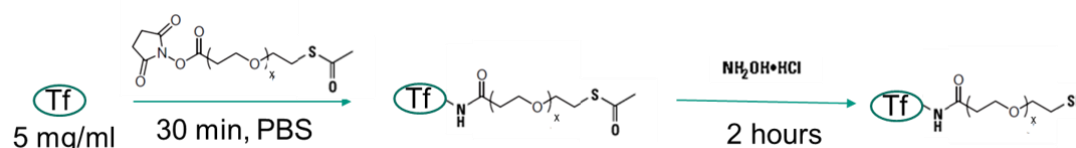


Figure 5.5 Preparation of PEGylated Tf NPs. PS40 NPs were modified with Mal-PEG_n-NH₂ to introduce maleimide groups on the NP surfaces. Tf was modified by SAT(PEG)₄ to introduce a thiol group. The two products were subsequently ‘clicked’ by the thiol-maleimide reaction at the particle surface.

5.7.3 Characterization of PS NPs

Dynamic light scattering and ζ -potential measurements were performed in serum free DMEM media using a Zetasizer Nano-ZS instrument (Malvern Instruments, Malvern, UK) with a 633 nm laser at 25 °C. Each measurement is an average of 5 runs of 100 individual measurements. The size of a Tf molecule is $\sim 7 - 10$ nm. However, the diameter of the PS40-Tf NPs was 101 ± 9 nm while the diameter of the bare PS40 NPs was 62 ± 3 nm. Therefore, Tf is probably forming a multi-layer on the PS40 NPs surface.

Table 5.1 Physico-chemical characterization of bare and functionalized PS NPs.

Sample	Diameter (nm)	ζ in DMEM (mV)
PS40	62 ± 3	-23.7 ± 1.1
PS40-Tf	101 ± 9	-8.4 ± 0.6
PS40-PEG(10k)-Tf	115 ± 6	-9.5 ± 0.7
PS20	36 ± 1	-33.7 ± 1.9
PS200	216 ± 2	-33.2 ± 2.7

Chapter 6

Super-resolution Imaging of Microtubules and Clathrin Coated Pits

During the development of localization microscopy techniques, subcellular structures with well characterized dimensions of 10 – 50 nm such as microtubules, actin, clathrin-coated pits, mitochondria, the endoplasmic reticulum and focal adhesion complexes⁸ were frequently imaged as proofs of principle. In this chapter, we will demonstrate the advantage of localization microscopy using both dSTORM⁷⁰ and PALM⁶⁸ to image microtubules and CCPs, respectively. Some technical details of acquiring a good super-resolution image are also discussed.

6.1 Super-resolution Imaging of Microtubules

Microtubules are a component of the cytoskeleton. They are hollow tubes consisting of polymerized α -tubulin and β -tubulin heterodimers. The $\alpha\beta$ dimers pack together via noncovalent bonding to form the wall of the hollow cylindrical microtubule (**Figure 6.1a**). The tube consists of 13 parallel protofilaments, which are linear chains of tubulin dimers with α - and β -tubulin alternating along its length (**Figure 6.1b** and **d**). All protofilaments have the same structural polarity, with a designated plus end (β -tubulin end) and a minus end (α -tubulin end). The diameter of the tube is 25 nm¹⁵⁸ (**Figure 6.1d** and **e**). Molecular motors use these tubes as tracks to transport vesicles, organelles and other cell components. Two types of motor proteins can be distinguished based on the directional movement toward each end: kinesins move toward the plus end and dyneins move toward the minus end. Microtubules are the most frequently used model system for super-resolution imaging.

We have labeled α -tubulin in fixed COS-7 cells with Alexa 647 using immunostaining. PBS buffer solutions in the sample were exchanged with imaging buffer immediately before dSTORM data acquisition. The resultant fluorescence image is shown in **Figure 6.2a**. Due to the resolution limit in far-field microscopy, the full width half maximum (FWHM) of the microtubules in the conventional fluorescence image is about 400 nm (**Figure 6.2c**). By using 3D localization microscopy, we obtained a super-resolved image of the microtubules (**Figure 6.2b**). The lateral FWHM was only 54 nm (**Figure 6.2d**). Considering the intrinsic 25-nm width of a microtubule and the length of the primary and secondary antibodies with more than 10 nm (diameter

of secondary antibody immunoglobulin G is 8.4 nm^{159}), the image represents the real microtubules very well.

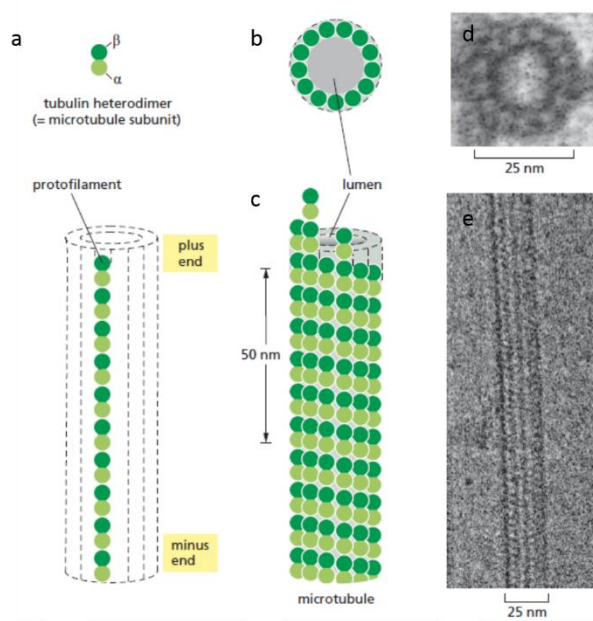


Figure 6.1 Schematic view of microtubules and the electron micrograph. (a) One tubulin subunit and one protofilament made by tubulin heterodimers. (b) and (c) Depictions of tubulin dimers packed together in the microtubule wall. (d) and (e) Electron micrographs showing a cross section and lengthwise view of a microtubule. Image adopted from Ref. [160].

The 3D super-resolution image in **Figure 6.2b** also encodes the axial positions. The 3D view of the cropped subregion in **Figure 6.2b** is shown in **Figure 6.2e**. It shows a compact bundle in all three dimensions. The x - z view and the intensity profile along the axial position are shown in **Figure 6.2f** and **Figure 6.2g**. Compared to the FWHM of conventional 3D confocal microscopy with an axial resolution of $500 - 800 \text{ nm}^{161}$, the FWHM of the microtubule along the axial direction was only 90 nm . Considering the intrinsic size of the microtubule structure, the 3D image was 10 times better resolved in all three dimensions than if it were taken by conventional microscopy.

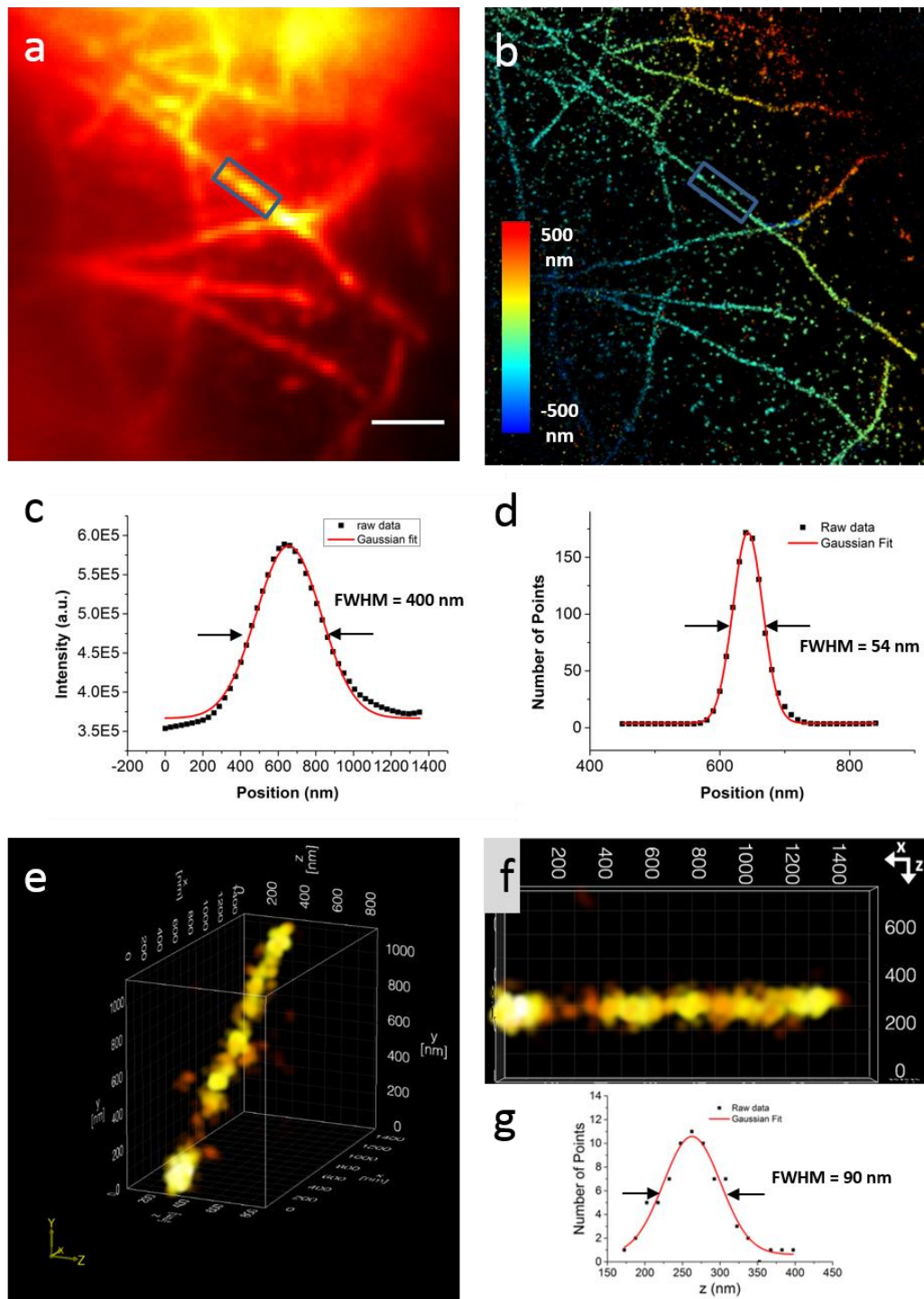


Figure 6.2 3D localization microscopy image of microtubules in a fixed HeLa cell immunostained by Alexa 647. (a) Conventional fluorescence image and (b) 3D super-resolution localization microscopy image of microtubules, respectively. (c) and (d) Lateral intensity profiles along the boxed region in (a) and (b), respectively. Gaussian fitting resulted in a FWHM of (c) 400 nm and (d) 54 nm. (e) 3D view of the boxed region in (b). (f) x-z view of (e). (g) Intensity profile along the axial direction. The FWHM of the microtubule was 90 nm along the axial direction. Scale bar, 2 μm .

The quality of the 3D localization microscopy image critically depends on the sample preparation including the selection of the dye. As described in Chapter 4, sample preparation in super-resolution microscopy is important. Imperfect sample fixation and permeabilization will result in broken structures. Clustering of the fluorescent probes is also a common problem since the fluorophores may undergo repetitive switching and, therefore, appear as an artificial cluster in the final reconstructed image^{70,148}.

The raw image quality is very important for reconstructing a good super-resolution image. With PALM/STORM, people have to pay attention to what is reconstructed by the software and make sense of the super-resolution images. Otherwise, the image may contain many artifacts. The PALM/STORM image is reconstructed by searching isolated molecules in the raw imaging frames. The performance of the molecule detection software often decreases with increasing molecule density and background level. It may either miss real molecules or return molecules with wrong parameters. Especially for 3D super-resolution imaging, the quality of the raw image data is crucial for the final reconstructed image since more parameters are needed to calculate the additional *z*-position.

We have compared the performance of Alexa647 and Alexa488 fluorophores. As shown in **Figure 6.3**, the SNR of Alexa647 labeled microtubules (**Figure 6.3a**) is much greater than that of Alexa488 labeled microtubules (**Figure 6.3b**), which is probably due to the fact that the mean number of photons emitted by a single Alexa488 dye (~1,000 photons) is much smaller than the number of photons emitted by Alexa647 (~5,000)¹⁴⁸. The autofluorescence in the green channel is also stronger than in the far red channel. Although the software can still find ‘bright spots’ as indicated by the red boxes, the reconstructed super-resolution images were quite different in quality between the two dyes (**Figure 6.2** and **Figure 6.4**).

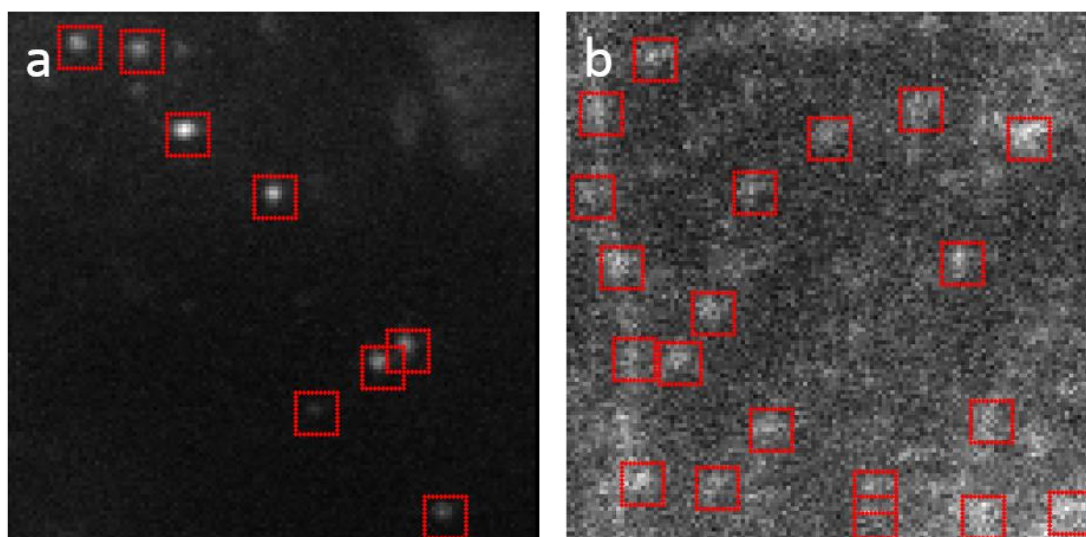


Figure 6.3 Raw dSTORM image frames. (a) and (b) Microtubules immunostained with Alexa647 and Alexa488, respectively. Red boxes indicate the molecule candidates detected by the software.

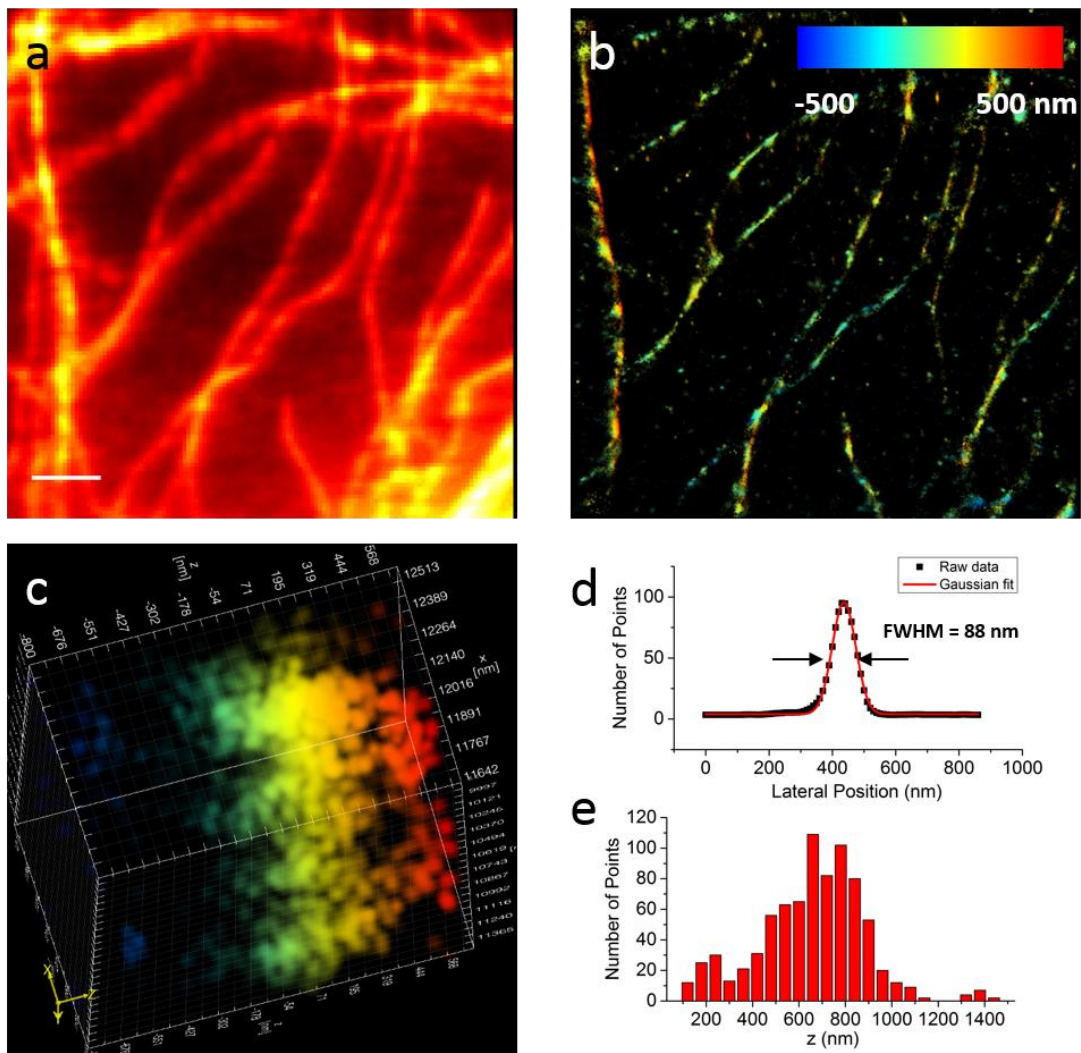


Figure 6.4 3D localization microscopy image of microtubules in a fixed HeLa cell immunostained by Alexa 488. (a) and (b) Conventional fluorescence image and 3D super-resolution image of microtubules. (c) 3D view of the boxed region in (b). (d) and (e) Intensity profiles of (c) along the lateral and the axial directions, respectively. Scale bar, 2 μm .

Compared with a conventional fluorescence image (**Figure 6.4a**), the dSTORM image (**Figure 6.4b**) still reconstructed some finer tubules in lateral direction, with the FWHM of the tubules of 88 nm (**Figure 6.4d**), compared with ~ 400 nm FWHM in the conventional fluorescence image. However, in the 3D view of the tubule structure (**Figure 6.4c**), the points are distributed broadly along the axial direction (**Figure 6.4e**), most likely because the software cannot find the correct σ_x and σ_y of the molecule candidates with strong background.

6.2 Super-resolution Imaging of Clathrin Coated Pits

Clathrin is a protein which plays an important role in the formation of coated vesicles on the membrane. These proteins are used to bud off small vesicles for the transportation of molecules within cells. The function of the vesicles is not only limited to endocytosis of nutrients, but also affects cell signaling, immune response, and cell communication. Viruses may also utilize this pathway to gain entry to the cell during infection.

Clathrin is a trimer of three 190 kDa heavy chains, each associated with a 23 – 26 kDa light chain (**Figure 6.5**). These three pairs of heavy chains and light chains form a triskelion shape. A clathrin triskelion is the assembly unit for the vesicular coating. The triskelia can interact with each other and form a polyhedral lattice surrounding the vesicle. The heavy chain has a very elongated structure, approximately 450 Å in contour length, with 42 α -helical zig-zags connecting a globular N terminal domain with a C terminal trimer hub¹⁶². They provide the structure backbone of the clathrin lattice. The light chain binds near the hub and is thought to regulate formation and disassembly of the clathrin lattice. After assembly of a clathrin coat, a sharp membrane invagination is produced. The radius of the clathrin coated pits ranges from 35 nm to more than 100 nm.

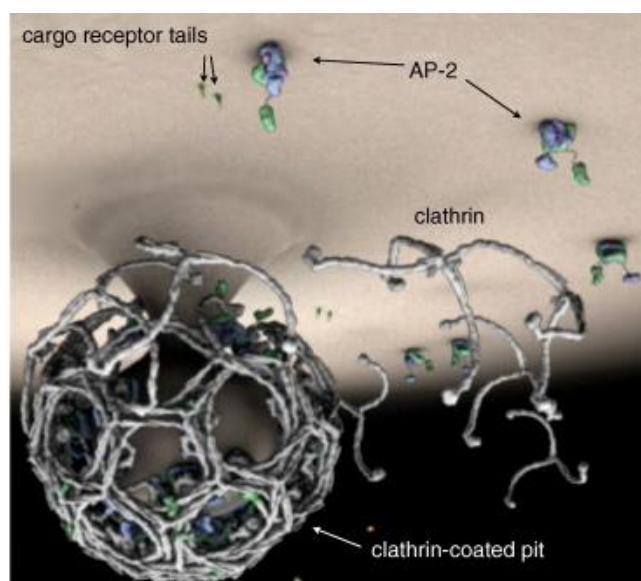


Figure 6.5 Schematic representation of a clathrin coated pit. Three pairs of heavy chains and light chains form a triskelion. These triskelia interact with each other and form a clathrin lattice. Image adopted from Ref. [162].

We have immunolabeled clathrin coated pits with the mouse monoclonal anti-clathrin heavy chain (Abcam) primary antibody. The secondary antibody was labeled either with Alexa647 or with Atto655 to compare the results. The immunostaining procedure has been described in Chapter 5. PBS buffer solutions in the sample were

exchanged with imaging buffer immediately before data acquisition. The dSTORM images are shown in **Figure 6.6**.

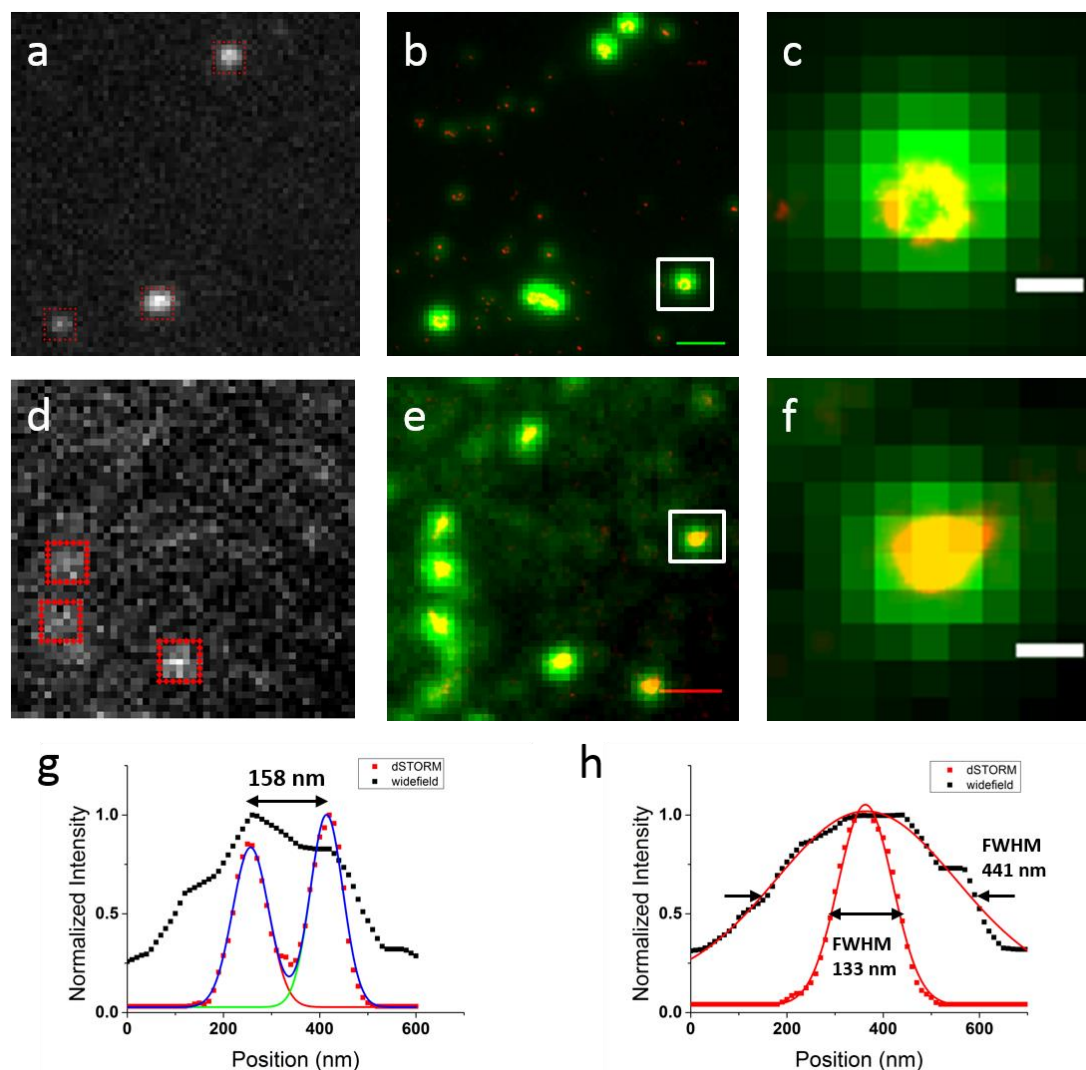


Figure 6.6 dSTORM imaging of clathrin using Alexa647 and Atto655. (a-c) Alexa 647, (d-f) Atto 655 image frames. The red boxes (a and d) are the molecule candidates in the raw image frames detected by the software. (b) and (e) Overlay of TIRF images (green) and super-resolution images of CCPs (red). (c) and (f) Zoomed image of the boxed regions in (b) and (e), respectively. (g) and (h) Intensity plot of (b) and (e), respectively. Gaussian fitting (red and green: single Gaussian, blue: sum) resulted in a separation of 158 nm between the analyzed structures. Scale bars, 1 μm (b and e) and 200 nm (c and f).

As shown in **Figure 6.6a** and **Figure 6.6d**, the SNR of the raw image of Alexa647 is much higher than that of Atto655. **Figure 6.6b** and **Figure 6.6e** are overlay images of the TIRF image (green) and the reconstructed dSTORM image (red) with Alexa647 and Atto655, respectively. For both Alexa647 and Atto655, the reconstructed dSTORM image of the CCPs has a better resolution than the TIRF image. However, the zoomed

images in **Figure 6.6c** and **Figure 6.6f** show a ring structure only for the Alexa647 labeled sample but not for Alexa655. The difference is more obvious in the intensity profiles along a 90-nm wide strip shown in **Figure 6.6g** (Alexa647) and **Figure 6.6h** (Atto655). As shown in **Figure 6.6g**, the dSTORM image of the Alexa647-labeled CCPs shows a ring-like cross-section with a diameter of about 158 nm. In contrast, the hollow center of the ring structure was not resolved in the Atto655 image, which instead showed a Gaussian profile. Compared to Alexa647, Atto655 suffered from lower localization accuracy due to the low photon yield per switching cycle, leading to a reduction in image resolution that blurred the CCP image substantially so that its hollowness was no longer apparent.

We further extended super-resolution imaging of CCPs to live HeLa cells by fusing the photoswitchable fluorescent protein mEos2 to the clathrin light chain. Cells were transfected with the CLC-mEos2 plasmid (gift of X. Zhuang, Harvard University) with promofectin using the protocol described in Chapter 5. Imaging buffer was not needed for mEos2. Cells were imaged directly in the culture medium. Instead of using 50 ms exposure time as for the fixed cell, we used a shorter exposure time of 5 ms. 10,000 images were taken (totally 50 s).

As show in **Figure 6.7a** (TIRF) and **Figure 6.7b** (PALM), the diffraction limited spots of the CCPs in the TIRF image are much bigger than in the PALM image. Some punctate patterns even consisted of two individual CCPs, as indicated by the arrows. The nanoscopic cup-like morphology was resolved in the PALM image (**Figure 6.7c**) which demonstrates the ability of resolving nanoscopic structures in living cell using localization microscopy.

Another interesting observation is that, instead of forming a ring-like structure, some CCPs appeared as two individual spots in the PALM image (**Figure 6.7b**, circle). This might be due to a different morphology of the CCPs on the membrane during endocytosis. Further investigations are necessary to explain these findings.

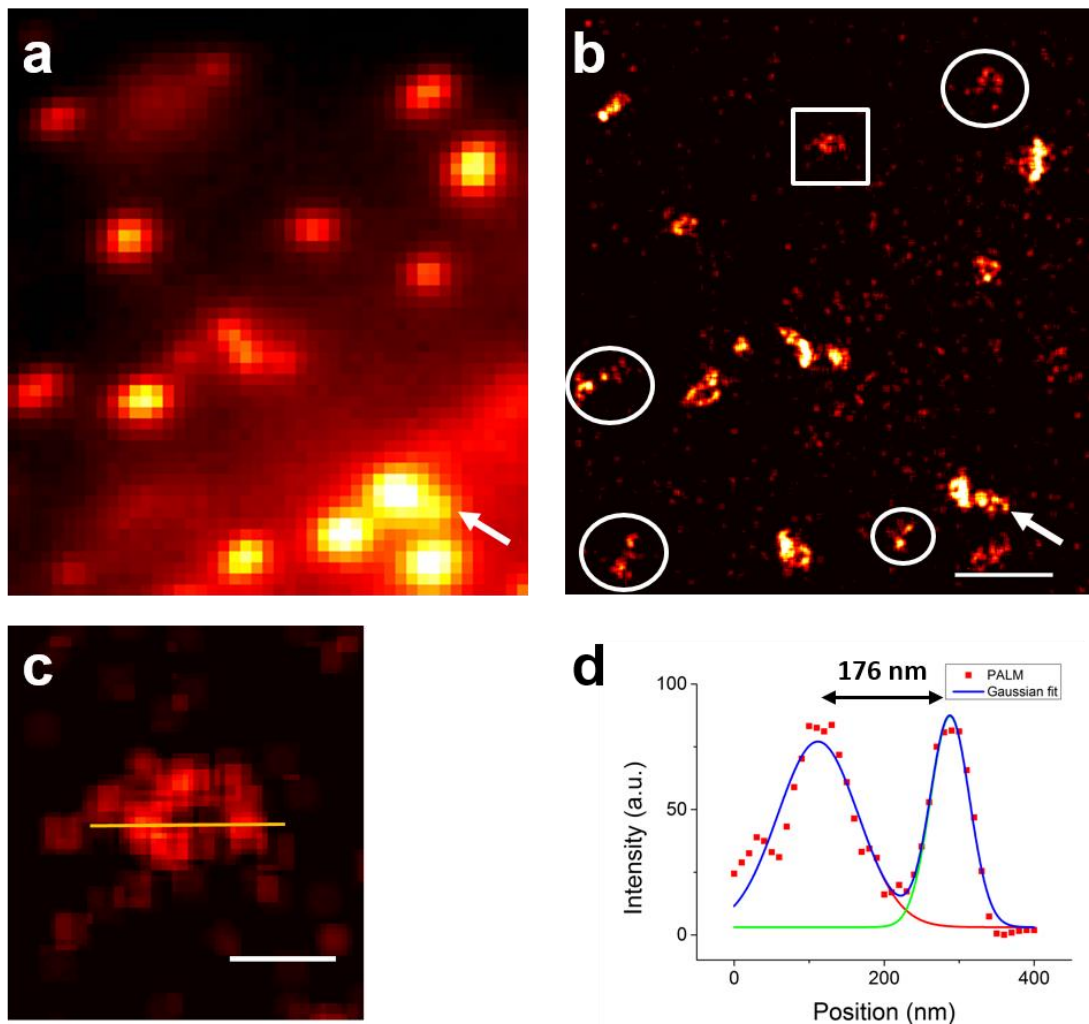


Figure 6.7 PALM image of CLC-mEos2 expressed in a live HeLa cell. 10,000 images were taken at a frame rate of 5 ms (totally 50 s). (a) The average of 800 TIRF images of CLC-mEos2 shows point-like structures of CCPs on the membrane. (b) The PALM image of CLC-mEos2 shows a ring-like structure of many individual CCPs. The circles indicate CCPs that show two individual spots. The arrow shows two CCPs that were resolved in the PALM image and appeared as only one in the TIRF image. (c) Zoomed-in image of the boxed region in (b). (d) Localization density profile along the line drawn in (c) shows the cup-like morphology of the CCP. Scale bars, 1 μm (b) and 200 nm (c).

We also applied the 3D astigmatism super-resolution method to image CLC-mEos2 in living COS-7 cells. Compared to organic dyes, fluorescent proteins emit much less photons. As it is very important to have enough photons for 3D super-resolution imaging of a single molecule so that the returned parameters can precisely encode the axial position, the camera exposure time was set to 100 ms, which is twice the typical camera exposure time for imaging Alexa647. The resulting photon histograms of single CLC-mEos2 molecules at camera exposure times of 5 ms (live cell, **Figure 6.7**) and 100 ms are shown in **Figure 6.8**.

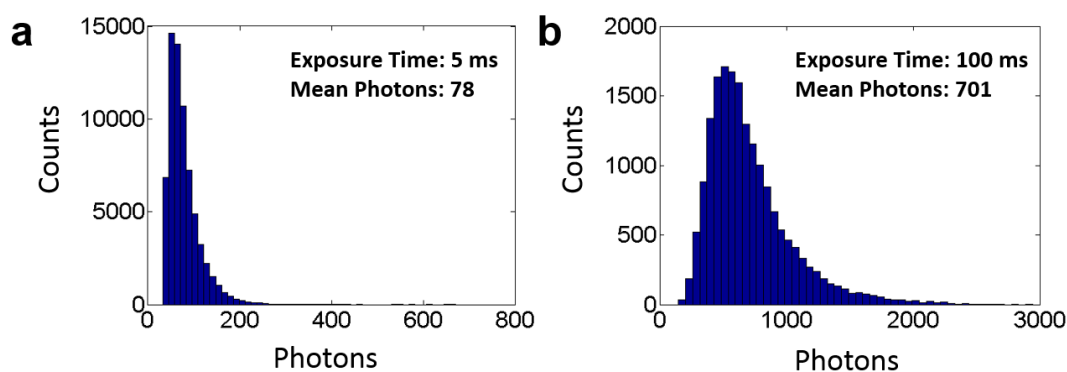


Figure 6.8 Photon histograms of CLC-mEos2 at different camera exposure times. (a) and (b) Photon number distributions of mEos2 at camera exposure times of 5 ms and 100 ms, respectively.

As shown in **Figure 6.8a** and **b**, the mean photon number of CLC-mEos2 with a camera exposure time of 100 ms is ~ 10 times of that with the exposure time of 5 ms. With this high photon count per single molecule, the 3D clathrin image in a living COS-7 cell could be reconstructed as shown in **Figure 6.9**. Inclined illumination (HILO)¹²³ was used for 3D imaging. **Figure 6.9a** and **b** shows the conventional wide field image (average of 100 images) and the PALM image, respectively. The CCPs in the wide-field image appear elongated due to the fact that the cylindrical lens was positioned in front of the camera during image acquisition. The PALM image was reconstructed from 10,000 image frames (16.7 min). The 2D PALM image showed much smaller CCPs compared to the ones in the wide field image. It is interesting to see that some CCPs were again reconstructed as two individual clusters (indicated by cycles) as shown in **Figure 6.9**. These CCPs were darker than other CCPs in the wide field image. Therefore, we suggest that these CCPs were probably about to be internalized. Interestingly, one particular CCP (indicated by the arrow) was found in the PALM image but not in the TIRF images. This CCP may have formed during the long acquisition time. To resolve the ring-like structure of the CCPs, the 2D image was divided into different axial layers (**Figure 6.9c**). Molecules were binned into different layers (25 nm each bin). As shown in **Figure 6.9c**, the molecules only spread ~ 250 nm in the axial direction, which is reasonable considering the size of the CCPs. The nanoscopic ring-like structure could be resolved between 25 and 75 nm. The CCP exhibits larger size in the middle layers (~ 100 nm to 150 nm) than in the edge layers which also agrees well with the spherical shape of the CCP.

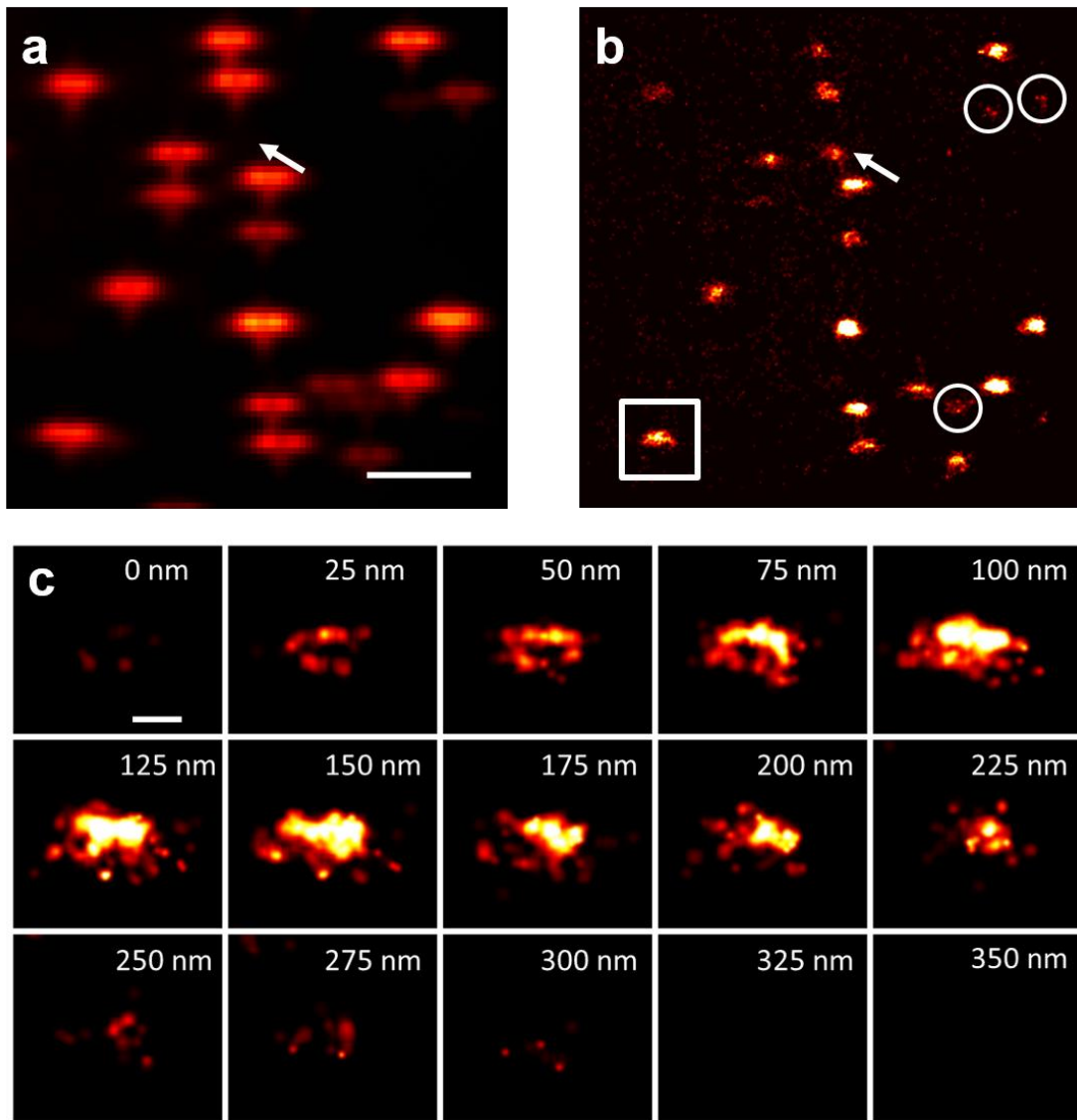


Figure 6.9 3D imaging of clathrin coated pits. (a) Wide field image of CCPs on the bottom COS-7 cell membrane surface. (b) PALM image of CCPs. The circles indicate CCPs that show two individual spots. The arrow shows a CCP that was reconstructed in the PALM image but not seen in the wide field image. (c) The image of the CCP in the boxed region in (b) was divided into different axial layers. Scale bars, 2 μm (a) and 200 nm (c).

Chapter 7

Super-resolution Imaging-based Single Particle Tracking Reveals Fast Dynamics of Nanoparticle-cell Interactions

We have combined the high spatial resolution capability of PALM and the fast temporal resolution of single particle tracking to investigate the critical early stages of the cellular uptake of NPs. Clathrin-mediated endocytosis (CME) is by far the best studied pathway among different endocytosis mechanisms²³. It is responsible for endocytosis of many different NPs⁴⁶. Here, polystyrene (PS) NPs with different size (20 nm, 40 nm and 200 nm) and different surface functionality were chosen as model particles. We have focused on the interaction between PS NPs and CCPs.

7.1 Interaction between Carboxylated PS40 NPs and CCPs

We have already discussed that the PALM images of the CCPs labeled with mEos2 often show ring-like shapes, whereas they only appear as spot-like structures in the conventional TIRF image (**Figure 6.7**), demonstrating the much improved spatial resolution of PALM. Molecules were identified in each frame using the software described in **Section 2.3**⁹¹. The PALM image of CCPs in COS-7 cell was reconstructed from 5,000 fluorescence images of CLC-mEos2 (**Figure 7.1a**). The trajectories of the PS40 NPs were overlaid with the CCPs (**Figure 7.1b** and **Figure 7.1c**). Due to the movement of clathrin during image acquisition, the CCPs appeared blurred in the PALM image. Therefore, we reconstructed the PALM image with shorter time intervals (500 frames, 15 s). Indeed, as shown in **Figure 7.1d**, a much improved quality of the CCP structure was obtained. Dynamic information on even faster time scales could not be obtained from the PALM images. However, by using the trajectories of the NPs as complementary information, one can get additional dynamic insight into the events involving clathrin. An example is shown in **Figure 7.1d**. From 0 – 60 s, the trajectory of the particle was confined to a small area and the clathrin pit in the PALM image was also constrained. From 60 – 120 s, the trajectory of the PS40 NP showed a directed motion over a short distance. Meanwhile, the clathrin structure became more extended. The trajectory of the NP always co-localized with the CCP, indicating co-movement of the PS40 NP and the CCP. From 105 – 150 s, the PS40 NP remained at the same spot

again.

In order to obtain even faster dynamic information, the rolling-window algorithm was applied for subtrajectory analysis¹⁶³. The local mean square displacement (time window: 100 frames and step duration: 20 frames) was fitted by a power law function $MSD = \Gamma t^\alpha$ as described in **Section 4.3**. The time dependent α is shown in **Figure 7.2**. As expected, in the first 60 s and the last 30 s, 54% and 50% of the α values were below 1, showing hindered diffusion, with the remaining events associated with α mostly slightly above 1. From 60 – 120 s, 80% of the α values were above 1, suggesting a super-diffusion process. The detailed analysis of the MSD curves revealed very heterogeneous diffusive motions of the PS40 NPs that co-moved with the CCPs. Even with the PS40 NPs confined in the CCPs (first 60 s and last 30 s in **Figure 7.1d**), the interaction of the CCPs and the sub-membrane cytoskeleton could direct the movement of the CCPs (60 – 120 s in **Figure 7.1d**). Therefore, the motion type of the NPs reflects the interactions between the CCPs and the submembrane cytoskeleton network.

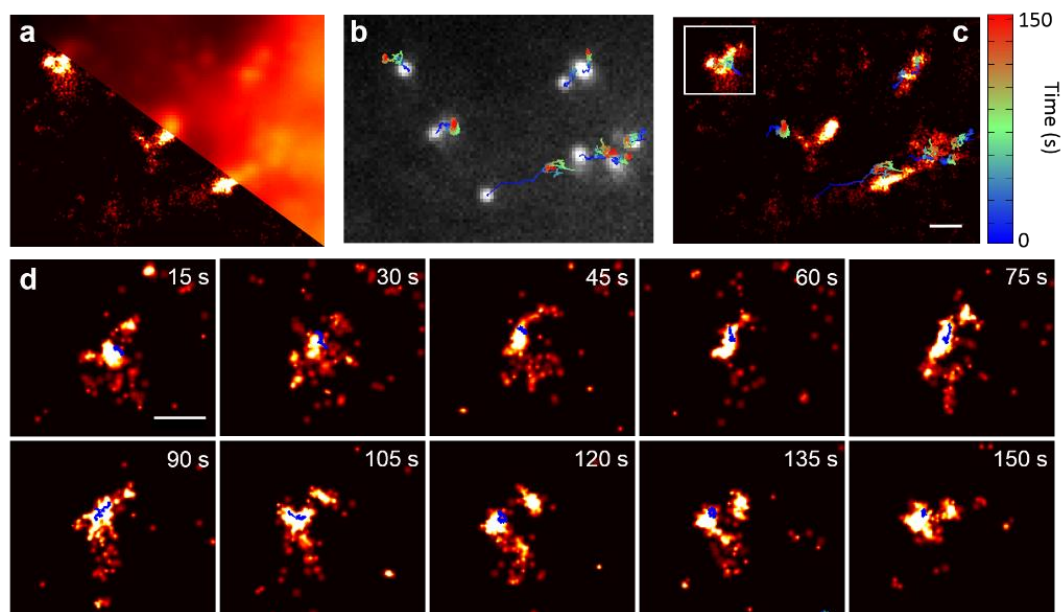


Figure 7.1 Interaction between PS40 NPs and CCPs. (a) Conventional wide field image (top) and PALM image (bottom) of CCPs. (b) Trajectories of PS40 NPs moving on the COS-7 cell. (c) Overlap of the PS40 NPs trajectories with the PALM image of the CCPs. (d) Time-lapse images of higher-magnification views of the boxed region in (c) showing the highly dynamic interaction between PS40 NP and CCP. Scale bars, 1 μm .

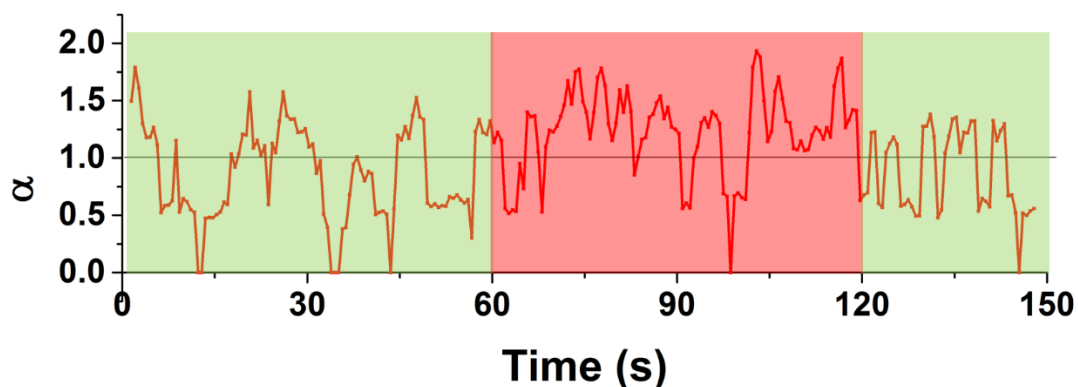


Figure 7.2 Analysis of the time exponent of the *MSDs* calculated from the trajectories shown in **Figure 7.1**. The local mean square displacement (time window 100 frames, step duration 20 frames) was fitted by a power law function, $MSD = \Gamma t^\alpha$. The horizontal line at $\alpha = 1$ refers to free diffusion, $\alpha < 1$ indicates anomalous sub-diffusion, and $\alpha > 1$ super-diffusion. The green and red time windows represent anomalous sub-diffusion and super-diffusion dominated time periods, respectively.

7.1.1 Accumulation of Carboxylated PS40 NPs on the Membrane

Since carboxylated PS40 NPs are closer to each other than the optical diffraction limit if they accumulate, we cannot distinguish the fluorescent spot from a single PS40 NP from that of accumulated PS40 NPs. To overcome the detection barrier, we have used a mixture of NPs emitting in the green and in the red with identical size (40 nm) as a nanoruler¹⁶⁴. Equal volumes of red (660/680) and green (565/580) PS40 NPs (~1 nM each) were mixed and then applied to COS-7 cells. A 561 nm laser and a 640 nm laser were used to excite the green and red NPs, respectively.

The image of PS40 NPs was taken 40 min after adding the NPs (**Figure 7.3**). **Figure 7.3(a)** and **(b)** show the PS40 NPs in the red and green channel, respectively. The two channel images were then merged by the local weighted mean mapping function derived from the calibration using multi-color beads. 33.3% (194/581) of red and green PS40 NPs were found to be co-localized with each other. This result indicates that an individual spot contains one or at most two NPs which is consistent with previous results⁴. In a random combination, another one-third of the spots have two particles of the same color, and the remaining one-third of the spots consists only of a single green or red NP. Note that, the more NPs congregate in one site, the lower is the probability of spots having only a single color.

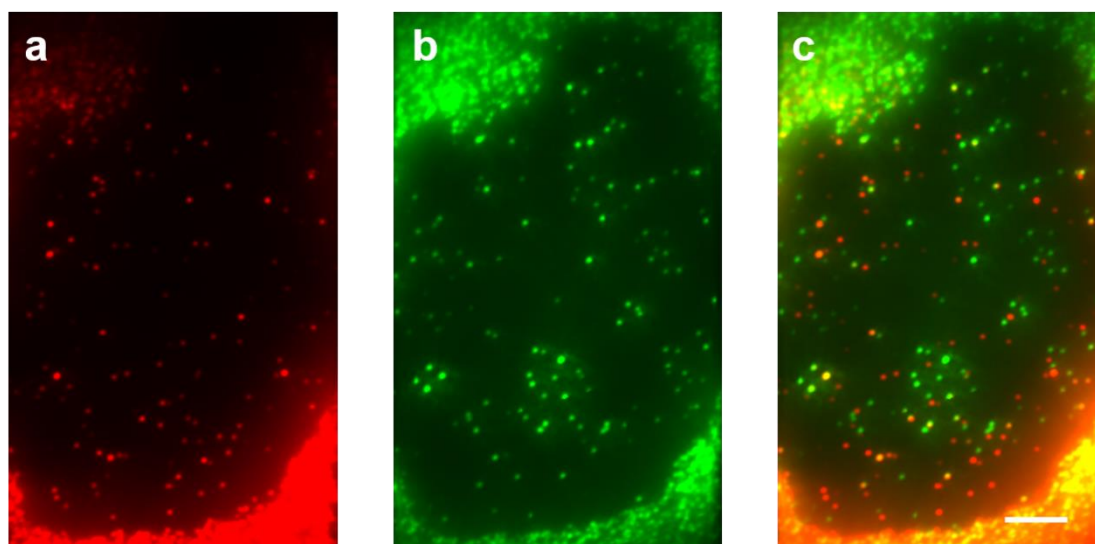


Figure 7.3 NPs (excitation/emission peaks: 565/580 nm), which we refer to as ‘green NPs’, were mixed with equal proportions of red NPs (excitation/emission peaks: 660/680 nm). Lasers emitting light at 561 nm and 640 nm were used to excite the green and red NPs, respectively. Images were taken 40 min after adding the NPs. (a) Red PS40 NPs at the bottom surface of a COS-7 cell, imaged with a band pass filter (697/75). (b) Same view in the green channel, filtered with a band pass filter (582/50). (c) The two images were merged using the image registration method described in Chapter 4. Scale bar, 5 μm .

To quantify particle aggregation on the membrane over time, the cells were fixed at different time points (10, 20, 30, 40 min) after adding the mixed red and green PS40 NPs. The distance between the co-localized green and red NPs is expected to indicate the size of the vesicles that captured the NPs¹⁶⁴. The size of the vesicle was determined by the sum of the distance between the co-localized green and red NPs and their diameters (62 nm from the DLS measurement). The size distributions at the four chosen time points are shown in **Figure 7.4**(a), (b), (c) and (d), respectively. The fraction of red PS40 NPs that were co-localized with green PS40 NPs was 20% (48/245), 25% (102/405), 29% (160/550), 33% (194/581) for 10, 20, 30 and 40 min, respectively. The average vesicle size at the different time points was 167 ± 55 nm, 155 ± 60 nm, 167 ± 70 nm and 160 ± 65 nm. Even though co-localization increases with time, the mean distance between red and green PS40 NPs does not change, indicating that larger aggregates do not form during this time.

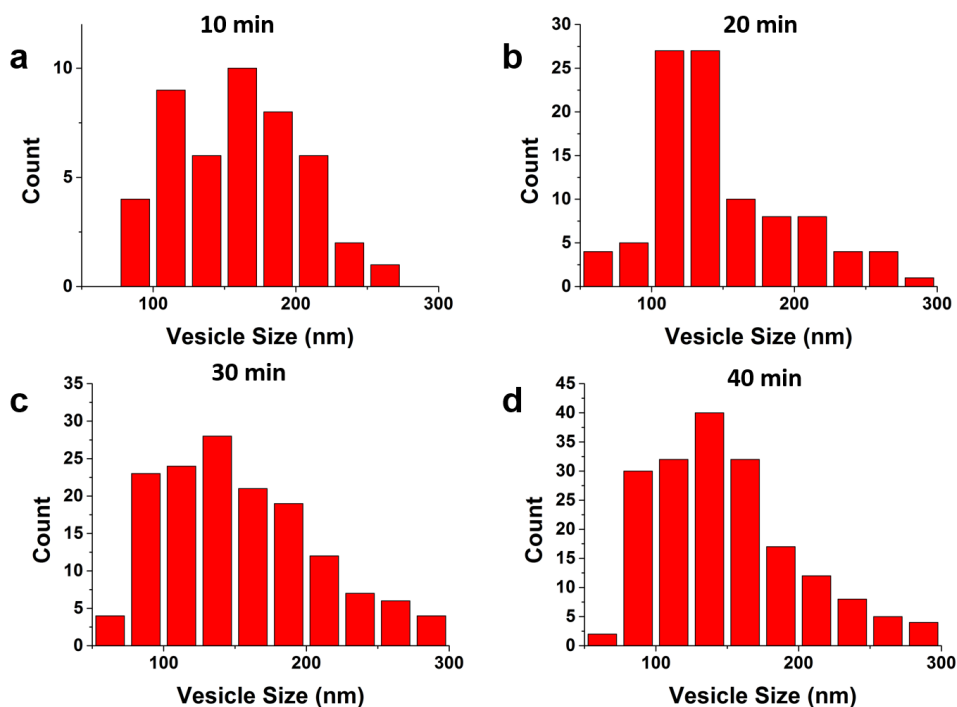


Figure 7.4 Distance between colocalized red and green PS40 NPs. After adding mixed red and green PS40 NPs to COS-7 cells, cells were fixed at different time points. The distance between the co-localized green and red NPs indicates the size of the vesicles that captured the NPs. The vesicle size distributions for at fixation 10, 20, 30, 40 min after NP exposure are shown in panels (a), (b), (c) and (d), respectively.

7.2 Two Types of Interaction between Carboxylated PS40 NPs and CCPs

Interestingly, two distinctly different types of interaction between PS40 NPs and CCPs were observed (**Figure 7.5** and **Figure 7.7**). In more than 80% (48/59) of all events, in the beginning, NPs were bound on the membrane without any CCP present (type I, **Figure 7.5** a-d). After some time, the CCP signal appeared and increased gradually. During this period, the fluorescence intensity of the NPs remained essentially constant. After the signal of the CCPs reached its maximum, the NP emission intensity started to decrease, indicating the beginning of internalization (**Figure 7.5c**). In the final stage, a 100-nm lateral movement of the CCP was observed in both the PALM image of the CCP and the trajectory of the PS40 (**Figure 7.5b**), while the control PS40 NPs outside the cells showed constant intensity and location (**Figure 7.6**). It is noteworthy that the intensity of the PS40 NPs often did not decrease to zero after the complete disappearance of the clathrin signal. However, the decrease of more than 30% of the intensity indicates that the PS40 NPs moved away from the surface. The PS40 NPs probably stay near the membrane and are not immediately transported deeply into the cell after internalization.

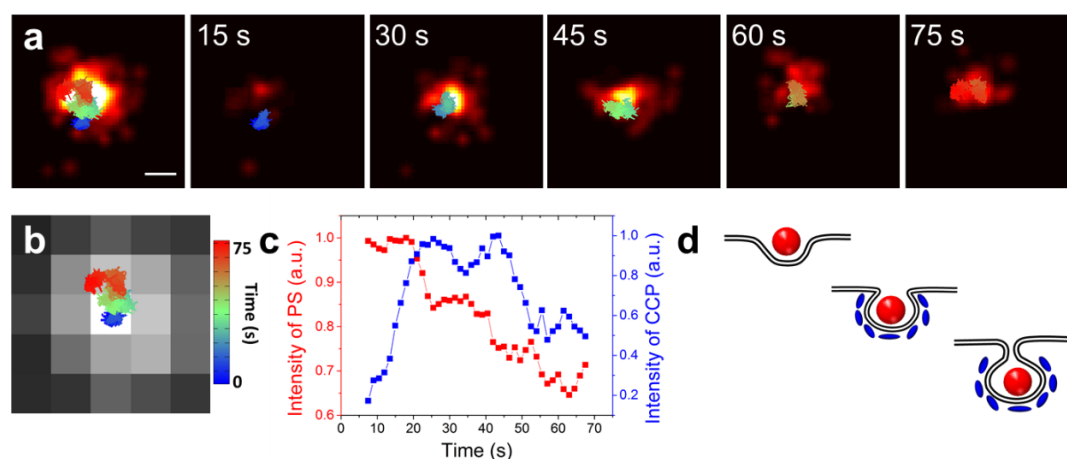


Figure 7.5 Type I PS NP and CCP co-localization. (a) Overlay of PS40 NP trajectory and CCP. (b) PS40 NP trajectory over raw data. A lateral shift of the PS40 NP was observed during the uptake process. (c) The emission intensities of the PS40 NP and the CCP during the uptake process. (d) Schematics of the sequential stages during type I endocytosis of PS40 NP. Red: NP, blue: clathrin. Scale bar, 100 nm. (d, courtesy of Karin Nienhaus.)

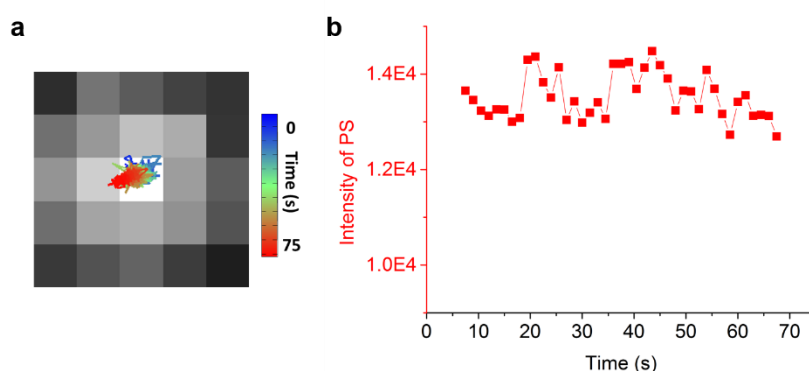


Figure 7.6 Trajectory and intensity distribution of a control PS40 NP adsorbed on the glass surface. (a) The trajectory of the control PS40 NP showed a constant location, with an average standard deviation of the x and y dimensions of 14.7 nm. The average standard deviation of the x and y dimension of the PS40 NP shown in **Figure 7.5b** is 31.8 nm. (b) The intensity distribution of the controlled PS40 NP shows a constant intensity level. Scale bar, 100 nm.

In the other cases, the PS40 NPs were observed to move into a pre-existing CCP region (type II, **Figure 7.7a-d**). As shown in **Figure 7.7a**, at the initial stage, the PS40 NP was randomly moving on the membrane, then co-localized with and remained within the CCP (**Figure 7.7c** and **d**). Finally, the signal of the CCP continuously decreased, indicating internalization of the CCP. After about 15 s, both the CCP and the PS40 NP had disappeared (**Figure 7.7c**), suggesting that the CCP had detached from the membrane (**Figure 7.7d**).

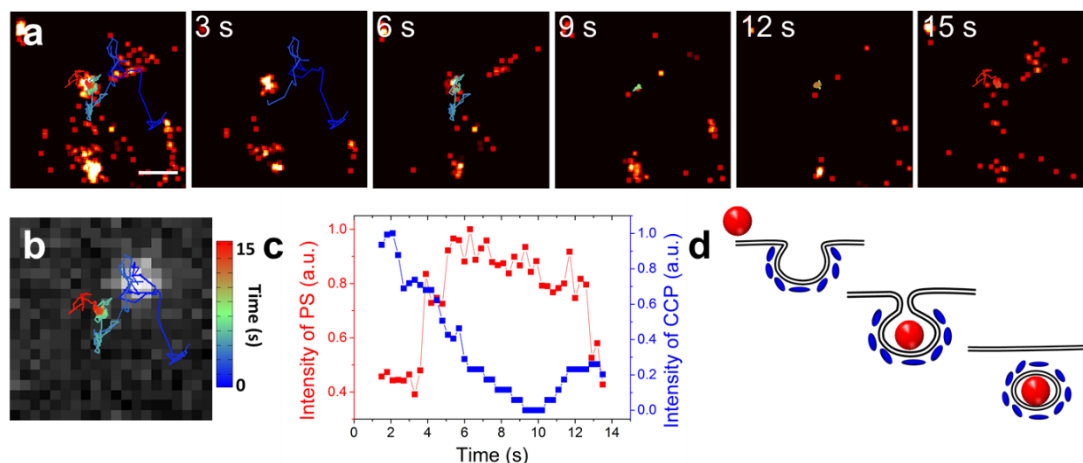


Figure 7.7 Type II PS40 NP and CCP co-localization. (a) Overlay of the PS40 NP trajectory and the CCP. (b) PS40 NP trajectory over raw data. (c) Emission intensities of the PS40 NP and the CCP during the uptake process. (d) Schematics of the sequential stages during type II endocytosis of PS40 NPs. Red: NP, blue: clathrin. Scale bar 500 nm. (d, courtesy of Karin Nienhaus.)

7.3 Co-localization of PS NPs with CCPs

7.3.1 Role of Clathrin in the Cellular Uptake of Carboxylated PS NPs

Studies have reported that carboxylated PS40 NPs are taken up by cells in a clathrin-dominated pathway¹⁶⁵. By using chlorpromazine, an inhibitor known to interfere with the CME pathways, we also observed an up to 40% decrease in the fluorescence of internalized PS40 NPs (**Figure 7.8a-c**), suggesting a significant role of clathrin in the endocytosis of these NPs by COS-7 cells. In contrast, treatment of COS-7 cells with chlorpromazine lead to almost no change in the uptake level of PS200 NPs (**Figure 7.8d-f**), probably due to the fact the PS200 are too big to be taken up through CCPs which normally have a diameter of less than 200 nm. We emphasize that, although the inhibition data do not give direct evidence on the specificity of NP-cellular interactions due to the toxicity of the inhibitor, the difference in the uptake of PS40 and PS200 NPs is indicative of the relative contribution made by CME pathway.

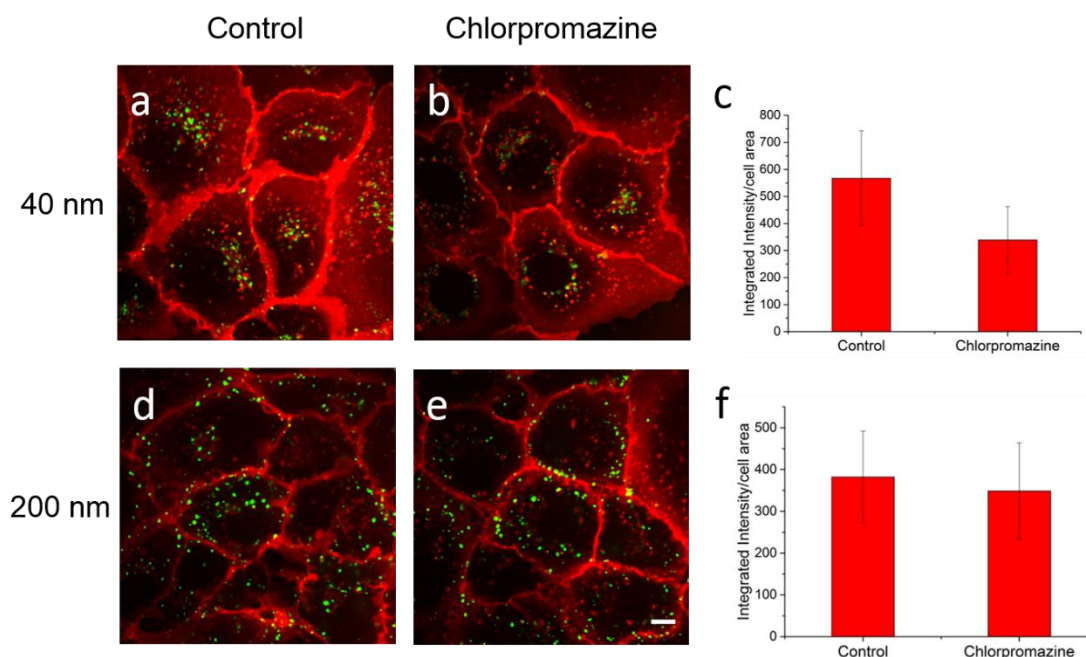


Figure 7.8 Effect of chlorpromazine on the uptake of PS40 and PS200 NPs by COS-7 cells. Spinning disk confocal images of COS-7 cells after 2 h incubation with 20 µg/ml (~1 nM) PS40 NPs, (a) without inhibitor (control) and, (b) with 10 µg/ml chlorpromazine. (c) Overall effect of chlorpromazine on the uptake of PS40 NPs, averaged over 32 cells, showing that the drug suppressed uptake by ~40%. Spinning disk confocal images after 2 h incubation with 20 µg/ml PS200 NPs, (d) without inhibitor (control) and, (e) with 10 µg/ml chlorpromazine. (f) Overall uptake of PS200 NPs, averaged over 25 cells. Within the error, there is no indication that internalization of PS200 NPs was affected by chlorpromazine. Scale bar, 10 µm.

7.3.2 Co-localization Probability

7.3.2.1 Co-localization of PS NPs and CCPs in simulated data

To determine the probability for an accidental co-localization of PS NPs and CCPs on the membrane, we used simulated data to evaluate this effect. Considering the density of PS NPs and CCPs on the membrane, 30 PS NPs and 100 CCPs were randomly distributed in an area of 30 µm × 30 µm (**Figure 7.9a**). The percentage of PS NPs co-localized with CCPs was determined as a function of the diameter of the CCPs (from 100 to 1000 nm, **Figure 7.9b**). If the distance between the PS NP and the center of the CCP was less than the radius of the CCP, the PS NP was counted as a co-localized particle. The percentage of PS NPs that were co-localized with CCPs depending on the width of the CCPs is shown in **Figure 7.9b**. For CCPs with widths less than 200 nm, only 0.2% of PS NPs are expected to co-localize with CCPs.

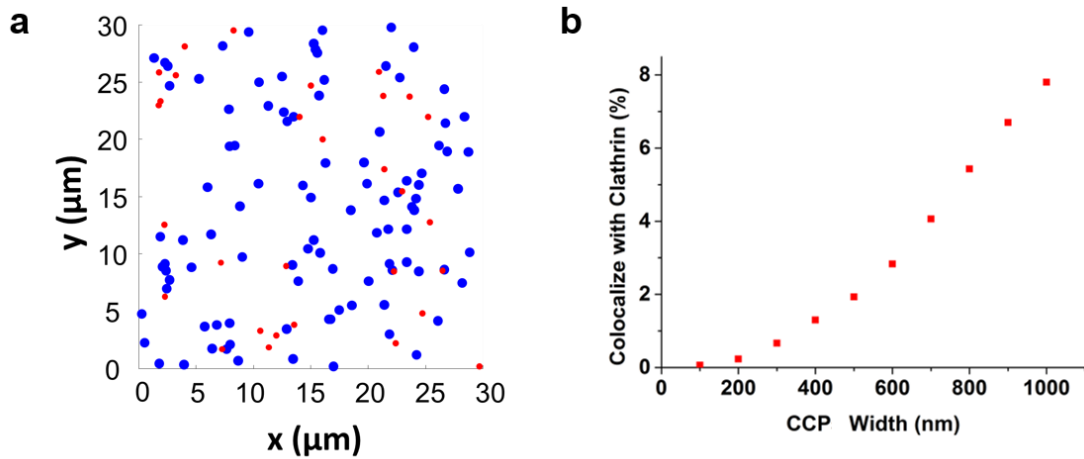


Figure 7.9 Simulation of random co-localization of PS NPs and CCPs. (a) 30 PS NPs and 100 CCPs were randomly deposited within a field of $30\ \mu\text{m} \times 30\ \mu\text{m}$. (b) Fraction of PS NPs co-localized with CCPs as a function of CCP diameter. For CCPs $<200\ \text{nm}$ in diameter, only 0.2% of PS NPs are expected to co-localize with CCPs.

7.3.2.2 Co-localization of PS NPs and Tf in COS-7 Cells

Next, we have evaluated the co-localization probability of Tf and CCPs. Tf is supposed to be exclusively internalized *via* CME. For the imaging of Tf, cells transfected by CLC-mEos2 were incubated in serum-free DMEM for 30 – 60 min at $37\ ^\circ\text{C}$. $1\ \mu\text{M}$ labeled Tf-Alexa647 was added *in situ*, left for 3 min and then washed with DMEM. The cells were kept in DMEM for imaging. The TIRF images of clathrin and Tf are shown in **Figure 7.10**.

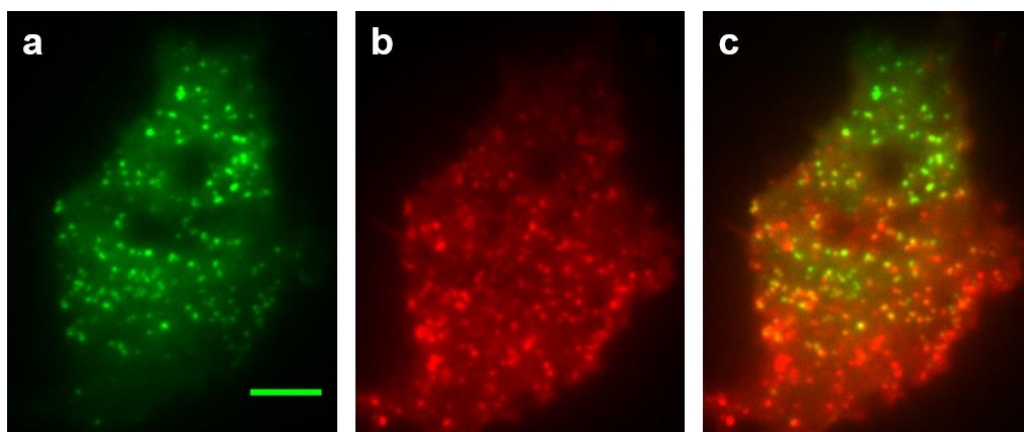


Figure 7.10 Dual-color TIRF image of a COS-7 cell expressing CLC-mEos2, exposed to fluorescently labeled Tf. (a) The green channel shows the punctate structure of CLC-mEos2 CCPs. (b) The red channel displays Tf labeled with Alexa647. (c) Overlay image, revealing colocalization of $\sim 35\%$ of the CCPs with Tf. Scale bar, $5\ \mu\text{m}$.

The ImageJ plugin JACoP was used to quantify the co-localization of CCPs and Tf. The object-based method was used. In order to segment the CCPs and the Tf objects from the fluorescent image, the background in the TIRF image (**Figure 7.11a**) was first subtracted using a rolling ball algorithm with a ball size of 2 pixels (**Figure 7.11b**). The objects with minimal size of 5 pixels were extracted from the background-subtracted image (**Figure 7.11c**). After object extraction, the percentage of Tf that co-localized with CCPs was calculated. The co-localization probability of Tf and CCPs was about 35% as shown in **Figure 7.12**.

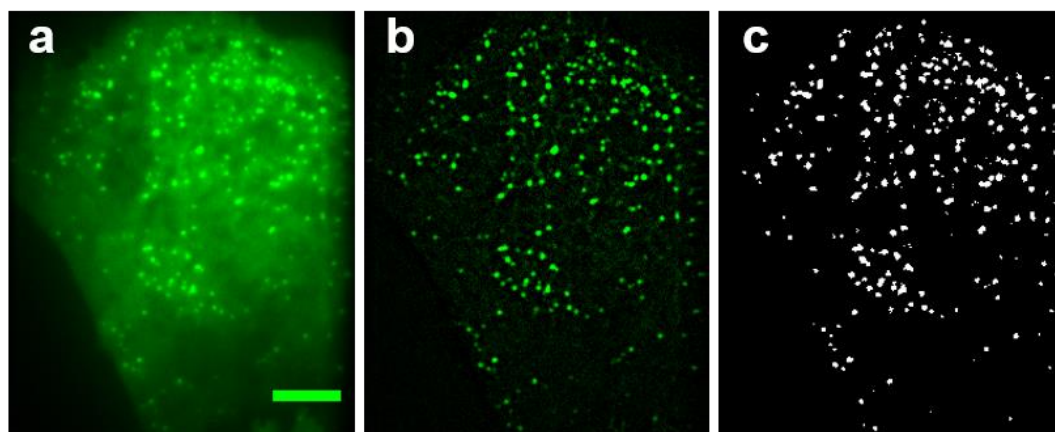


Figure 7.11 Object extraction from TIRF images of COS-7 cells using ImageJ. (a) TIRF image showing CCPs stained with CLC-mEos2; scale bar, 5 μm . (b) Image after background subtraction. (c) Objects (minimal size 5 pixels) were extracted from the background-subtracted image.

7.3.2.3 Co-localization of PS NPs and CCPs in COS-7 Cells

A variety of other NPs with different sizes and surface ligands were also investigated in this study. Carboxylated PS NPs with diameters of 20 nm and 200 nm (PS20 and PS200) were investigated. For unmodified, carboxylated PS20 (**Figure 7.12a**) and PS40 (**Figure 7.12b**) NPs, we found that $\sim 5\%$ of the PS NP trajectories were colocalized with the CCPs (**Figure 7.12f**), which is significantly higher than the simulated randomly distributed particles (0.2%, **Figure 7.9**). For cellular imaging of Tf, which is a ligand supposed to be exclusively internalized via CME, COS-7 cells were preincubated in serum free DMEM for 30 – 60 min at 37 $^{\circ}\text{C}$. 1 μM labeled Tf-Alexa647 was added *in situ* and left to incubate for 3 min. Then, the cells were thoroughly rinsed in DMEM for imaging. We found that $\sim 35\%$ of the molecules colocalized with CCPs (**Figure 7.12**). The relatively low percentage of colocalization is probably due to the fact that not all CME processes have been activated simultaneously in the short image acquisition time. In contrast, no CCP-related cellular internalization of PS200 NPs was found (**Figure 7.12d**), most probably because they are too large to be transported *via* this route. Indeed, treatment of COS-7 cells with chlorpromazine lead to almost no change in the uptake level of PS200, whereas the internalization of PS40 NPs was strongly decreased

(Figure 7.8). We then examined the cellular uptake of PS40 NPs upon modification with transferrin by either directly binding at the particle surface (PS40-Tf) or by coupling with a PEG linker in between (PS40-PEG(10k)-Tf. For PS40-Tf NPs, only 25% of the cells (3/12) were found to have NPs colocalized with CCPs (**Figure 7.12e** and **f**). On the contrary, for PS40-PEG(10k)-Tf NPs, over 70% of the cells (17/24) were found to have NPs colocalized with CCPs (**Figure 7.12c** and **f**). For bare PS40 and PS20 NPs, 55% (26/47) and 60% (26/43) of the cells were found to have NPs colocalized with CCPs, respectively. The median colocalization fraction (13%) is also higher than that of the bare PS NPs. Interestingly, a higher percentage of PS40-PEG(10k)-Tf NPs were found to go through Type II internalization (17%, **Figure 7.13**) compared to the bare PS40 NPs (8%) and PS20 NPs (9%).

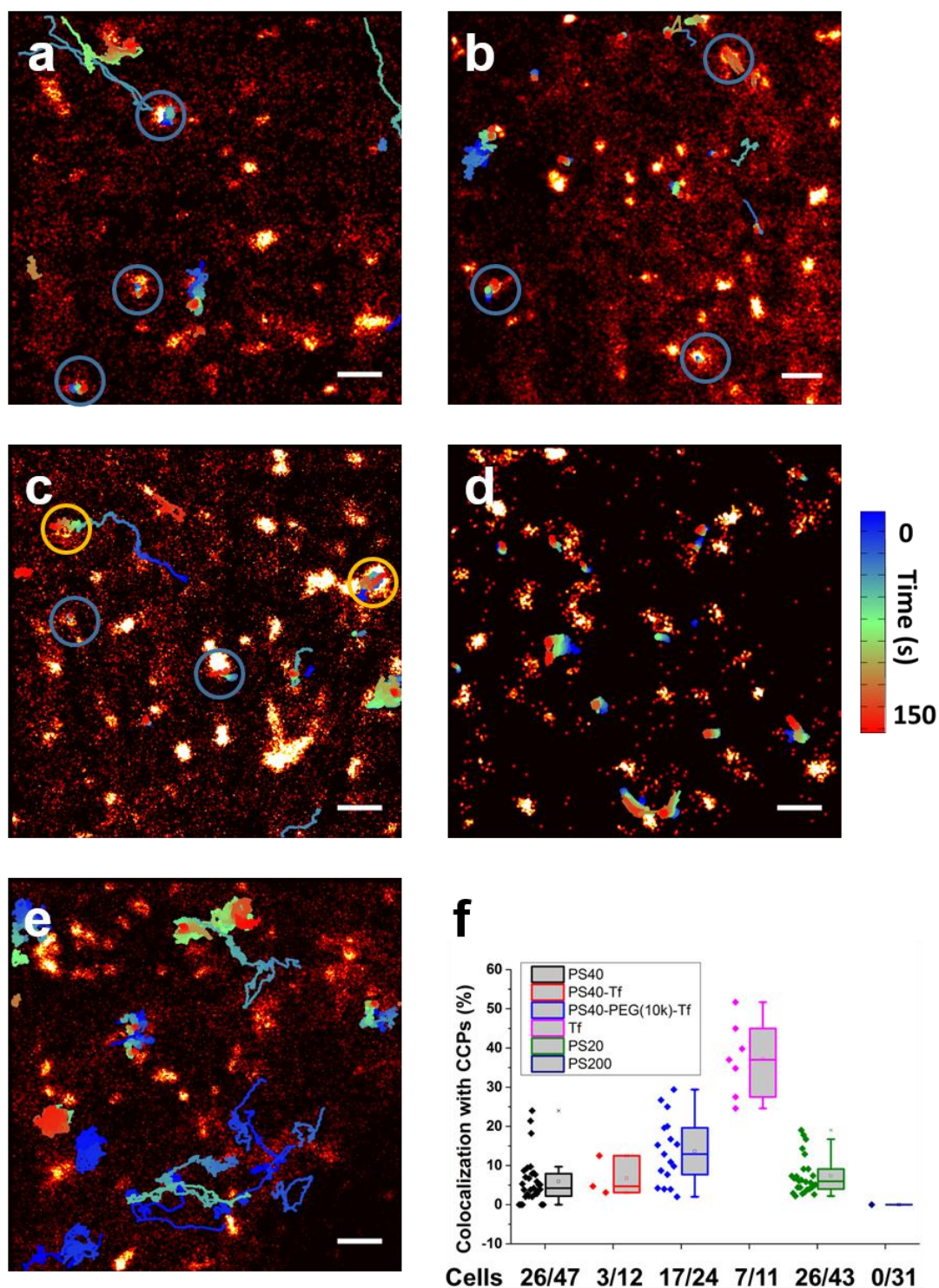


Figure 7.12 Percentage of different PS NPs and Tf co-localized with CCPs. (a) Overlay of PS20 NP trajectories and CCPs. (b) Overlay of PS40 NP trajectories and CCPs. (c) Overlay of PS40-PEG(10k)-Tf NP trajectories and CCPs. (d) Overlay of PS200 NP trajectories and CCPs. (e) Overlay of PS40-Tf NP trajectories and CCPs. (f) Percentage of different PS NPs and transferrin colocalized with CCPs. Blue and yellow circles indicate Type I and Type II events, respectively. Scale bars, 1 μm.

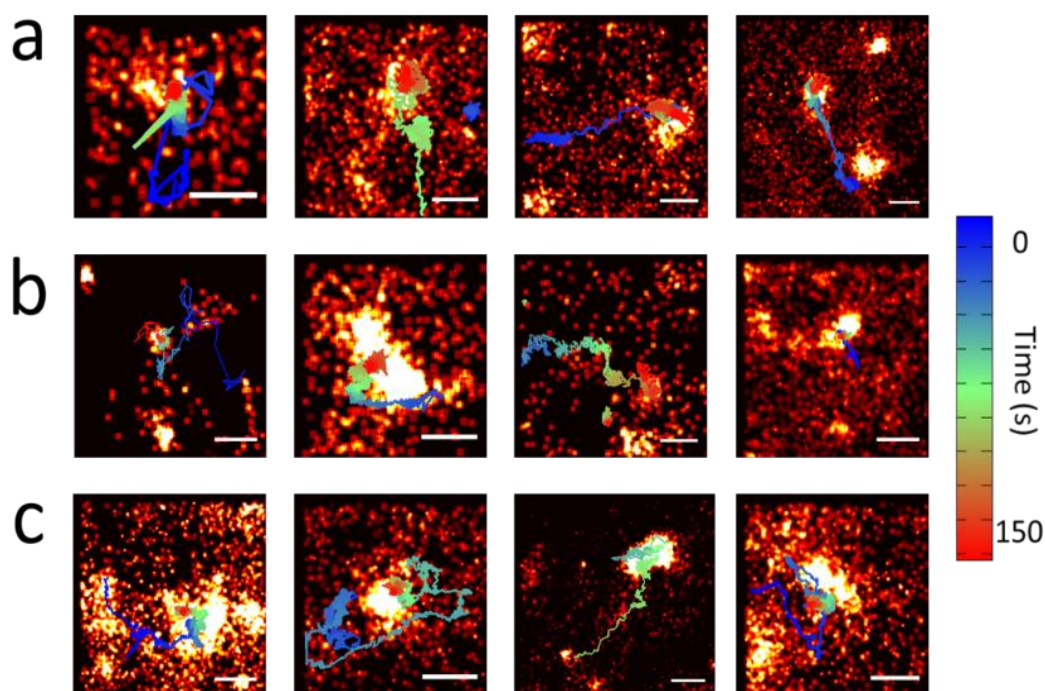


Figure 7.13 Dual-color image sequences showing examples of NPs colocalizing with CCPs in a type II encounter. Overlays of (a) PS20 NP, (b) PS40 NP, and (c) PS40-PEG(10k)-Tf NPs trajectories with CCP images. For PS20, PS40 and PS40-PEG(10k)-Tf NPs, 9% (5/58), 8% (5/63) and 17% (11/64) of all observed co-localization events are classified as type II encounters, respectively. Scale bars, 500 nm.

7.4 Mobility of PS NPs on the Membrane

7.4.1 MSS Analysis of the Mobility of Bare PS NPs on the Membrane

We have also quantified the mobility of the PS NPs on the cell membrane. The diffusion coefficient $D(t)$ at 1 s, D_0 , was used to measure the particle dynamics, and the slope of moment scaling spectrum (S_{MSS}) was used to determine the mode of movement¹⁴⁵. Three modes of motion could be distinguished (**Figure 7.14**): (i) confined diffusion ($D_0 < 2 \times 10^{-3} \mu\text{m}^2/\text{s}$, **Figure 7.14**, box 1); (ii) fast random diffusion with transient confinement ($D_0 > 2 \times 10^{-3} \mu\text{m}^2/\text{s}$, $S_{MSS} < 0.5$, **Figure 7.14**, box 2); (iii) directed movement ($S_{MSS} > 0.5$, **Figure 7.14**, box3). For bare PS NPs, most of the PS40 (62%, **Figure 7.14a**) and PS200 (59%, **Figure 7.14e**) NPs were found to be confined on the membrane while PS20 NPs were more mobile, with only 46% (**Figure 7.14d**) being confined. Interestingly, very different mobility of PS40-Tf and PS40-PEG(10k)-Tf NPs on the membrane was found. Most of the PS40-Tf NPs (72%, **Figure 7.14b**) were observed to diffuse fast on the membrane, with a mean D_0 of the transient confinement portion: $0.035 \pm 0.002 \mu\text{m}^2/\text{s}$ (standard error of mean, $n = 1441$) compared to the mean

D_0 of the transient confinement portion of PS40-PEG(10k)-Tf: $0.015 \pm 0.001 \mu\text{m}^2/\text{s}$ ($n = 1259$). Similar results were also observed in spinning disk confocal imaging of the top cell surface (**Figure 7.16** – **Figure 7.18**). These results show the low binding affinity of PS40-Tf on the membrane, which is probably the reason for the low uptake of PS40-Tf NPs by COS-7 cells and why very few PS40-Tf NPs were found to be colocalized with CCPs.

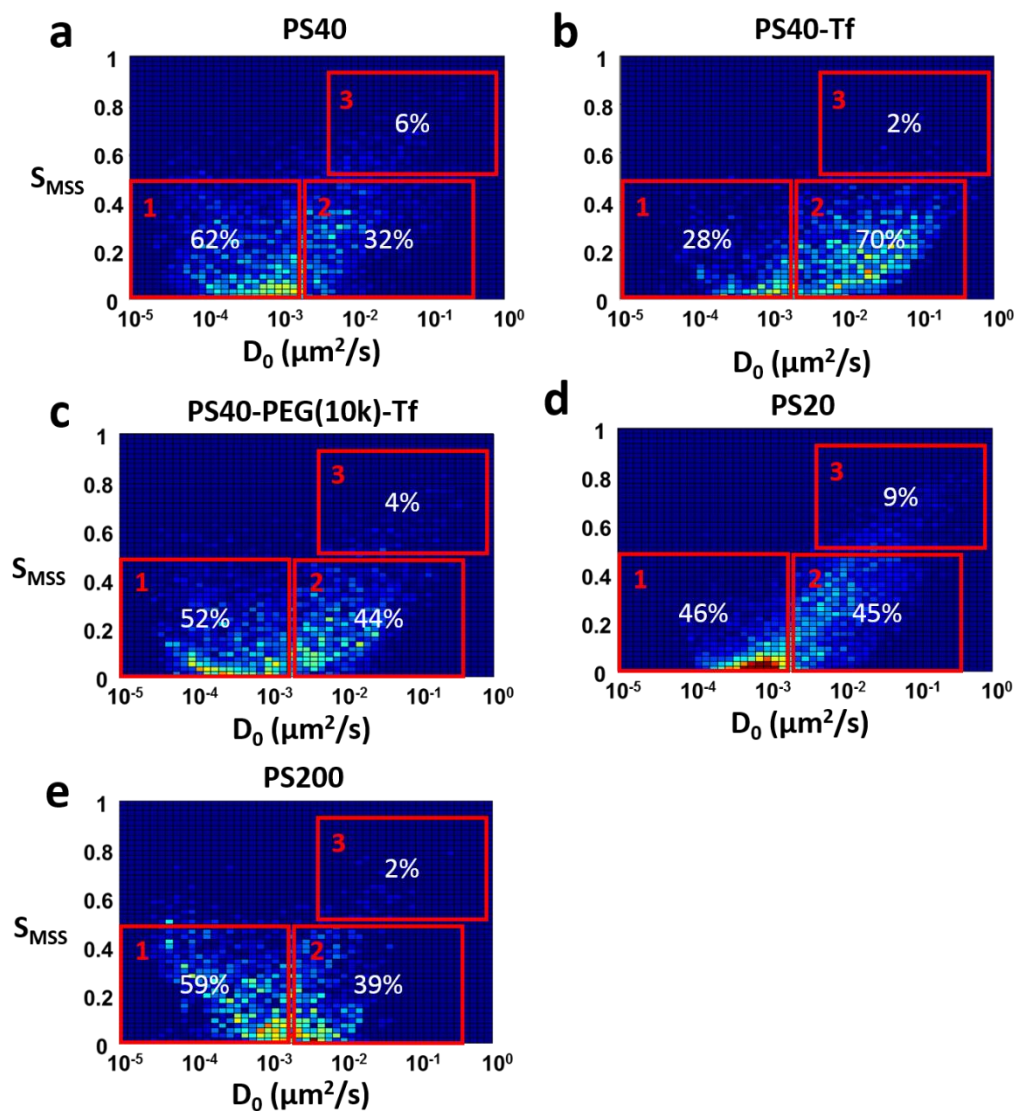


Figure 7.14 Comparison of S_{MSS} versus D_0 plots for different PS NPs on the COS-7 cell membrane. The three boxes highlight regions in the graph in which the PS NP motion is either confined (box 1), rapid with transient confinement (box 2) or directed (box 3). The S_{MSS} versus D_0 plots of different PS NPs show quite different mobility of these PS NPs on the membrane: PS40 NPs (**a**), PS40-Tf NPs (**b**), PS40-PEG(10k)-Tf NPs (**c**), PS20 NPs (**d**) and PS200 NPs (**e**).

7.4.2 Microscopic Diffusion Coefficients

Microscopic diffusion coefficients of individual tracks, denoted by D_{1-4} , were determined by linear fits to the MSD of the first four image frames, corresponding to an elapsed time of 120 ms in our data. For diffusion in compartmentalized space, D_{1-4} characterizes short-term diffusion within a compartment, whereas the long-term behavior is governed by the dynamics across many compartments. D_{1-4} is convenient because it can be determined independently of the motional modes¹⁶⁶. The center of the D_{1-4} distribution shifts to lower values with increasing size of the PS NPs; the centers of the D_{1-4} distributions are $4.8 \times 10^{-3} \mu\text{m}^2/\text{s}$, $1.3 \times 10^{-3} \mu\text{m}^2/\text{s}$ and $0.8 \times 10^{-3} \mu\text{m}^2/\text{s}$ for PS20, PS40 and PS200, respectively (**Figure 7.15**). For PS40-PEG(10k)-Tf NPs, two populations of D_{1-4} were found, with center positions at $0.7 \times 10^{-3} \mu\text{m}^2/\text{s}$ and $1.8 \times 10^{-2} \mu\text{m}^2/\text{s}$. Likewise, for PS40-Tf NPs, two populations were found, with center populations at $0.5 \times 10^{-2} \mu\text{m}^2/\text{s}$ and $0.8 \times 10^{-1} \mu\text{m}^2/\text{s}$, respectively.

Since the PS NPs have an additional searching process in Type II events, PS NPs with higher mobility on the membrane are likely to have higher probability to find a CCP on the membrane. Compared to bare PS40 NPs, PS40-PEG(10k)-Tf NPs have a more mobile population on the membrane which may indicate that it has more Type II events than bare PS40 NPs. However, this is not the case for PS20 NPs. Even though PS20 NPs are also more mobile than PS40 NPs, the percentage of Type II events did not increase. The role of the ligand should also play an important role in the random walk search on the membrane to find a suitable entrance site⁶. These pieces of information could shed some light on the optimal NPs design for target molecules which requires both a suitable mobility of NPs on the membrane and the conjugated ligand.

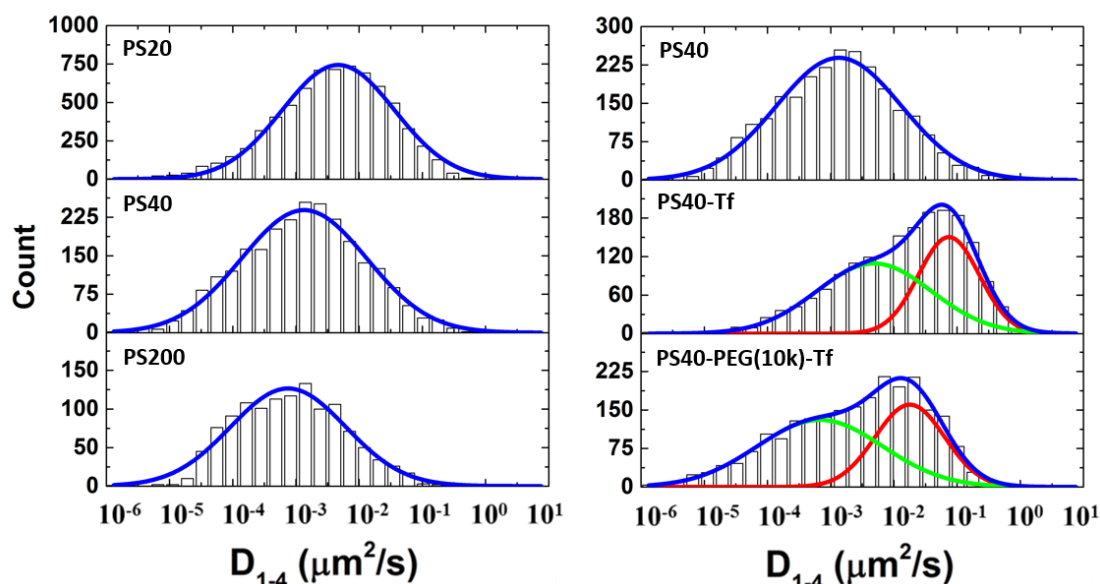


Figure 7.15 Distribution of microscopic diffusion coefficient D_{1-4} of different PS NPs.

7.5 Spinning Disk Confocal Imaging

COS-7 cells were first incubated with 0.5 $\mu\text{g/ml}$ Hoechst 33342 nucleic acid stain in serum free DMEM for 30 min. Afterwards, membranes were stained with 0.25 $\mu\text{g/ml}$ CellMaskTM Orange (Invitrogen) in DMEM for 5 min and washed twice with PBS. After adding the same amount of PS40 NPs as for TIRF imaging (0.5 nM), live cell imaging was performed for 1 h at 2 s intervals by using an Andor Revolution[®] XD spinning disk laser scanning microscope (BFI OPTiLas, München, Germany) with alternating excitation.

For spinning disk confocal imaging, relatively low laser power was used compared to the laser power used for localization microscopy and longer image acquisition (2 h) was applied. Since COS-7 cells are relatively flat, individual PS40 NPs could be observed on the top membrane surface (**Figure 7.16a**). Interestingly, after summing up all the images acquired in 1 h, a lot of spots were still clearly resolved on the membrane (**Figure 7.16b**). In comparison, fast moving particles in the medium (arrows, **Figure 7.16a**) were not visible on the membrane in the summed image (arrows, **Figure 7.16b**). It indicates that the PS40 NPs were immobilized during imaging. The zoomed image in **Figure 7.16c** further confirms this assumption. A lot of PS40 NPs could be observed over a long time period. The motion of the PS40 NPs on the top membrane surface was very similar to that of the PS40 NPs on the basal membrane. Therefore, the PS40 NPs appear to be strongly bound to the membrane, and they are confined in a small region. This may be due to a membrane skeleton “fence” or “corral”^{167,168} formed by cortical actin. The cytosolic surface of the plasma membrane is partitioned into many grids. The actin filaments restrict the inter-compartment movement.

For PS40-PEG(10k)-Tf NPs, the trajectories of the NPs during the 2 h image acquisition time were plotted onto the initial raw particle image (**Figure 7.17**). Only trajectories longer than 5 min were kept. As shown in **Figure 7.17b**, many particles can be tracked for a very long time which means that the particles stayed on the membrane for long time periods. In contrast, no trajectories were found for PS40-Tf NPs on the membrane. If we sum up all image frames taken over the 2 h, almost no individual spots could be identified (**Figure 7.18b**). Almost no PS40-Tf NPs were found to be bound on the membrane which confirms the view from the SPT data that most of PS40-Tf NPs were not confined on the membrane.

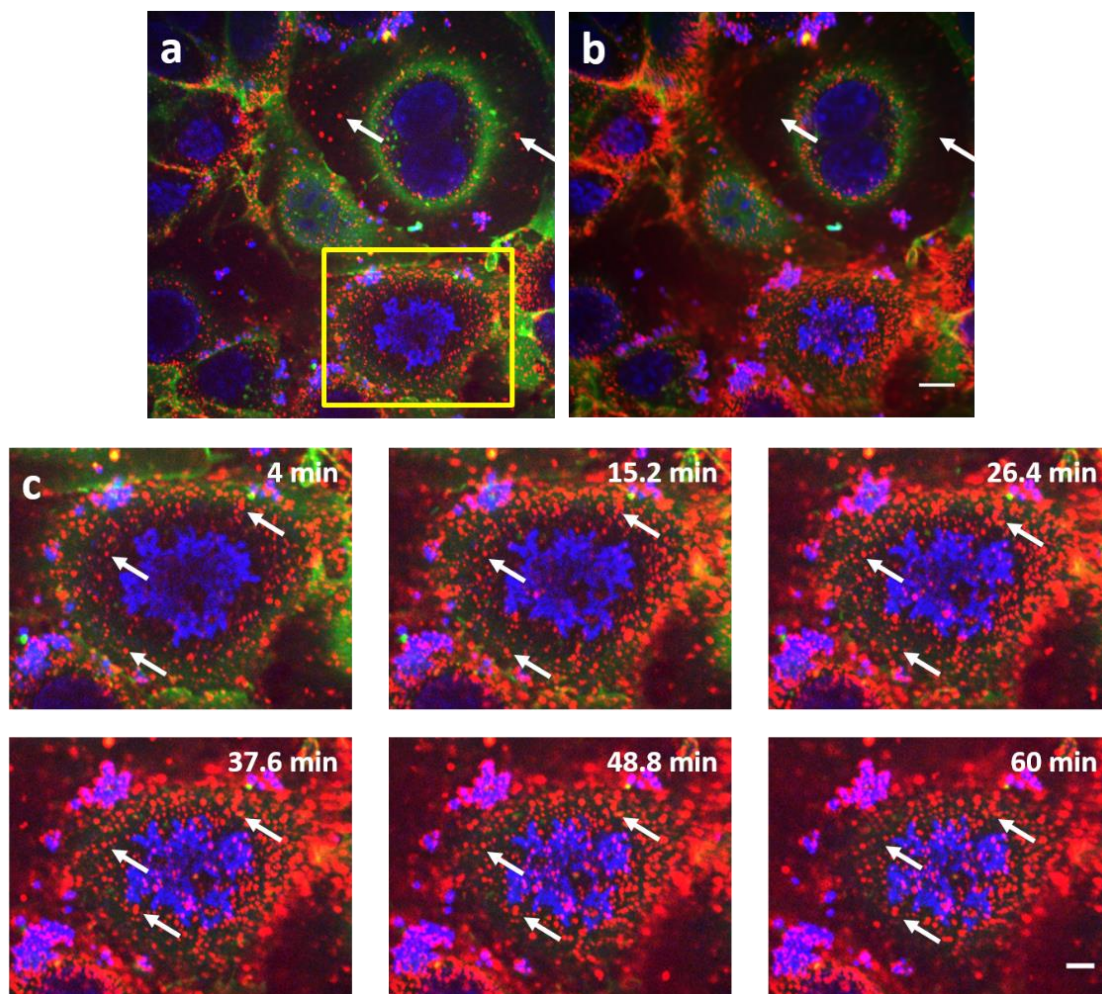


Figure 7.16 Multi-color spinning disk confocal images of COS-7 cells exposed to PS40 NPs, taken in three color channels. Blue: nucleus; green: membrane; red: PS40 NPs. (a) Single confocal image scanned across the top membrane of the cell marked by the yellow frame. (b) Integrated image of all confocal frames collected during 1 h; scale bar, 10 μm . The two arrows mark locations where NPs identified in panel (a) have disappeared in panel (b), indicating that these are fast diffusing NPs in the cell medium. By contrast, many spots on the plasma membrane of the marked cell in the first image (panel (a)) are still visible in the integrated image, indicating their low mobility. (c) Temporal evolution of the marked region of panel (a). Many PS40 NPs can be tracked for a long time period, similar to what was observed for the basal membrane. They are confined to small membrane regions, likely due to a “fence” or “corral” formed by cortical actin that restricts their long-range diffusion.

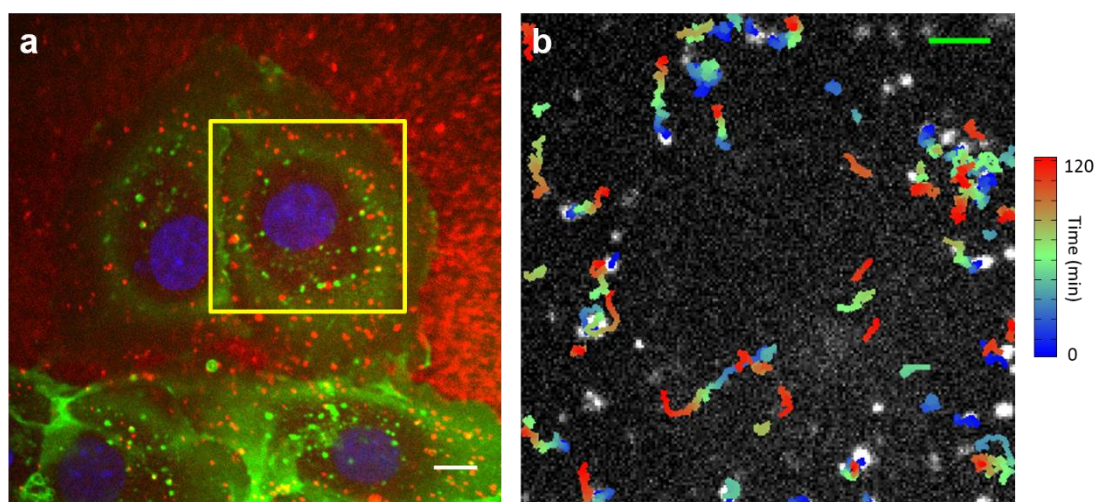


Figure 7.17 Multi-color spinning disk confocal imaging of PS40-PEG(10k)-Tf NPs on COS-7 cells. Blue: nucleus; green: membrane; red: PS40 NPs. (a) Confocal image of PS40-PEG(10k)-Tf NPs on the top cell surface; scale bar 10 μm . (b) NP trajectories longer than 5 min in the region marked by the yellow frame in panel (a) over 2 h; scale bar, 5 μm .

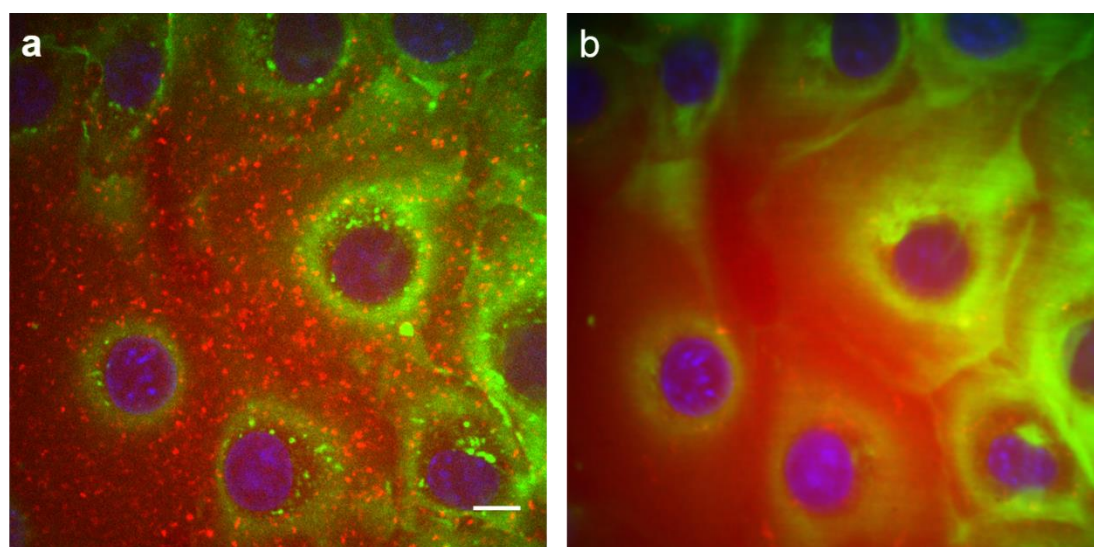


Figure 7.18 Multi-color spinning disk confocal imaging of PS40-Tf NPs on COS-7 cells. Blue: nucleus; green: membrane; red: PS40 NPs. (a) Confocal image of PS40-Tf NPs scanned across the top cell surface, showing NPs as punctate structures; scale bar, 10 μm . (b) Integrated image of all confocal frames taken over 2 h. Unlike in panel (a), resident spots are essentially absent, indicating that these NPs are not immobilized by tightly adhering to the membrane, which is in agreement with the observations made by single particle tracking.

7.6 Size of CCPs

Finally, we investigated the size of the CCPs that co-localized with PS NPs and those that did not co-localize. It has been reported that the size of CCPs is affected by the size of the cargoes²⁹. Association of CCPs with larger cargoes was supposed to build a larger clathrin lattice. With the super-resolved PALM image, we could directly measure the size of the CCPs that were loaded with PS NPs (**Figure 7.19**). An appropriate bin time window is critical for size measurements from the PALM image. The size distribution of the CCPs determined from 30 s snapshots was similar to those determined from both 15 s snapshots and 7.5 s snapshots, which is consistent with previous results¹³¹(**Figure 7.20**). Shorter time bins reduce the effect of CCP movement during data acquisition, however, the size of the CCPs also varies during the whole lifetime¹⁶². Therefore, non-matured CCPs are measured more often within a short time window. Compared with the 30 s snapshot, the 45 s snapshot has more CCPs with sizes >200 nm, which is probably due to the effect of movement of CCPs during the long time data acquisition. Therefore, a time bin of 30 s was used for measuring the size of the CCPs. As shown in **Figure 7.19**, the mean size of the non-overlapped CCPs was 150 nm. However, for the CCPs that colocalized with PS20, PS40 and PS40-PEG(10k)-Tf NPs, a significant increase of about 30 – 40 nm was found. No significant size change was found for CCPs that colocalized with PS20, PS40 and PS40-PEG(10k)-Tf NPs. Our observations provide direct evidence that cargo loading is related to the size of CCPs.

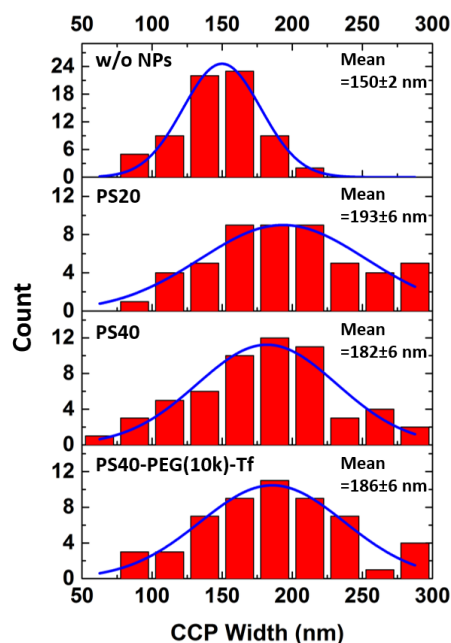


Figure 7.19 Measured size distributions of CCPs with and without loaded PS NPs. To measure the size of each CCP, localization density profiles along the short axis within a 60-nm wide stripe at the center of CCPs were obtained and fitted with a Gaussian to obtain the full-width half maximum (FWHM). The FWHM of many individual CCPs is shown.

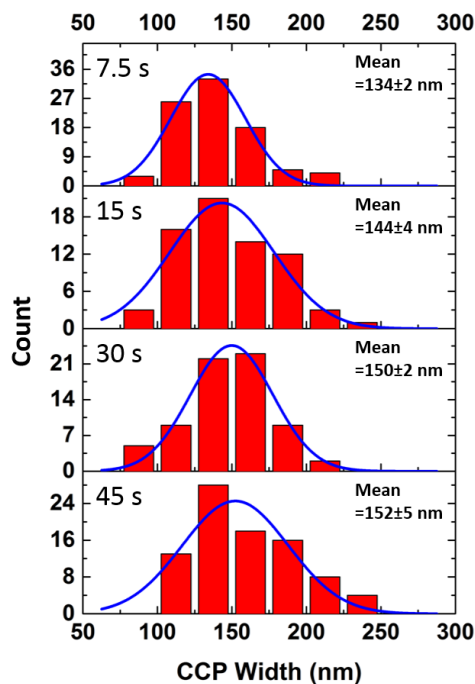


Figure 7.20 Measured size distributions of CCPs obtained from PALM images by using different time bins.

7.7 Summary

In summary, we have demonstrated that, by combining SPT and PALM, one could directly observe the fast dynamics of NPs during endocytosis, with both high spatial and temporal resolution. This has allowed us to visualize endocytic mechanisms of PS NPs without using inhibitors to block specific endocytic pathways. In combination with the PALM image, the detailed analysis of the co-localized CCP trajectories shows very heterogeneous diffusion during the interaction of PS NPs and CCPs, indicating a strong interaction between the CCPs and the sub-membrane cytoskeleton during endocytosis. With the unique advantage of imaging with both high spatial and temporal resolution, we identified two different types of NP-CCP interaction modes. In most cases, CCPs form *in situ* around NPs to trigger endocytosis. NPs with different size and ligand conjugation were also investigated. PS200 NPs were not internalized through CCPs while PS20 and PS40 NPs were internalized through CCPs. By conjugation of Tf through a PEG linker on the PS NP surface, the percentage of PS NPs taken up through CME is increased. Although the current study focused on the clathrin-involved endocytosis pathway, one can easily extend this strategy to study other essential aspects of NP-cell interactions, such as the exocytosis of NPs, role of the cytoskeleton in NP transport and caveolae-involved endocytosis mechanism.

Chapter 8

Summary

Recently, the resolution limit of far-field optical microscopy methods has been overcome by a couple of techniques. Among these approaches, single molecule localization microscopy is an emerging multidisciplinary field that has opened up new opportunities to study cellular events at the nanometer scale. The main principle of this new imaging modality is the sparse activation of fluorophore molecules at different times. Individual molecular patterns are then identified and fitted with a model function, enabling precise estimation of the fluorophore locations. Unlike conventional fluorescence microscopy images, the raw data of these sparse patterns cannot be visualized directly. Instead, an additional data processing step is needed to generate the final image.

In this work, we have presented a fast and efficient molecule detection algorithm for localization microscopy. With the development of GPU based molecule localization algorithms, molecule localization requires less than 10% of the overall analysis process. Molecule detection is currently the limiting factor of the analyzing software regarding both speed and detection efficiency aspects. The bottleneck of the analysis software lies on fast molecule detection while maintaining minimum detection errors. Therefore, most of my work focused on molecule detection. Instead of the basic thresholding approach based on the SNR of each pixel, we used the null hypothesis that a pixel belongs to the local background by computing the P -value for each pixel under the assumption that it is drawn from a normal distribution. There are two advantages of this method: 1) the calculation of the P value can be parallelized which enables real time computation of the data; 2) the P -value map is insensitive to the changes of the SNR and significantly enhances signal contrast without introducing noise peaks, which enables efficient molecule detection. For a typical image size of 512×512 pixels, acquired by the electron-multiplying charge-coupled device (EMCCD) camera, the processing time is 15 – 30 ms per image, depending on its complexity. The speed is comparable to the maximum full frame rate of current EMCCD cameras and, therefore, allows real-time data processing. Comparison of our newly developed algorithm a-livePALM with other state-of-the-art algorithms demonstrates that a-livePALM achieves efficient molecule detection without sacrificing analysis speed. This advanced software development enables a statically analysis of large data sets recorded in PALM experiments.

We have also implemented 3D astigmatism super-resolution imaging by introducing a cylindrical lens in the emission pathway. Using bright fluorescent beads, the localization accuracy was $\sim 5 - 7$ nm near the focal plane (< 200 nm) and $\sim 8 - 13$ nm further away from the focal plane (400 – 600 nm). Application of this technique to image microtubules and CCPs demonstrates the ability of resolving nanoscopic structures in living cells using localization microscopy. With the microtubules immunostained by Alexa647, the reconstructed FWHM of the tubule bundle was ~ 54 nm in the lateral direction and ~ 90 nm in the axial direction while the FWHM observed by TIRF microscopy was ~ 400 nm in the lateral direction. We have also implemented this technique to image CLC-mEos2 in living COS-7 cells. By optimization of the experimental conditions (*i.e.*, image acquisition time, suitable fluorescent probes), CCPs which appeared as punctuate structures in a TIRF image showed as ring-like structures in the PALM image. These proof-of-principle experiments demonstrate the improved spatial resolution by localization microscopy.

Mapping the interaction between NPs and cells requires both high spatial and temporal resolution. However, the basic principle of localization microscopy, which requires enough individual molecules to reconstruct a super-resolution structure limits the temporal resolution of this technique. We have demonstrated that, by combining SPT and PALM, one could directly observe the interaction between NPs and receptors on the cell membrane with high spatial and temporal resolution. This has allowed us to visualize the endocytic uptake of PS NPs without using inhibitors to block specific endocytic pathways. The detailed analysis of trajectories that co-localized with CCPs showed very heterogeneous diffusion during the interaction of PS NPs and CCPs, indicating the strong interaction between the CCPs and the sub-membrane cytoskeleton during endocytosis. With the unique advantage of imaging with both high spatial and temporal resolution, we have identified two different types of NP-CCP interaction modes, where in most cases CCPs form *in situ* around NPs to trigger endocytosis. NPs with different size and ligand conjugation were also investigated. PS20 and PS40 NPs were internalized through CCPs while PS 200 NPs were not internalized through CCPs. By conjugation of Tf through a PEG linker on the PS40 NP surface, the percentage of PS40 NPs taken up through CME was increased.

MSS analysis was applied to elucidate the relation between diffusion coefficient and motion type of PS NPs (confined, transiently confined and directed movement). Most of the bare PS40 (62%) and PS200 (59%) NPs were found to be confined on the membrane while bare PS20 NPs showed more mobility, with only 46% being confined. They are confined to small membrane regions, likely due to a “fence” or “corral” formed by cortical actin that restricts their long-range diffusion. Interestingly, very different mobilities were found for PS40-Tf and PS40-PEG(10k)-Tf NPs on the membrane. Most of the PS40-Tf NPs (72%) were observed to diffuse fast on the membrane, with a mean D_0 of the transient confinement portion: $0.035 \pm 0.002 \mu\text{m}^2/\text{s}$

compared to the mean D_0 of the transiently confined portion of PS40-PEG(10k)-Tf: $0.015 \pm 0.001 \mu\text{m}^2/\text{s}$. Spinning disk confocal imaging also confirmed these observations on the top cell surface. Weaker binding of PS40-Tf NPs on the membrane also inhibits the efficient uptake of these NPs. We therefore emphasize the importance of NP binding to the membrane, since in most cases, CCPs form *in situ* around NPs to trigger endocytosis. Any conjugation of ligands on NPs should be well characterized because the binding affinity of NPs on the membrane may change after modification.

Though we limited this method to the interaction between NPs and cell membrane receptors, we envision a great potential of applying the present approach for exploring a wide range of biological events at the molecular level, with the unique advantage of featuring both high spatial and temporal resolution.

Zusammenfassung

Innerhalb der letzten Jahre konnte mit Hilfe neuartiger Techniken das limitierte Auflösungsvermögen der konventionellen Weitfeldmikroskopie überwunden werden. Eine dieser Methoden ist die Lokalisationsmikroskopie (*photoactivation localization microscopy*, PALM), ein multidisziplinäres Forschungsgebiet, welches neue Möglichkeiten eröffnet, um zelluläre Prozesse auf der Nanometerskala zu untersuchen. Das Grundprinzip dieses bildgebenden Verfahrens beruht auf der zufälligen Aktivierung einiger weniger Fluorophore innerhalb eines Ensembles zu unterschiedlichen Zeitpunkten. Diese können anhand ihrer Fluoreszenz identifiziert und mit Hilfe einer Modellfunktion präzise lokalisiert werden. Dieser Vorgang wird so lange wiederholt, bis alle Fluorophore registriert sind. Anders als bei Bildern gängiger Fluoreszenzmikroskope muss dann zusätzlich ein Datenaufbereitungsschritt eingefügt werden, um aus den vielen Einzelbildern das endgültige Bild zu erzeugen.

Im Rahmen dieser Arbeit wurde ein schneller und zudem effizienter Algorithmus zur Moleküldetektion und -lokalisierung entwickelt, den wir a-livePALM genannt haben. Die Moleküldetektion ist zurzeit der limitierende Faktor im Hinblick auf die Geschwindigkeit und Effizienz der Datenanalyse. Den eigentlichen Engpass bildet die schnelle und gleichzeitig möglichst fehlerfreie Moleküldetektion. Durch die Entwicklung eines GPU-basierten Moleküldetektionsalgorithmus konnte die Gesamtrechenzeit für diesen Schritt auf weniger als 10% der gesamten Prozessdauer reduziert werden. Anstatt einer simplen, auf dem Signal-Rausch-Verhältnis jedes Pixels basierenden Schwellenwertanalyse wurde die Nullhypothese angewandt, um jedem Pixel einen lokalen Hintergrund zuzuordnen. Dazu wurde der P -Wert für jeden Pixel berechnet, und zwar unter der Annahme, dass der P -Wert mit Hilfe einer Normalverteilung gewonnen werden kann. Diese Methode hat zwei Vorteile: 1.) Die Berechnung des P -wertes für die einzelnen Pixel kann parallel durchgeführt werden, was eine Analyse der Daten in Echtzeit ermöglicht; 2.) Die P -Wert-Karte ist unempfindlich gegenüber Unterschieden im Signal-Rausch-Verhältnis und erhöht den Kontrast erheblich, ohne durch Rauschen verursachte Peaks einzubringen, was eine effiziente Moleküldetektion ermöglicht. Für ein typisches Bild mit einer Größe von 512×512 Pixeln, das mit einer mit einer *electron-multiplying charge-coupled device* Kamera (EMCCD-Kamera) aufgenommen wurde, betrug die Verarbeitungszeit, abhängig von der Komplexität des Bildes, 15 – 30 ms. Diese Geschwindigkeit ist vergleichbar mit der maximalen Bildrate von aktuellen EMCCD-Kameras und erlaubt

daher eine Echtzeit-Analyse der Daten. Der Vergleich unseres neuentwickelten a-livePALM-Algorithmus mit anderen modernen Algorithmen zeigte, dass a-livePALM eine effiziente Moleküldetektion ermöglicht, ohne dabei Geschwindigkeit zu opfern. Diese hochentwickelte Software ermöglicht somit eine statistische Analyse von großen Datensätzen, die in PALM-Experimenten gemessen wurden.

Zusätzlich wurde durch den Einbau einer Zylinderlinse in den Emissionspfad des Mikroskops ein Astigmatismus-basiertes hochauflösendes Bildgebungsverfahren in 3D implementiert. Unter Verwendung heller fluoreszierender Partikel konnte eine Lokalisationsgenauigkeit von $\sim 5 - 7$ nm im Bereich der Brennebene (Abstand < 200 nm) und $\sim 8 - 13$ nm außerhalb der Brennebene (Abstand 400 nm – 600 nm) erreicht werden. Die Anwendung dieser Technik in der Bildgebung von Mikrotubuli und sogenannten *Clathrin-coated-Pits* (CCPs) zeigte die Fähigkeit der Lokalisationsmikroskopie, nanoskopische Zellstrukturen aufzulösen. Für mit Alexa647 immunhistochemisch gefärbte Mikrotubuli konnte eine Durchmesser (FWHM) der Protofilamente von ~ 54 nm in lateraler Richtung und ~ 90 nm in axialer Richtung bestimmt werden. Im Vergleich dazu konnte durch konventionelle Totalreflexionsfluoreszenzmikroskopie (TIRFM) lateral nur eine Halbwertsbreite von ~ 400 nm erreicht werden. Weiterhin wurde diese Methode verwendet, um die *Clathrin-light-chain* (CLC)-mEos2 Fusion in lebenden COS-7-Zellen abzubilden. Durch die Optimierung der experimentellen Bedingungen (Bildaufnahmezeit, geeignete Fluorophore *etc.*) konnten die CCPs, welche durch TIRFM nur punktförmig wiedergegeben wurden, durch PALM als ringförmige Strukturen abgebildet werden. Diese Experimente erbrachten den Grundsatzbeweis dafür, dass durch Lokalisationsmikroskopie eine verbesserte räumliche Auflösung erreicht wird.

Um die Wechselwirkung zwischen Nanopartikeln (NPs) und lebenden Zellen zu beobachten, ist sowohl eine hohe räumliche als auch eine hohe zeitliche Auflösung erforderlich. Das Prinzip der Lokalisationsmikroskopie erfordert jedoch die Detektion einer ausreichenden Anzahl an Photonen, um im Anschluss eine Struktur mit einer Auflösung unterhalb des Beugungslimits rekonstruieren zu können, weshalb diese Technik nur eine sehr begrenzte Zeitauflösung aufweist. Daher haben wir PALM (zur Bildgebung der CCPs) mit *Single Particle Tracking* (SPT, zur Beobachtung der NP Diffusion) kombiniert. Dadurch wurde es möglich, die Aufnahme von Polystyrol (PS) NPs durch Endozytose in Echtzeit zu beobachten, ohne zuvor bestimmte Mechanismen der Endozytose durch Verwendung spezieller Inhibitoren zu unterdrücken. Die genaue Analyse von Trajektorien der NPs, die eine Kollokalisierung mit CCPs aufwiesen, zeigte ein sehr heterogenes Diffusionsverhalten. Dies wies auf eine starke Interaktion zwischen den CCPs und dem sub-membranen Zytoskelett während der Endozytose hin. Mit dieser einmaligen Möglichkeit der Bildgebung mit sowohl hoher zeitlicher als auch räumlicher Auflösung konnten zwei verschiedene Arten der NP-CCP Interaktion identifiziert werden, wobei sich in den meisten Fällen CCPs *in situ* um die NPs bildeten,

um somit die Endozytose auszulösen. Des Weiteren wurde die zelluläre Aufnahme von NPs verschiedener Größe und Oberflächenfunktionalisierung verglichen. 20-nm und 40-nm PS NPs wurden hierbei durch CCPs internalisiert, während 200-nm PS NPs nicht durch CCPs internalisiert wurden. Durch die Bindung von Transferrin über einem PEG-Linker an die Oberfläche von 40-nm PS NPs wurde der Prozentsatz der NPs, der durch Clathrin-vermittelten Endozytose internalisiert wurde, erhöht.

Mit Hilfe einer ‚*Moment Scaling Spectrum*‘ (MSS) Analyse wurde der Zusammenhang zwischen Diffusionskoeffizient und Art der Bewegung (beschränkt, vorübergehend beschränkt, gerichtete Bewegung) genauer untersucht. Die Bewegung der meisten 40-nm PS NPs (62%) und 200-nm PS NPs (59%) auf der Zellmembran war beschränkt, während die 20-nm PS NPs mobiler waren und nur zu 46% eine beschränkte Diffusion aufwiesen. Diffusion über größere Strecken wurde vermutlich durch die Bildung von „fence“ oder „corral“ Strukturen des kortikalen Aktins unterbunden. Interessanterweise zeigten die mit Transferrin funktionalisierten 40-nm PS NPs, je nach Art der Anbindung, sehr unterschiedliche Mobilität. Die meisten der direkt mit Transferrin bedeckten 40-nm PS NPs (72%) zeigten eine schnelle Diffusion auf der Membran mit einem mittleren Diffusionskoeffizienten $D_0 = 0.035 \pm 0.002 \mu\text{m}^2/\text{s}$. Wurde das Transferrin über einen Linker an die Oberfläche gekoppelt, war der Diffusionskoeffizient deutlich kleiner, $D_0 = 0.015 \pm 0.001 \mu\text{m}^2/\text{s}$ (Werte für NPs mit vorübergehend beschränkter Bewegung). Diese Beobachtungen konnten durch Bildgebung mit einem Spinning-Disk-Mikroskop auch für die Membran an der Oberseite der Zelle bestätigt werden. Die schwächere Bindung der mit Transferrin funktionalisierten 40-nm PS NPs an die Membran hemmte auch die effektive Aufnahme der NPs in die Zelle. Deshalb muss an dieser Stelle noch einmal die Bedeutung der Bindung der NPs an die Membran betont werden, da sich die CCPs in den meisten Fällen *in situ* um gebundene NPs bilden und so die Endozytose auslösen. Da die Bindungsaffinität der NPs an die Membran auch von der Art der Oberflächenfunktionalisierung abhängt, sollte diese gut charakterisiert werden.

Auch wenn die Methode hier nur zur Untersuchung der Interaktion zwischen NPs und Zellmembranrezeptoren verwendet wurde, hat sie großes Potential in der Erforschung von einer Vielzahl von biologischen Prozessen auf molekularer Ebene mit dem einzigartigen Vorteil einer gleichzeitig hohen räumlichen und zeitlichen Auflösung.

Acronyms

APD	avalanche photodiode
AP	adaptor protein
ADC	analog-to-digital converter
β ME	β -mercaptoethanol
CCP	clathrin coated pit
CCV	clathrin coated vesicles
CDF	cumulative distribution function
CIC	clock induced charge
CME	clathrin-mediated endocytosis
CLC	clathrin light chain
CLIC	clathrin-independent carrier
CPU	central processing unit
CRLB	Crámer-Rao lower bound
DMEM	Dulbecco's modified Eagle's medium
dSTORM	direct stochastic optical reconstruction microscopy
EM	electron-multiplying
EMCCD	electron multiplying charge-coupled device
FWHM	full width half maximum
GFP	green fluorescent protein
GPU	graphic processing unit
GSDIM	ground state depletion and individual molecule return
LWM	local weighted mean
MEA	mercaptoethylamine
MLE	maximum likelihood estimator
MSD	mean square displacement
MSS	moment scaling spectrum
NP	nanoparticle
PALM	photoactivated localization microscopy
PALMIRA	PALM with independently running acquisition
PA-FP	photoactivatable fluorescent protein
PBS	phosphate buffered saline.
PDF	probability density function
PFA	paraformaldehyde
PMT	photomultiplier tubes
PO	precision optimized
PS NP	polystyrene nanoparticle

PSF	point spread function
QD	quantum dot
RO	recall optimized
SBR	signal-to-background ratio
sCMOS	scientific complementary metal-oxide-semiconductor
SNR	signal-to-noise ratio
SPT	single particle tracking
SSIM	saturated structured illumination microscopy
STED	stimulated emission depletion
STORM	stochastic optical reconstruction microscopy
Tf	transferrin
TfR	transferrin receptor
TIRFM	total internal reflection fluorescence microscopy
TRE	target registration error
UAIM	ultrahigh accuracy imaging modality

References

1. Nel, A. E., Mädler, L., Velegol, D., Xia, T., Hoek, E. M. V., Somasundaran, P., Klaessig, F., Castranova, V. & Thompson, M. Understanding biophysicochemical interactions at the nano-bio interface. *Nat. Mater.* **8**, 543–557 (2009).
2. Treuel, L., Jiang, X. & Nienhaus, G. U. New views on cellular uptake and trafficking of manufactured nanoparticles. *J. R. Soc. Interface* **10**, 20120939–20120952 (2013).
3. Jain, R. K. & Stylianopoulos, T. Delivering nanomedicine to solid tumors. *Nat. Rev. Clin. Oncol.* **7**, 653–664 (2010).
4. Shang, L., Nienhaus, K. & Nienhaus, G. Engineered nanoparticles interacting with cells: size matters. *J. Nanobiotechnology* **12**, 5–15 (2014).
5. Iversen, T.-G., Skotland, T. & Sandvig, K. Endocytosis and intracellular transport of nanoparticles: Present knowledge and need for future studies. *Nano Today* **6**, 176–185 (2011).
6. Welsher, K. & Yang, H. Multi-resolution 3D visualization of the early stages of cellular uptake of peptide-coated nanoparticles. *Nat. Nanotechnol.* **9**, 198–203 (2014).
7. Hell, S. W. Microscopy and its focal switch. *Nat. Methods* **6**, 24–32 (2009).
8. Huang, B., Babcock, H. & Zhuang, X. Breaking the diffraction barrier: super-resolution imaging of cells. *Cell* **143**, 1047–1058 (2010).
9. Canton, I. & Battaglia, G. Endocytosis at the nanoscale. *Chem. Soc. Rev.* **41**, 2718–2739 (2012).
10. Doherty, G. J. & McMahon, H. T. Mechanisms of endocytosis. *Annu. Rev. Biochem.* **78**, 857–902 (2009).
11. Elsaesser, A. Taylor, A., de Yanes, G. S., Mckerr, G., Kim, E.-M., O'Hare, E. & Howard, C. V. Quantification of nanoparticle uptake by cells using microscopical and analytical techniques. *Nanomedicine* **5**, 1447–1457 (2010).

12. Aderem, A. & Underhill, D. M. Mechanisms of phagocytosis in macrophages. *Annu. Rev. Immunol.* **17**, 593–623 (1999).
13. Cleal, K., He, L., D. Watson, P. & T. Jones, A. Endocytosis, intracellular traffic and fate of cell penetrating peptide based conjugates and nanoparticles. *Curr. Pharm. Des.* **19**, 2878–2894 (2013).
14. Silverstein, S. C. Phagocytosis of microbes: insights and prospects. *Trends Cell Biol.* **5**, 141–142 (1995).
15. Cougoule, C., Wiedemann, A., Lim, J. & Caron, E. Phagocytosis, an alternative model system for the study of cell adhesion. *Semin. Cell Dev. Biol.* **15**, 679–689 (2004).
16. Araki, N. Phosphoinositide-3-kinase-independent contractile activities associated with Fcγ-receptor-mediated phagocytosis and macropinocytosis in macrophages. *J. Cell Sci.* **116**, 247–257 (2002).
17. Underhill, D. M. & Goodridge, H. S. Information processing during phagocytosis. *Nat. Rev. Immunol.* **12**, 492–502 (2012).
18. Caron, E. & Hall, A. Identification of two distinct mechanisms of phagocytosis controlled by different Rho GTPases. *Science* **282**, 1717–1721 (1998).
19. Geng, Y., Dalhaimer P., Cai, S., Tsai, R., Tewari, M., Minko, T. & Discher, D. E. Shape effects of filaments versus spherical particles in flow and drug delivery. *Nat. Nanotechnol.* **2**, 249–255 (2007).
20. Champion, J. A. & Mitragotri, S. Role of target geometry in phagocytosis. *Proc. Natl. Acad. Sci.* **103**, 4930–4934 (2006).
21. Roth, T. F. Yolk protein uptake in the oocyte of the mosquito *aedes aegypti*.l. *J. Cell Biol.* **20**, 313–332 (1964).
22. Kirchhausen, T. Clathrin. *Annu. Rev. Biochem.* **69**, 699–727 (2000).
23. McMahon, H. T. & Boucrot, E. Molecular mechanism and physiological functions of clathrin-mediated endocytosis. *Nat. Rev. Mol. Cell Biol.* **12**, 517–533 (2011).
24. Brodsky, F. M., Chen, C. Y., Knuehl, C., Towler, M. C. & Wakeham, D. E. Biological basket weaving: formation and function of clathrin-coated vesicles. *Annu. Rev. Cell Dev. Biol.* **17**, 517–568 (2001).

25. Stimpson, H. E. M., Toret, C. P., Cheng, A. T., Pauly, B. S. & Drubin, D. G. Early-arriving Syp1p and Ede1p function in endocytic site placement and formation in budding yeast. *Mol. Biol. Cell* **20**, 4640–4651 (2009).
26. Henne, W. M., Boucrot, E., Meinecke, M., Evergren, E., Vallis, Y., Mittal, R. & McMahon, T. FCHO proteins are nucleators of clathrin-mediated endocytosis. *Science* **328**, 1281–1284 (2010).
27. Stowell, M. H., Marks, B., Wigge, P. & McMahon, H. T. Nucleotide-dependent conformational changes in dynamin: evidence for a mechanochemical molecular spring. *Nat. Cell Biol.* **1**, 27–32 (1999).
28. Merrifield, C. J., Feldman, M. E., Wan, L. & Almers, W. Imaging actin and dynamin recruitment during invagination of single clathrin-coated pits. *Nat. Cell Biol.* **4**, 691–698 (2002).
29. Ehrlich, M., Boll, W., van Oijen, A., Hariharan, R., Chandran, K., Nibert, M. L. & Kirchhausen, T. Endocytosis by random initiation and stabilization of clathrin-coated pits. *Cell* **118**, 591–605 (2004).
30. De Domenico, I., McVey Ward, D. & Kaplan, J. Regulation of iron acquisition and storage: consequences for iron-linked disorders. *Nat. Rev. Mol. Cell Biol.* **9**, 72–81 (2008).
31. Harush-Frenkel, O., Debotton, N., Benita, S. & Altschuler, Y. Targeting of nanoparticles to the clathrin-mediated endocytic pathway. *Biochem. Biophys. Res. Commun.* **353**, 26–32 (2007).
32. Vasir, J. K. & Labhasetwar, V. Quantification of the force of nanoparticle-cell membrane interactions and its influence on intracellular trafficking of nanoparticles. *Biomaterials* **29**, 4244–4252 (2008).
33. Chung, T.-H., Wu, S.-H., Yao, M., Lu, C.-W., Lin, Y.-S., Hung, Y., Mou, C.-Y. Chen, Y. -C., & Huang, D.-M. The effect of surface charge on the uptake and biological function of mesoporous silica nanoparticles in 3T3-L1 cells and human mesenchymal stem cells. *Biomaterials* **28**, 2959–2966 (2007).
34. Ma, Z. & Lim, L.-Y. Uptake of chitosan and associated insulin in Caco-2 Cell monolayers: a comparison between chitosan molecules and chitosan nanoparticles. *Pharm. Res.* **20**, 1812–1819 (2003).
35. Parton, R. G. & Simons, K. The multiple faces of caveolae. *Nat. Rev. Mol. Cell Biol.* **8**, 185–194 (2007).

36. Anderson, R. G. The caveolae membrane system. *Annu. Rev. Biochem.* **67**, 199–225 (1998).
37. Yameen, B. Choi, W. I., Vilos, C., Swami, A., Shi, J. & Farokhzad, O. C. Insight into nanoparticle cellular uptake and intracellular targeting. *J. Control. Release* **190**, 485–499 (2014).
38. Rothberg, K. G., Heuser, J. E., Donzell, W. C., Ying, Y.-S., Glennen, J. R. & Anderson, R. G. W. Caveolin, a protein component of caveolae membrane coats. *Cell* **68**, 673–682 (1992).
39. Pelkmans, L. & Zerial, M. Kinase-regulated quantal assemblies and kiss-and-run recycling of caveolae. *Nature* **436**, 128–133 (2005).
40. Mayor, S. & Pagano, R. E. Pathways of clathrin-independent endocytosis. *Nat. Rev. Mol. Cell Biol.* **8**, 603–612 (2007).
41. Anderson, H. A., Chen, Y. & Norkin, L. C. Bound simian virus 40 translocates to caveolin-enriched membrane domains, and its entry is inhibited by drugs that selectively disrupt caveolae. *Mol. Biol. Cell* **7**, 1825–1834 (1996).
42. Rejman, J., Conese, M. & Hoekstra, D. Gene transfer by means of lipo- and polyplexes: role of clathrin and caveolae-mediated endocytosis. *J. Liposome Res.* **16**, 237–247 (2006).
43. Sahay, G., Kim, J. O., Kabanov, A. V & Bronich, T. K. The exploitation of differential endocytic pathways in normal and tumor cells in the selective targeting of nanoparticulate chemotherapeutic agents. *Biomaterials* **31**, 923–933 (2010).
44. Nishikawa, T., Iwakiri, N., Kaneko, Y., Taguchi, A., Fukushima, K., Mori, H., Morone, N. & Kadokawa, J.-I. Nitric oxide release in human aortic endothelial cells mediated by delivery of amphiphilic polysiloxane nanoparticles to caveolae. *Biomacromolecules* **10**, 2074–2085 (2009).
45. Sandvig, K., Torgersen, M. L., Raa, H. A. & Deurs, B. Clathrin-independent endocytosis: from nonexisting to an extreme degree of complexity. *Histochem. Cell Biol.* **129**, 267–276 (2008).
46. Sahay, G., Alakhova, D. Y. & Kabanov, A. V. Endocytosis of nanomedicines. *J. Control. Release* **145**, 182–195 (2010).

47. Grant, B. D. & Donaldson, J. G. Pathways and mechanisms of endocytic recycling. *Nat. Rev. Mol. Cell Biol.* **10**, 597–608 (2009).
48. Garaiova, Z., Strand, S. P., Reitan, N. K., Lelu, S., Støret, S. Ø., Berg, K., Malmo, J., Folasire, O., Bjørkøy, A. & de L. Davies, C. Cellular uptake of DNA–chitosan nanoparticles: The role of clathrin- and caveolae-mediated pathways. *Int. J. Biol. Macromol.* **51**, 1043–1051 (2012).
49. Lu, Y. & Low, P. S. Folate-mediated delivery of macromolecular anticancer therapeutic agents. *Adv. Drug Deliv. Rev.* **54**, 675–693 (2002).
50. Rijnboutt, S. Endocytosis of GPI-linked membrane folate receptor-alpha. *J. Cell Biol.* **132**, 35–47 (1996).
51. Mercer, J. & Helenius, A. Virus entry by macropinocytosis. *Nat. Cell Biol.* **11**, 510–520 (2009).
52. Kerr, M. C. & Teasdale, R. D. Defining macropinocytosis. *Traffic* **10**, 364–371 (2009).
53. Mercer, J. & Helenius, A. Vaccinia virus uses macropinocytosis and apoptotic mimicry to enter host cells. *Science* **320**, 531–535 (2008).
54. West, M. A., Bretscher, M. S. & Watts, C. Distinct endocytotic pathways in epidermal growth factor-stimulated human carcinoma A431 cells. *J. Cell Biol.* **109**, 2731–2739 (1989).
55. Zhang, L., Zhang, S., Ruan, S.-B., Zhang, Q.-Y., He, Q. & Gao, H.-L. Lapatinib-incorporated lipoprotein-like nanoparticles: preparation and a proposed breast cancer-targeting mechanism. *Acta Pharmacol. Sin.* **35**, 846–852 (2014).
56. Bechtel, W. The cell: Locus or object of inquiry? *Stud. Hist. Philos. Sci. Part C Stud. Hist. Philos. Biol. Biomed. Sci.* **41**, 172–182 (2010).
57. Giepmans, B. N. G. The fluorescent toolbox for assessing protein location and function. *Science* **312**, 217–224 (2006).
58. Abbe, E. Beiträge zur Theorie des Mikroskops und der mikroskopischen Wahrnehmung. *Arch. für Mikroskopische Anat.* **9**, 413–418 (1873).
59. Rayleigh, Lord. On the theory of optical images, with special reference to the microscope. *J. R. Microsc. Soc.* **23**, 474–482 (1903).

60. Koster, A. J. & Klumperman, J. Electron microscopy in cell biology: integrating structure and function. *Nat. Rev. Mol. Cell Biol.* **4**, SS6–S10 (2003).
61. Betzig, E. & Trautman, J. K. Near-field optics: Microscopy, spectroscopy, and surface modification beyond the diffraction limit. *Science* **257**, 189–195 (1992).
62. Rittweger, E., Han, K. Y., Irvine, S. E., Eggeling, C. & Hell, S. W. STED microscopy reveals crystal colour centres with nanometric resolution. *Nat. Photonics* **3**, 144–147 (2009).
63. Schmidt, R., Wurm, C. A., Jakobs, S., Engelhardt, J., Egner, A. & Hell, S. W. Spherical nanosized focal spot unravels the interior of cells. *Nat. Methods* **5**, 539–544 (2008).
64. Gustafsson, M. G. L. Nonlinear structured-illumination microscopy: wide-field fluorescence imaging with theoretically unlimited resolution. *Proc. Natl. Acad. Sci. U. S. A.* **102**, 13081–13086 (2005).
65. Thompson, R. E., Larson, D. R. & Webb, W. W. Precise nanometer localization analysis for individual fluorescent probes. *Biophys. J.* **82**, 2775–2783 (2002).
66. Yildiz, A. Myosin V walks hand-over-hand: Single fluorophore imaging with 1.5-nm localization. *Science* **300**, 2061–2065 (2003).
67. Rust, M. J., Bates, M. & Zhuang, X. Sub-diffraction-limit imaging by stochastic optical reconstruction microscopy (STORM). *Nat. Methods* **3**, 793–796 (2006).
68. Betzig, E., Patterson, G. H., Sougrat, R., Lindwasser, O. W., Olenych, S., Bonifacino, J. S., Davidson, M. W., Lippincott-Schwartz, J. & Hess, H. F. Imaging intracellular fluorescent proteins at nanometer resolution. *Science* **313**, 1642–1645 (2006).
69. Hess, S. T., Girirajan, T. P. K. & Mason, M. D. Ultra-high resolution imaging by fluorescence photoactivation localization microscopy. *Biophys. J.* **91**, 4258–4272 (2006).
70. Heilemann, M., van de Linde, S., Schüttelz, M., Kasper, R., Seefeldt, B., Mukherjee, A., Tinnefeld, P. & Sauer, M. Subdiffraction-resolution fluorescence imaging with conventional fluorescent probes. *Angew. Chem. Int. Ed.* **47**, 6172–6176 (2008).

71. Fölling, J., Bossi, M., Bock, H., Medda, R., Wurm, C. A., Hein, B., Jakobb, S., Eggeling, C. & Hell, S. W. Fluorescence nanoscopy by ground-state depletion and single-molecule return. *Nat. Methods* **5**, 943–945 (2008).
72. Egner, A., Geisler, C., von Middendorff, C., Bock, H., Wenzel, D., Medda, R., Andresen, M., Stiel, A. C., Jakobs, S., Eggeling, C., Schöfle, A. & Hell, S. W. Fluorescence nanoscopy in whole cells by asynchronous localization of photoswitching emitters. *Biophys. J.* **93**, 3285–3290 (2007).
73. Shroff, H., Galbraith, C. G., Galbraith, J. A. & Betzig, E. Live-cell photoactivated localization microscopy of nanoscale adhesion dynamics. *Nat. Methods* **5**, 417–423 (2008).
74. Hedde, P. N. & Nienhaus, G. U. Optical imaging of nanoscale cellular structures. *Biophys. Rev.* **2**, 147–158 (2010).
75. Henriques, R., Lelek, M., Fornasiero, E. F., Valtorta, F., Zimmer, C. & Mhlanga, M. M. QuickPALM: 3D real-time photoactivation nanoscopy image processing in ImageJ. *Nat. Methods* **7**, 339–340 (2010).
76. Huang, F., Hartwich, M. P., Rivera-Molina, F. E., Lin, Y., Duim, W. C., Long, J. J., Uchil, P. D., Myers, J. R., Baird, M. A., Mothes, W., Davidson, M. W., Toomre, D. & Bewersdorf, J. Video-rate nanoscopy using sCMOS camera-specific single-molecule localization algorithms. *Nat. Methods* **10**, 653–658 (2013).
77. Nienhaus, K., Nienhaus, G. U., Wiedenmann, J. & Nar, H. Structural basis for photo-induced protein cleavage and green-to-red conversion of fluorescent protein EosFP. *Proc. Natl. Acad. Sci.* **102**, 9156–9159 (2005).
78. Fernández-Suárez, M. & Ting, A. Y. Fluorescent probes for super-resolution imaging in living cells. *Nat. Rev. Mol. Cell Biol.* **9**, 929–943 (2008).
79. Nienhaus, K. & Ulrich Nienhaus, G. Fluorescent proteins for live-cell imaging with super-resolution. *Chem. Soc. Rev.* **43**, 1088–1106 (2014).
80. Danhier, F., Feron, O. & Prét, V. To exploit the tumor microenvironment: Passive and active tumor targeting of nanocarriers for anti-cancer drug delivery. *J. Control. Release* **148**, 135–146 (2010).
81. Van der Meel, R., Vehmeijer, L. J. C., Kok, R. J., Storm, G. & van Gaal, E. V. B. Ligand-targeted particulate nanomedicines undergoing clinical evaluation: Current status. *Adv. Drug Deliv. Rev.* **65**, 1284–1298 (2013).

82. Andersson, S. B. Localization of a fluorescent source without numerical fitting. *Opt. Express* **16**, 18714–18724 (2008).
83. Ma, H., Long, F., Zeng, S. & Huang, Z.-L. Fast and precise algorithm based on maximum radial symmetry for single molecule localization. *Opt. Lett.* **37**, 2481 (2012).
84. Parthasarathy, R. Rapid, accurate particle tracking by calculation of radial symmetry centers. *Nat. Methods* **9**, 724–726 (2012).
85. Quan, T., Li, P., Long, F., Zeng, S., Luo, Q., Hedde, P. N., Nienhaus, G. U. & Huang, Z.-L. Ultra-fast, high-precision image analysis for localization-based super resolution microscopy. *Opt. Express* **18**, 11867–11876 (2010).
86. Smith, C. S., Joseph, N., Rieger, B. & Lidke, K. A. Fast, single-molecule localization that achieves theoretically minimum uncertainty. *Nat. Methods* **7**, 373–375 (2010).
87. Ruusuvoori, P., Äijö, T., Chowdhury, S., Garmendia-Torres, C., Selinummi, J., Birbaumer, M., Dudley, A. M., Pelkmans, L. & Yli-Harja, O. Evaluation of methods for detection of fluorescence labeled subcellular objects in microscope images. *BMC Bioinformatics* **11**, 248 (2010).
88. Smal, I., Loog, M., Niessen, W. & Meijering, E. Quantitative comparison of spot detection methods in fluorescence microscopy. *IEEE Trans. Med. Imaging* **29**, 282–301 (2010).
89. Křížek, P., Raška, I. & Hagen, G. M. Minimizing detection errors in single molecule localization microscopy. *Opt. Express* **19**, 3226–3235 (2011).
90. Quan, T., Zhu, H., Liu, X., Liu, Y., Ding, J., Zeng, S. & Huang, Z.-L. High-density localization of active molecules using Structured Sparse Model and Bayesian Information Criterion. *Opt. Express* **19**, 16963 (2011).
91. Li, Y., Ishitsuka, Y., Hedde, P. N. & Nienhaus, G. U. Fast and efficient molecule detection in localization-based super-resolution microscopy by parallel adaptive histogram equalization. *ACS Nano* **7**, 5207–5214 (2013).
92. Richards, B. & Wolf, E. Electromagnetic diffraction in optical systems. II. structure of the image field in an aplanatic system. *Proc. R. Soc. A Math. Phys. Eng. Sci.* **253**, 358–379 (1959).

93. Gibson, S. F. & Lanni, F. Experimental test of an analytical model of aberration in an oil-immersion objective lens used in three-dimensional light microscopy. *J. Opt. Soc. Am. A*, **9**, 154–166 (1992).
94. Ram, S., Sally Ward, E. & Ober, R. J. A Stochastic analysis of performance limits for optical microscopes. *Multidimens. Syst. Signal Process.* **17**, 27–57 (2006).
95. Thomann, D., Rines, D. R., Sorger, P. K. & Danuser, G. Automatic fluorescent tag detection in 3D with super-resolution: application to the analysis of chromosome movement. *J. Microsc.* **208**, 49–64 (2002).
96. Janesick, J. *Photon transfer: DN -->[lambda]*. (SPIE Press, Bellingham, WA, USA, 2007)
97. Hirsch, M., Wareham, R. J., Martin-Fernandez, M. L., Hobson, M. P. & Rolfe, D. J. A stochastic model for electron multiplication charge-coupled devices – from theory to practice. *PLoS One* **8**, e53671 (2013).
98. Robbins, M. S. & Hadwen, B. J. The noise performance of electron multiplying charge-coupled devices. *IEEE Trans. Electron Devices* **50**, 1227–1232 (2003).
99. Mortensen, K. I., Churchman, L. S., Spudich, J. A. & Flyvbjerg, H. Optimized localization analysis for single-molecule tracking and super-resolution microscopy. *Nat. Methods* **7**, 377–381 (2010).
100. Chao, J., Ram, S., Ward, E. S. & Ober, R. J. Ultrahigh accuracy imaging modality for super-localization microscopy. *Nat. Methods* **10**, 335–338 (2013).
101. Starck, J., Fadili, J. & Murtagh, F. The undecimated wavelet decomposition and its reconstruction. *IEEE Trans. Image Process.* **16**, 297–309 (2007).
102. Boulanger, J., Kervrann, C. & Bouthemy, P. Space-time adaptation for patch-based image sequence restoration. *IEEE Trans. Pattern Anal. Mach. Intell.* **29**, 1096–1102 (2007).
103. Mallat, S. *A wavelet tour of signal processing: the sparse way*. (Academic Press, Waltham, MA, USA, 2008).
104. Bright, D. S. & Steel, E. B. Two-dimensional top hat filter for extracting spots and spheres from digital images. *J. Microsc.* **146**, 191–200 (1987).

105. Sage, D., Neumann, F. R., Hediger, F., Gasser, S. M. & Unser, M. Automatic tracking of individual fluorescence particles: application to the study of chromosome dynamics. *IEEE Trans. Image Process.* **14**, 1372–1383 (2005).
106. Vincent, L. Morphological grayscale reconstruction in image analysis: applications and efficient algorithms. *IEEE Trans. Image Process.* **2**, 176–201 (1993).
107. Jiang, S., Zhou, X., Kirchhausen, T. & Wong, S. T. C. Detection of molecular particles in live cells via machine learning. *Cytom. Part A* **71**, 563–575 (2007).
108. McLachlan, G. *Discriminant analysis and statistical pattern recognition*. (John Wiley & Sons, Hoboken, NJ, 2004).
109. Wolter, S., Schüttelz, M., Tscherepanow, M., van de Linde, S., Heilemann, M. & Sauer, M. Real-time computation of subdiffraction-resolution fluorescence images. *J. Microsc.* **237**, 12–22 (2010).
110. Hedde, P. N., Fuchs, J., Oswald, F., Wiedenmann, J. & Nienhaus, G. U. Online image analysis software for photoactivation localization microscopy. *Nat. Methods* **6**, 689–690 (2009).
111. Small, A. & Stahlheber, S. Fluorophore localization algorithms for super-resolution microscopy. *Nat. Methods* **11**, 267–279 (2014).
112. Ober, R. J., Ram, S. & Ward, E. S. Localization Accuracy in Single-Molecule Microscopy. *Biophys. J.* **86**, 1185–1200 (2004).
113. Dickson, R., Cubitt, A., Tsien, R. & Moerner, W. On/off blinking and switching behaviour of single molecules of green fluorescent protein. *Nature* **388**, 355–358 (1997).
114. Annibale, P., Vanni, S., Scarselli, M., Rothlisberger, U. & Radenovic, A. Identification of clustering artifacts in photoactivated localization microscopy. *Nat. Methods* **8**, 527–528 (2011).
115. Bilic, J., Huang Y.-L., Davidson, G., Zimmermann, T., Crucial, C.-M., Bienz, M. & Niehrs, C. Wnt induces LRP6 signalosomes and promotes dishevelled-dependent LRP6 phosphorylation. *Science* **316**, 1619–1622 (2007).
116. Wiedenmann, J., Gayda, S., Adam, V., Oswald, F., Nienhaus, K., Bourgeois, D. & Nienhaus, G. U. From EosFP to mIrisFP: structure-based development of

- advanced photoactivatable marker proteins of the GFP-family. *J. Biophotonics* **4**, 377–390 (2011).
117. Holden, S. J., Uphoff, S. & Kapanidis, A. N. DAOSTORM: an algorithm for high-density super-resolution microscopy. *Nat. Methods* **8**, 279–280 (2011).
118. York, A. G., Ghitani, A., Vaziri, A., Davidson, M. W. & Shroff, H. Confined activation and subdiffraction localization enables whole-cell PALM with genetically expressed probes. *Nat. Methods* **8**, 327–333 (2011).
119. Cheezum, M. & Walker, W. Quantitative comparison of algorithms for tracking single fluorescent particles. *Biophys. J.* **81**, 2378–2388 (2001).
120. Bates, M., Huang, B., Dempsey, G. T. & Zhuang, X. Multicolor super-resolution imaging with photo-switchable fluorescent probes. *Science* **317**, 1749–1753 (2007).
121. Wacker, S. A., Alvarado, C., von Wichert, G., Knippschild, U., Wiedenmann, J., Clauß, K., Nienhaus, G. U., Hameister, H., Baumann, B., Borggreffe, T., Knöchel, W. & Oswald, F. RITA, a novel modulator of Notch signalling, acts via nuclear export of RBP-J. *EMBO J.* **30**, 43–56 (2011).
122. Sage, D., Kirshner, H., Pengo, T., Stuurman, N., Min, J., Manley, S. & Unser, M. Quantitative evaluation of software packages for single-molecule localization microscopy. *Nat. Methods* **12**, 717–724 (2015).
123. Tokunaga, M., Imamoto, N. & Sakata-Sogawa, K. Highly inclined thin illumination enables clear single-molecule imaging in cells. *Nat. Methods* **5**, 159–161 (2008).
124. Juetten, M. F., Gould, T. J., Lessard, M. D., Mlodzianoski, M. J., Nagpure, B. S., Bennett, B. T., Hess, S. T. & Bewersdorf, J. Three-dimensional sub-100 nm resolution fluorescence microscopy of thick samples. *Nat. Methods* **5**, 527–529 (2008).
125. Pavani, S. R. P., Thompson, M. A., Biteen, J. S., Lord, S. J., Liu, N., Twieg, R. J., Peistun, R. & Moerner, W. E. Three-dimensional, single-molecule fluorescence imaging beyond the diffraction limit by using a double-helix point spread function. *Proc. Natl. Acad. Sci.* **106**, 2995–2999 (2009).
126. Kao, H. P. & Verkman, A. S. Tracking of single fluorescent particles in three dimensions: use of cylindrical optics to encode particle position. *Biophys. J.* **67**, 1291–1300 (1994).

127. Holtzer, L., Meckel, T. & Schmidt, T. Nanometric three-dimensional tracking of individual quantum dots in cells. *Appl. Phys. Lett.* **90**, 053902 (2007).
128. Huang, B., Wang, W., Bates, M. & Zhuang, X. Three-dimensional super-resolution imaging by stochastic optical reconstruction microscopy. *Science* **319**, 810–813 (2008).
129. McGorty, R., Schnitzbauer, J., Zhang, W. & Huang, B. Correction of depth-dependent aberrations in 3D single-molecule localization and super-resolution microscopy. *Opt. Lett.* **39**, 275–278 (2014).
130. Carl Zeiss Microscopy, GmbH, Zeiss, Jul. 2015. URL: <https://www.microshop.zeiss.com/?l=en&p=us&f=o&a=v&m=a&id=420780-9970-000>
131. Jones, S. A., Shim, S.-H., He, J. & Zhuang, X. Fast, three-dimensional super-resolution imaging of live cells. *Nat. Methods* **8**, 499–508 (2011).
132. Goshtasby, A. Image registration by local approximation methods. *Image Vis. Comput.* **6**, 255–261 (1988).
133. Huang, B., Jones, S. A., Brandenburg, B. & Zhuang, X. Whole-cell 3D STORM reveals interactions between cellular structures with nanometer-scale resolution. *Nat. Methods* **5**, 1047–1052 (2008).
134. Erdelyi, M., Rees, E. & Metcalf, D. Correcting chromatic offset in multicolor super-resolution localization microscopy. *Opt. Express* **21**, 12177–12183 (2013).
135. Dani, A., Huang, B., Bergan, J., Dulac, C. & Zhuang, X. Superresolution imaging of chemical synapses in the brain. *Neuron* **68**, 843–856 (2010).
136. Shroff, H., Galbraith, C. G., Galbraith, J. A., Whiter, H., Gillette, J., Olenych, S., Davidson, M. W. & Betzig, E. Dual-color superresolution imaging of genetically expressed probes within individual adhesion complexes. *Proc. Natl. Acad. Sci.* **104**, 20308–20313 (2007).
137. Bossi, M., Fölling, J., Belov, V. N., Boyarskiy, V. P., Medda, R., Egner, A., Eggeling, C., Schönle, A. & Hell, S. W. Multicolor far-field fluorescence nanoscopy through isolated detection of distinct molecular species. *Nano Lett.* **8**, 2463–2468 (2008).
138. Baddeley, D., Crossman, D., Rossberger, S., Cheyne, J. E., Montgomery, J. M., Jayasinghe, I. D., Cremer, C., Cannell, M. B. & Soeller, C. 4D Super-

- Resolution Microscopy with Conventional Fluorophores and Single Wavelength Excitation in Optically Thick Cells and Tissues. *PLoS One* **6**, e20645 (2011).
139. Hoyer, P., Staudt, T., Engelhardt, J. & Hell, S. W. Quantum dot blueing and blinking enables fluorescence nanoscopy. *Nano Lett.* **11**, 245–250 (2011).
140. Köhler, D. M. Dreidimensionale stochastische höchstauflösende Mikroskopie mit mehreren Farbkkanälen. Karlsruhe Institute of Technology, Diploma thesis (2013).
141. Pinaud, F., Clarke, S., Sittner, A. & Dahan, M. Probing cellular events, one quantum dot at a time. *Nat. Methods* **7**, 275–285 (2010).
142. Feder, T. J., Brust-Mascher, I., Slattery, J. P., Baird, B. & Webb, W. W. Constrained diffusion or immobile fraction on cell surfaces: a new interpretation. *Biophys. J.* **70**, 2767–2773 (1996).
143. Saxton, M. J. & Jacobson, K. Single-particle tracking: Applications to membrane dynamics. *Annu. Rev. Biophys. Biomol. Struct.* **26**, 373–399 (1997).
144. Sbalzarini, I. F. & Koumoutsakos, P. Feature point tracking and trajectory analysis for video imaging in cell biology. *J. Struct. Biol.* **151**, 182–195 (2005).
145. Ewers, H., Smith, A. E., Sbalzarini, I. F., Lilie, H., Koumoutsakos, P. & Helenius, A. Single-particle tracking of murine polyoma virus-like particles on live cells and artificial membranes. *Proc. Natl. Acad. Sci.* **102**, 15110–15115 (2005).
146. Ferrari, R., Manfroi, A. J. & Young, W. R. Strongly and weakly self-similar diffusion. *Phys. D Nonlinear Phenom.* **154**, 111–137 (2001).
147. Van de Linde, S., Löschberger, A., Klein, T., Heidbreder, M., Wolter, S., Heilemann, M. & Sauer, M. Direct stochastic optical reconstruction microscopy with standard fluorescent probes. *Nat. Protoc.* **6**, 991–1009 (2011).
148. Dempsey, G. T., Vaughan, J. C., Chen, K. H., Bates, M. & Zhuang, X. Evaluation of fluorophores for optimal performance in localization-based super-resolution imaging. *Nat. Methods* **8**, 1027–1036 (2011).
149. Schäfer, P., van de Linde, S., Lehmann, J., Sauer, M. & Doose, S. Methylene blue- and thiol-based oxygen depletion for super-resolution imaging. *Anal. Chem.* **85**, 3393–3400 (2013).

150. Englander, S. W., Calhoun, D. B. & Englander, J. J. Biochemistry without oxygen. *Anal. Biochem.* **161**, 300–306 (1987).
151. Shi, X., Lim, J. & Ha, T. Acidification of the oxygen scavenging system in single-molecule fluorescence studies: *In situ* sensing with a ratiometric dual-emission Probe. *Anal. Chem.* **82**, 6132–6138 (2010).
152. Patil, P. V & Ballou, D. P. The Use of Protocatechuate dioxygenase for maintaining anaerobic conditions in biochemical experiments. *Anal. Biochem.* **286**, 187–192 (2000).
153. Van de Linde, S., Krstić, I., Prisner, T., Doose, S., Heilemann, M. & Sauer, M. Photoinduced formation of reversible dye radicals and their impact on super-resolution imaging. *Photochem. Photobiol. Sci.* **10**, 499–506 (2011).
154. Dempsey, G. T., Bates, M., Kowtoniuk, W. E., Liu, D. R., Tsien, R. Y. & Zhuang, X. Photoswitching Mechanism of Cyanine Dyes. *J. Am. Chem. Soc.* **131**, 18192–18193 (2009).
155. Jiang, X., Röcker, C., Hafner, M., Brandholt, S., Dürlich, R. M. & Nienhaus, G. U. Endo- and exocytosis of zwitterionic quantum dot nanoparticles by live HeLa cells. *ACS Nano* **4**, 6787–6797 (2010).
156. Bertrand, N., Wu, J., Xu, X., Kamaly, N. & Farokhzad, O. C. Cancer nanotechnology: the impact of passive and active targeting in the era of modern cancer biology. *Adv. Drug Deliv. Rev.* **66**, 2–25 (2014).
157. Otsuka, H., Nagasaki, Y. & Kataoka, K. PEGylated nanoparticles for biological and pharmaceutical applications. *Adv. Drug Deliv. Rev.* **55**, 403–419 (2003).
158. Wade, R. Microtubule structure and dynamics. *Curr. Opin. Cell Biol.* **9**, 12–17 (1997).
159. Tan, Y. H., Liu, M., Nolting, B., Go, J. G., Gervay-Hague, J. & Liu, G.-Y. A nanoengineering approach for investigation and regulation of protein immobilization. *ACS Nano* **2**, 2374–2384 (2008).
160. Alberts, B., Bray, D., Hopkin, K., Johnson, A., Lewis, J., Raff, M., Roberts, K. & Walter, P. *Essential cell biology*. (Garland Science, New York, NY, 2013).
161. Török, P. & Wilson, T. Rigorous theory for axial resolution in confocal microscopes. *Opt. Commun.* **137**, 127–135 (1997).

162. Kirchhausen, T. Imaging endocytic clathrin structures in living cells. *Trends Cell Biol.* **19**, 596–605 (2009).
163. Arcizet, D., Meier, B., Sackmann, E., R äller, J. & Heinrich, D. Temporal analysis of active and passive transport in living cells. *Phys. Rev. Lett.* **101**, 248103 (2008).
164. Wang, Z., Tiruppathi, C., Minshall, R. D. & Malik, A. B. Size and dynamics of caveolae studied using nanoparticles in living endothelial cells. *ACS Nano* **3**, 4110–4116 (2009).
165. Rejman, J., Oberle, V., Zuhorn, I. S. & Hoekstra, D. Size-dependent internalization of particles via the pathways of clathrin- and caveolae-mediated endocytosis. *Biochem. J.* **377**, 159–169 (2004).
166. Kusumi, A., Sako, Y. & Yamamoto, M. Confined lateral diffusion of membrane receptors as studied by single particle tracking (nanovid microscopy). Effects of calcium-induced differentiation in cultured epithelial cells. *Biophys. J.* **65**, 2021–2040 (1993).
167. Kusumi, A., Nakada, C., Ritchie, K., Murase, K., Suzuki, K., Murakoshi, H., Kasai, R. R., Kondo, J. & Fujiwara T. Paradigm shift of the plasma membrane concept from the two-dimensional continuum fluid to the partitioned fluid: High-speed single-molecule tracking of membrane molecules. *Annu. Rev. Biophys. Biomol. Struct.* **34**, 351–378 (2005).
168. Sako, Y. Compartmentalized structure of the plasma membrane for receptor movements as revealed by a nanometer-level motion analysis. *J. Cell Biol.* **125**, 1251–1264 (1994).

Appendix

The screenshot shows a dialog box titled "Analyse PALM/STORM Particles" with a close button in the top right corner. The dialog contains several sections of settings:

- Minimum SNR:** 5.00
- Maximum FWHM (in px):** 5
- Image plane pixel size (nm):** 107.00
- Checkboxes:**
 - Smart SNR
 - 3D PALM (astigmatism) - will require calibration file
 - Online rendering
 - Attach to running acquisition
 - Stream particle info directly into file
- Online rendering settings (used only if selected) --**
 - Pixel size of rendered image (nm):** 30.00
 - Accumulate last (0 to accumulate all frames):** 0
 - Update every (frames):** 10
- Attach to running acquisition settings (used only if selected) --**
 - Image name pattern (NN...NN represents the numerical change):** imgXXXXXXXX.tif
 - Start NN...NN with:** 0
 - In acquisition max. wait time for new image (ms):** 50
- Advanced settings (don't normally need to be changed) --**
 - Minimum symmetry (%):** 1
 - Local threshold (% maximum intensity):** 40
 - Maximum iterations per frame:** 1000
 - Threads (each takes ~3*[frame size] in memory):** 50
- Don't forget to save the table in the end...**
- Buttons:** OK, Cancel

Figure S1 : Computer screenshot displaying the input parameters used for QuickPALM.

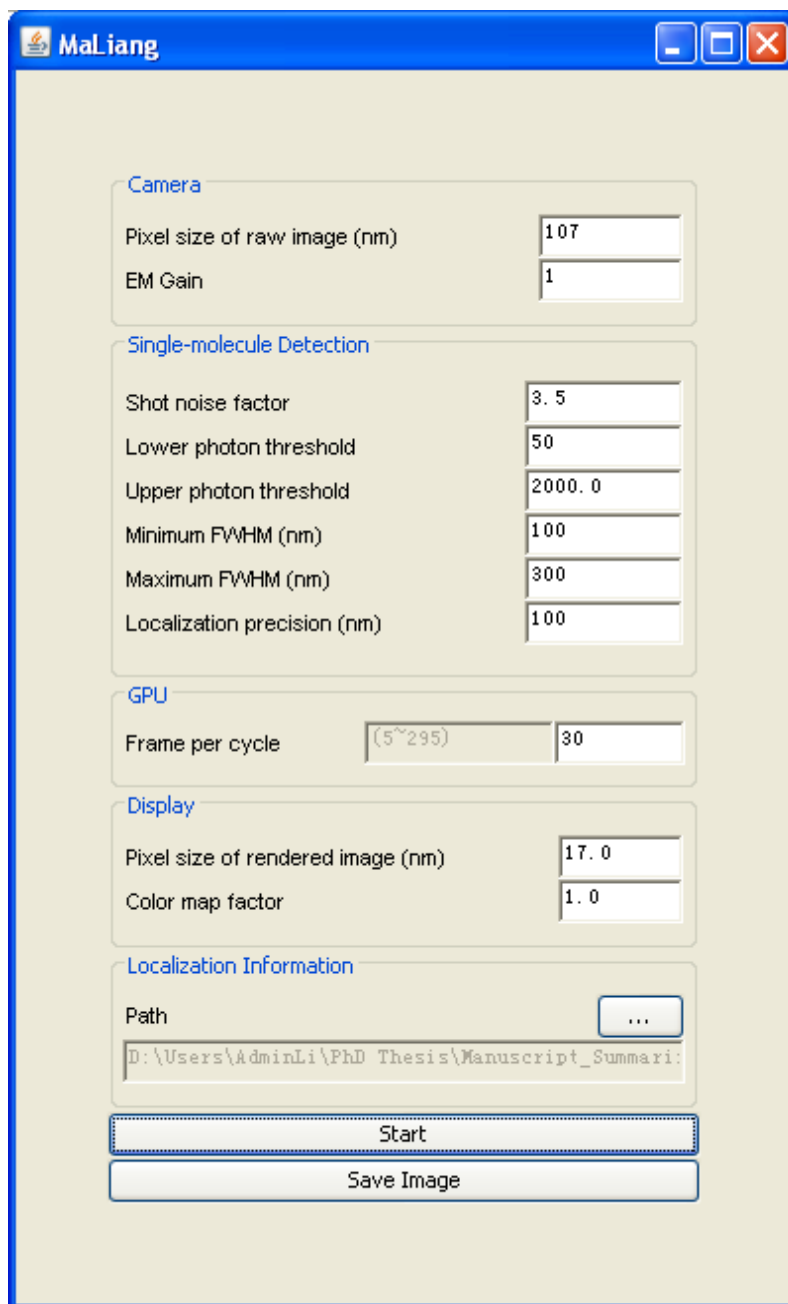


Figure S2 : Computer screenshot displaying the input parameters used for Maliang.

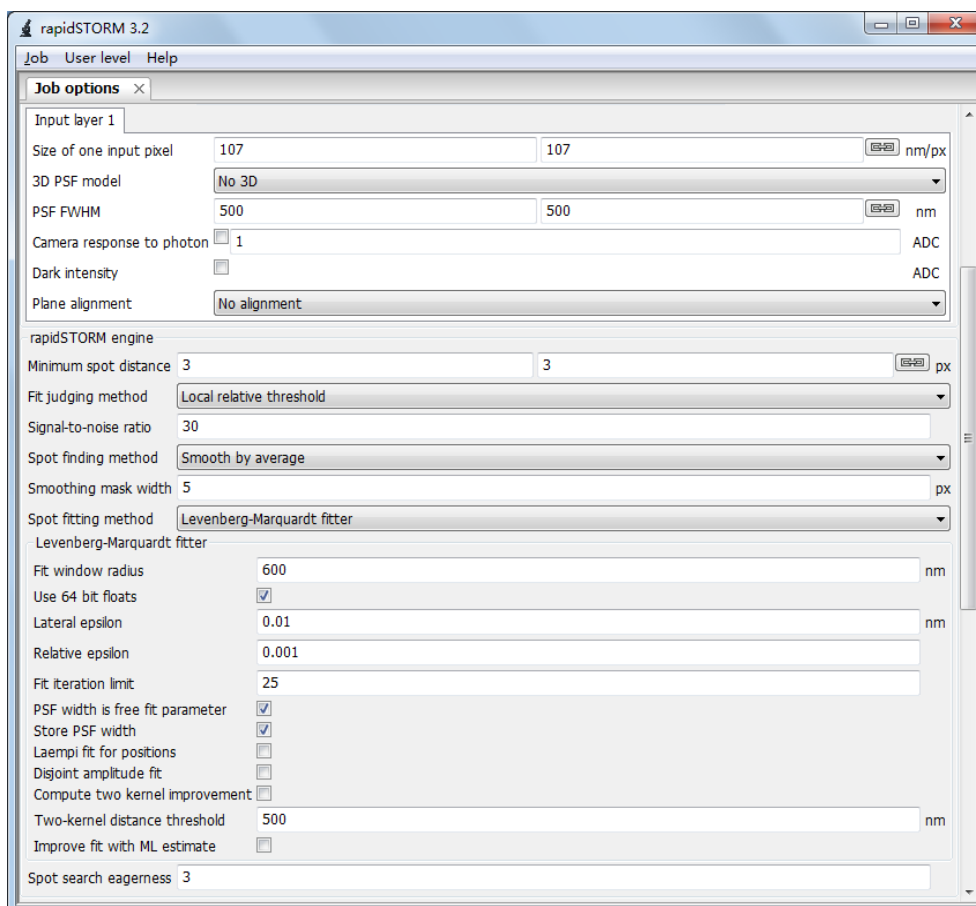


Figure S3 : Computer screenshot displaying the input parameters used for rapidSTORM.

List of Publications

- Li, Y., Ishitsuka, Y., Hedde, P. N. & Nienhaus, G. U. Fast and efficient molecule detection in localization-based super-resolution microscopy by parallel adaptive histogram equalization. *ACS Nano* **7**, 5207–5214 (2013).
- Ishitsuka, Y., Savage, N., Li, Y., Bergs, A., Grün, N., Kohler, D., Donnelly, R., Fischer, R., Takeshita, N., Nienhaus, G.U. Super-resolution microscopy reveals a dynamic picture of cell polarity maintenance during directional growth. Submitted
- Li, Y., *et al.* Super-resolution imaging-based single particle tracking reveals fast dynamics of nanoparticle-cellular interactions. Manuscript in preparation

List of Presentations

- 2011 *Focus on Microscopy (FOM) conference in Konstanz, Germany*. Li, Y., Hedde, P. N., & Nienhaus, G. U.: Online Photoactivation Localization Microscopy (PALM) Imaging. **Poster presentation.**
- 2011 *Sectional Meeting of the Deutsche Gesellschaft für Biophysik (DGfB) in Hühnfeld, Germany*. Li, Y., Hedde, P. N., & Nienhaus, G. U.: Towards Real-time Dynamic Photoactivation Localization Microscopy (PALM) Imaging. **Poster presentation.**
- 2012 *Annual meeting of the Deutsche Gesellschaft für Biophysik (DGfB) in Göttingen, Germany*. Li, Y., Hedde, P. N., Ishitsuka, Y. & Nienhaus, G. U.: Fast and robust image reconstruction in localization-based super-resolution microscopy. **Poster presentation.**
- 2013 *International Symposium on Biomedical Imaging (ISBI) in San Francisco, USA*. Li, Y., Ishitsuka, Y. Hedde, P. N., & Nienhaus, G. U.: Fast and efficient molecule detection in localization-based super-resolution microscopy by parallel adaptive histogram equalization. **Invited talk.**

Curriculum Vitae

PERSONAL INFORMATION

Name Yiming Li

Nationality Chinese

EDUCATION

12/2010 - present **PhD candidate** at Karlsruhe Institute of Technology
PhD project: Super-resolution Imaging Techniques for Studying Cellular Uptake of Nanoparticles

09/2009 – 09/2010 **M.Sc.** Medical Physics at Heidelberg University
Master thesis: Membrane Reconstruction by Localization Microscopy: Spectral Precision Distance Microscopy (SPDM)

09/2005 – 07/2009 **B.E.** Biomedical Engineering at Shanghai Jiao Tong University
Bachelor thesis: Construction of a Portable Confocal Microscope for Imaging Human Tissue in *vivo*

Acknowledgements

First of all, I would like to thank **Prof. Dr. Gerd Ulrich Nienhaus** who drew my interest to far field optical nanoscopy and gave me the opportunity, the encouragement, the freedom to explore the many different aspects of super-resolution microscopy that have found their way into my thesis. I also want to thank **Prof. Dr. Martin Bastmeyer** for making himself available as external referee to review this work.

I am deeply indebted to all the members of the group for the kind regard and on-going support. I'm especially thankful to **Dr. Yuji Ishitsuka** for a lot of suggestions on this work and many stimulating discussions. He also taught me a lot about the cell biological experiments. I also would like to thank very much to **Dr. Li Shang** who kindly help me modify the nanoparticles and provided me helpful advices. I would like to thank **Dr. Karin Nienhaus** who revised my thesis very carefully and gave a lot of suggestions to my thesis. I also want to thank all the other people in this group: **Dr. Per Niklas Hedde, René Dörlich, Anika Hense, Pauline Maffre, Michael Horn, Linxiao Yang, Christoph Manz** and others.

I would also like to thank the external collaborator **Dr. Qing Chen** who provided me the COS-7 cells and introduced me to the transfection protocol with PromoFectin.

Finally, I would like to thank all who have supported and helped me during the course of my PhD thesis. Particular thanks go to my parents and wife. None of this would have been possible without their ongoing support.